TECHNISCHE UNIVERSITÄT MÜNCHEN

Lehrstuhl für Nanoelektronik

Micromagnetic Simulation of Field-Coupled Devices from Co/Pt Nanomagnets

Xueming Ju

Vollständiger Abdruck der von der Fakultät für Elektrotechnik und Informationstechnik der Technischen Universität München zur Erlangung des akademischen Grades eines

Doktor-Ingenieurs

genehmigten Dissertation.

Vorsitzender:	Univ.-Prof. Dr. techn. Josef A. Nossek
Prüfer der Dissertation:	1. Univ.-Prof. Paolo Lugli, Ph. D.
	2. Prof. Dr. Wolfgang Porod
	University of Notre Dame, USA

Die Dissertation wurde am 14. 06. 2012 bei der Technischen Universität München eingereicht und durch die Fakultät für Elektrotechnik und Informationstechnik am 18. 10. 2012 angenommen.

MICROMAGNETIC SIMULATION OF FIELD-COUPLED LOGIC DEVICES FROM CO/PT NANOMAGNETS

Abstract

by

Xueming Ju

Nanomagnet Logic (NML), also known as Magnetic Quantum-dot Cellular Automata, emerges as a promising candidate of novel "beyond CMOS" technology. In this new paradigm, single-domain nanomagnets represent fundamental logic states, and digital information computing is realized by means of their magnetic interactions, providing benefits such as nonvolatility, high integration density, low power dissipation and room temperature operation.

A fully functional NML system is composed of an electronic/magnetic interface serving as an input, strongly field-coupled nanomagnets array which store and process data, a clocking structure to drive and control the information flow through logic elements, and an electronic readout mechanism. Within the scope of this dissertation, the main goal is to implement computational study on the recently proposed Co/Pt multilayer-based NML. Different from most of the research on in-plane NML so far, Co/Pt multilayer-based nanomagnets with anisotropy perpendicular to the film plane offer strong out-of-plane magnetic coupling. The magnetic properties of the Co/Pt multilayer films can be engineered by focused ion beam irradiation, which provides more design choices for the purpose of NML applications.

More specifically, a tailor-made simulation model for Co/Pt nanomagnets has been developed to fully characterize the switching behavior in NML. In particular, the model of partially irradiated Co/Pt nanomagnets is presented. In our former study, ordering frustrations and wrong metastable states have been observed both

in experiments and simulations. However, with a proper partially irradiation on Co/Pt nanomagnets, non-reciprocal coupling behavior can be obtained. This non-reciprocal coupling results in a well-controlled information flow and effectively remove the existed errors. Our simulations verified with a properly chosen clocking field, error-free NML can be achieved. With this model, for the first time we demonstrate our design of a systolic architecture built with Co/Pt nanomagnets – an NML application of large-scale circuitry.

Furthermore, our computational study of the recently proposed clocking scheme – clocking NML with domain wall is discussed in details. The simulation results verified its feasibility and suggest the possibility of a further reduction of the power consumed in NML clocking structure.

The last not the least, most of the computational study has been confirmed by experiments: a fruitful of latest experiment implementations are revealed. These efforts are made by our cooperative experimental group – Lehrstuhl für Technische Elektronik (LTE) of Technische Universität München and Center for Nano Science and Technology from University of Notre Dame (US).

CONTENTS

FIGURES

ACKNOWLEDGEMENTS

For the first and the most, I would like to express my gratitude to my advisors – Prof. Paolo Lugli and Prof. György Csaba.

I am so grateful that Prof. Paolo Lugli in the first instance offered me this valuable opportunity to commence my Ph.D study at the Institute for Nanoelectronics. He provided me the best atmosphere for my research. I can always obtain solid support, stimulating suggestions and encouragements from him. It is such a wonderful three-year working experience with all of these friendly and helpful colleagues in our institute.

I am deeply indebted to Prof. György Csaba, who pioneered the research on Nanomagnet Logic at Techinishe Universität München and led me to this novel and interesting field. I would like to thank him for his guidance through my whole study, all the constructive discussions and always patient and insightful answers to my questions. He became a research assistant professor at University of Notre Dame when I was half way of my Ph.D study. Despite the inconvenience of long distance and time difference, he always spares time to advise me every week in the midst of pressing affairs. During my visiting at Notre Dame, he and Veronika gave me the most warmhearted personal help and support. All of these are unforgettable in all my life.

I would like to express my thanks to the other members in our nanomagnetism research group: Prof. Doris Schmitt-Landsiedel, Dr. Markus Becherer, Josef Kiermaier, Stephan Breitkreutz and Irina Eichwald. Markus initialized the experimental investigations and has been making great efforts to push our project forward. Thanks for so well organized group meetings and valuable experimental data support from these group mates. I indeed learned a lot from them.

I am very grateful to Prof. Wolfgang Porod, who initialized the Nanomagnet Logic research at the University of Notre Dame. I really appreciate that he offered me the chance to visit University of Notre Dame. I gain more confidence from his encouragement. I spent the most wonderful time there during my visit. It was also very nice experience to cooperate with Prof. Michael Niemier, Prof. Gary. H. Bernstein and Peng Li from Notre Dame nanomagnetism group.

Andrea Savo, Stephanie Wartenburg and Fabian Flach, they accomplished their thesis with me and have done an outstanding job. Thanks for their contributions.

Special thanks to my fiancee Wen Cui – though she did bring me 'troubles' during my study. I am very grateful for her support, such a long-time waiting and longing for in faraway Beijing.

I also would like to acknowledge the Deutsche Forschungsgemeinshaft (DFG) and Defense Advanced Research Projects Agency (DARPA). Their financial support made this dissertation possible.

SYMBOLS

A_{exch}	Exchange stiffness
$\mathbf{B}$	Magnetic induction
B_c	Coercivity
B_{cpl}	Coupling magnetic field
$B_{\text{cpl}}^{\text{left}}$	Left-side coupling field
$B_{\text{cpl}}^{\text{right}}$	Right-side coupling field
B_{LR}	Difference between left-side coupling and right-side coupling
B_{osc}	Amplitude of external oscillating field
D	Dose of FIB irradiation
E_{anis}	Anisotropy Energy
E_{demag}	Demagnetizing energy
E_{ex}	Exchange energy
E_{therm}	Thermal energy
E_{total}	Total energy
E_{Zeeman}	Zeeman (external field) energy
h	Planck constant
$\mathbf{H}$	Magnetic field
$\mathbf{H}_{\text{anis}}$	Anisotropy field
$\mathbf{H}_{\text{eff}}$	Effective magnetic field
$\mathbf{H}_{\text{exch}}$	Exchange field
$\mathbf{H}_{\text{therm}}$	Thermal field
$\mathbf{H}_{\text{Maxwell}}$	Maxwell (real) magnetic field
$\mathbf{H}_{\text{Zeeman}}$	Externally applied magnetic field
i	Index of one atom or dipole

j	Index of another atom or dipole
J_{ex}	Exchange integral
K	Anisotropy value in simulation
K_V	Volume anisotropy
K_S	Interface anisotropy
$\mathrm{k_B}$	Boltzmann's constant
$\mathbf{M}(\mathbf{r}, t)$	Magnetization distribution
M_s	Saturation magnetization
n	Number of processor elements in systolic pattern matchers
$\mathbf{r}$	Spatial position
r_{ij}	Distance between two dipoles
$\mathbf{s}$	Spin vector
$\mathbf{S}_{\mathrm{i}}$	Spin vector of one atom
$\mathbf{S}_{\mathrm{j}}$	Spin vector of the neighboring atom
t_{Co}	Total layer thickness of Co
t_{Co+Pt}	Total Co/Pt multilayer thickness
α	Damping constant of the Landau-Lifshitz equation
γ	Gyromagnetic ratio
λ_{ex}	Exchange length
μ_0	Vacuum permeability
$\mu_{\mathbf{H}}$	Magnetic moment per atom
μ_{i}	Magnetic moment of one dipole
μ_{j}	Magnetic moment of the neighboring dipole
π	Circumference ratio
ϕ	Angle between the spins of two atoms
Δt	Time scale of thermal fluctuation

CHAPTER 1

INTRODUCTION

1.1 Motivation of this work

Nowadays, the most extensively argued hot-spot in electronic realm is how to continue the health and success of electronic industry, facing the nearly touchable end of MOS-era. With the rapid development of nanotechnology, plenty of research work emerges during the last few years of the new century, dedicating in maintaining the prosperity of industry by utilizing new functional materials, novel architectures and alternative computing paradigms. This dissertation presents our efforts in searching for opportunities realizing Boolean logic computing in an unconventional way – Nanomagnet Logic (NML).

In the latest report of International Technology Roadmap for Semiconductors (ITRS), Nanomagnet Logic (NML) appears in the Chapter 'Emerging Research Devices' as one of the most promising alternative approaches of information processing beyond CMOS technology [1]. NML research belongs to the framework of spintronics, which is an emerging nanotechnology that exploits both the intrinsic spin of electrons and its associated magnetic moment, in addition to its electron charge. Instead of presenting binary states with electron charge in conventional devices, electron spins of ferromagnetic materials are employed in NML to perform Boolean logic operations and build non-charge-based devices.

Date back to ancient China, it is recorded that people started to recognize magnetism and use lodestone compass for navigation, where they sculpted a directional spoon from lodestone in such a way that the handle of the spoon always pointed south, as shown in Fig. 1.1. Thousands of years later, in modern tech-

nology, the 'nanoscale spoons' are widely unitized in memory applications, where the 'handle of spoon' indicates binary information either '1' or '0'. The study of this dissertation is to better understand the dynamics of these 'nano-spoons', aiming to achieve Boolean logic computing by aligning all these interacting 'nano-spoons'. In the earlier research from University of Notre Dame, investigations have been implemented on magnetic field-coupled Permalloy nanomagnets with planar magnetization. In this dissertation, we follow their tracks, but focus on a new medium – ultra-thin cobalt/platinum (Co/Pt) multilayer material system, chasing the same target.

Figure 1.1. Model of 'spoon-like' compass in ancient China indicating south [2].

In order to have an in-depth understanding of the magnetic properties of this ultra-thin film system, an important task of my work is to develop a simulation model for extensive micromagnetic simulations. With the support of the simulation tools, we can explore the magnetic behaviors of individual nanomagnets and field-coupled nanomagnets, and the feasibility of achieving reliable error-free NML computing. These micromagnetic simulations should provide accurate and constructive guide for our experiment group in fabricating and characterizing Co/Pt

nanomagnets in NML-related microstructures.

Though this dissertation mainly deals with Co/Pt multilayer-based NML, the comparison with Permalloy-based NML is given from time to time. Most of the content of this dissertation is predominantly theoretical. The latest experimental results are also included to confirm our study and encourage the future work. We believe, more and more exciting results are yet to come.

1.2 Structure of this dissertation

As spintronics pops up recently, more and more research groups show their interest and get involved in this field of NML research. Chapter 2 briefly reviews the basic concepts in NML and the rise of NML in the last decade. Here we classify NML according to the way it defines and propagates binary information. The state-of-art is demonstrated, with the most dedicated two research groups in the world as representatives (Prof. Porod's group from Notre Dame and Prof. Cowburn's group from the UK). Compared to them, the new features of Co/Pt based NML in our study are exhibited.

As theoretical foundation of this work, micromagnetic theory is summarized in Chapter 3 to make this dissertation more readable for electrical engineers. The description of our simulation packages is also included in this chapter.

My own contribution within my Ph. D career starts from Chapter 4. In this chapter, a new calibrated simulation model of Co/Pt multilayer nanomagnets is developed by fitting with experimental data from our group partner LTE. Based on this simulation model, the reversal characteristics of Co/Pt nanomagnets have been fully studied. Further, we discuss the sources of the most frequently observed errors in both experiments and simulations.

With the raised question – 'how to avoid these errors' addressed in Chapter 4, we propose to ensure the information flow by means of non-reciprocal coupling, which can be realized by asymmetrical FIB irradiation on Co/Pt nanomagnets and we call these nanomagnets partially irradiated nanomagnets. Chapter 5 is the

core of the whole dissertation. I spend the most ink here describing in full detail the idea to induce asymmetrical coupling among Co/Pt nanomagnets with FIB irradiation. With this approach, for the first time we obtained error-free, perfectly controlled NML in our simulations by properly engineering the nanomagnets and clocking field. Some of the latest experimental outcome is shown in the last section of this chapter, to prove that we are on the right way.

In Chapter 6, it is demonstrated that we are the first to apply the model of partially irradiated nanomagnets in a large-scale circuit – a systolic array. This chapter describes why systolic structure is suitable for NML application and presents our designed structure of an N-bit systolic pattern matcher made up with Co/Pt nanomagnets. This design is the most compacted so far. Micromagnetic simulations proved with this design, the circuits could operate without any errors, enlightening us to have nanomagnets working in more circuit-level applications. Moreover, the evaluation on the circuit performance is also given here, such as power dissipation, working frequency and comparison with CMOS technology.

One of the most critical issue for NML is how to clock the nanomagnets most efficiently. From our calculation, the switching of nanomagnets consumes very little energy, but power consumed from clocking structure dominates in the overhead. Chapter 7 demonstrates the new idea to clock the nanomagnets with the interaction of domain walls. Three dimensional simulations are used to show how the fringing field from a Permalloy domain wall influences the switching behavior of Co/Pt nanomagnets. Particularly, we verified the feasibility of using this clocking scheme to order the nanomagnets with a proper geometry.

Apart from the main content of this dissertation, the investigations of switching behavior of Permalloy dots and the method to directly measure the coupling strength between Permalloy dots are summed up in Appendix A. This work is cooperated with nanomagnetism group from University of Notre Dame.

CHAPTER 2

OVERVIEW OF NANOMAGNET LOGIC

Aggressive scaling of CMOS devices results in a series of non-ideal behaviors such as high leakage current and a high power density level. These road blocks slow down the steps of Moore's Law. Due to physical, technological and economic constraints, the end of the road for continuous CMOS scaling becomes in sight [3].

Quantum-dot Cellular Automata (QCA) [4] is a semiconductor quantum dot device in computational nanotechnology for the realization of computing by arrays of nano-scale QCA units. The concept of QCA attracts lots of attention thanks to its extremely small feature size and ultra-low power consumption. The basic unit in QCA is called a cell, which consists of four dots at the corners with two electrons, which can tunnel between the dots. Due to Coulomb repulsion, the two excess electrons always occupy diagonally opposite dots. The two configurations with energetically equivalent polarizations are designated as two logic states, as shown in Fig. 2.1.

However, QCA only operates at very low temperature. In addition, the fabrication process is usually at a great price. The idea of magnetic information processing has been around for decades [5] [6] [7], and viewed as a curious, unorthodox computing paradigm. More recently, magnetic Quantum-dot Cellular Automata (MQCA) was first proposed in [8], where processing method based on magnetism was reported: networks of interacting submicrometer magnetic dots are used to perform logic operations at room temperature. This idea emerges as a non-FET, non-charge-based 'beyond CMOS' technology aiming to building an alternative information processing besides CMOS for specific applications. In-

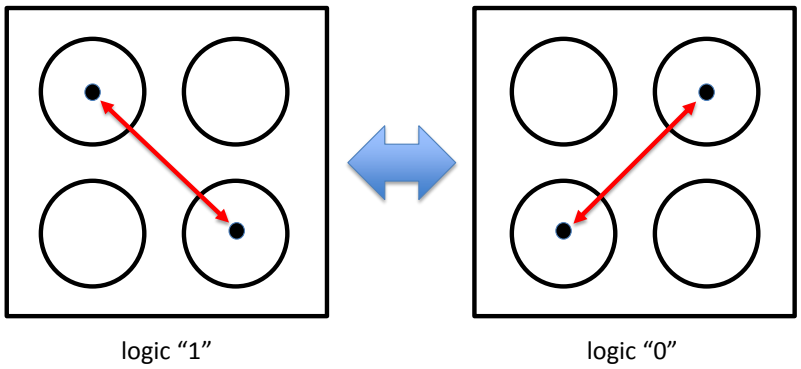

Figure 2.1. Two configured logic states of MQCA.

stead of electron charge in conventional electronic devices, in MQCA the spin of electrons in ferromagnetic materials is employed as a new way indicating binary states for logic computing. The logic states are distinguished by the spin orientation in nano-scale structures, and computing process purely relies on magnetic interactions superposed with clocking signal [9].

According to the way defining binary logic states, the up-to-date MQCA can be further classified as (1) domain-wall-motion based Domain Wall Logic (DWL) and (2) field-coupled nanomagnets based Nanomagnet Logic (NML).

2.1 Domain Wall Logic

Down to nano-scale, the magnetic moments of ultra-small ferromagnetic materials tend to align in the same direction. This is well known as single-domain phenomenon. The single-domain behavior has already been extensively investigated in earlier publications [10] [11] [12] and will be further discussed in this dissertation. From the year 2000 to 2005, Prof. R. P. Cowburn's group demonstrated magnetic domain-wall logic elements [13] [14] [15], such as fan-out, cross-over, logical NOT and AND junctions and summarized them in [16]. The comparison was made with conventional CMOS circuits. In their research scope, the information computing was realized by driving and detecting the magnetic states in specifically

designed structures. Fig. 2.2 illustrates a structure including one NOT gate, one AND gate, two fan-out junctions and one cross-over junction [16]. To generate and drive the domain wall, a rotating external field is required. The motion of domain wall is controlled by this external field, and logic state switches as the magnetization state at certain part of the structure changes to the opposite direction. Controlling the domain wall position in the structures is the key for this kind of logic scheme.

In order to have a good control of the domain wall, it is very much necessary to have well defined and fabricated fine parts of logic elements in experiments. Unavoidable edge roughness may lead to errors as the domain wall propagates (the domain wall gets stuck). More recently, Prof. Cowburn's group has been making efforts to investigate the motion-control and pinning of domain wall in new microstructures for logic computing and also other potential applications, e.g. high density data storage. For more details, see [17] [18] [19] [20] [21] [22].

2.2 Nanomagnet Logic

As discussed, in Quantum-dot Cellular Automata, the binary states are distinguished by the position configurations of two electrons in one cell. The electrostatic force acts as the interaction between the electrons. Instead of the electrostatic interaction in QCA, the magnetic interaction between single-domain nanomagnets tend to align the magnets in ferromagnetical or antiferromagnetical manner, depending on how the magnets are placed. Each nanomagnet behaves as an island, and one island can communicate with other islands close by with magnetic interactions. A designed layout of magnet-array can carry out Boolean logic computing. Instead of transmitting information inside the continuous nanowires as in Domain Wall Logic structures, here the information propagates by 'jumping' from one nanomagnet to the neighboring one. We name this type of computing magnet-array Nanomagnet Logic. The main focus of my dissertation lies only on NML and DWL is just seldom invloved.

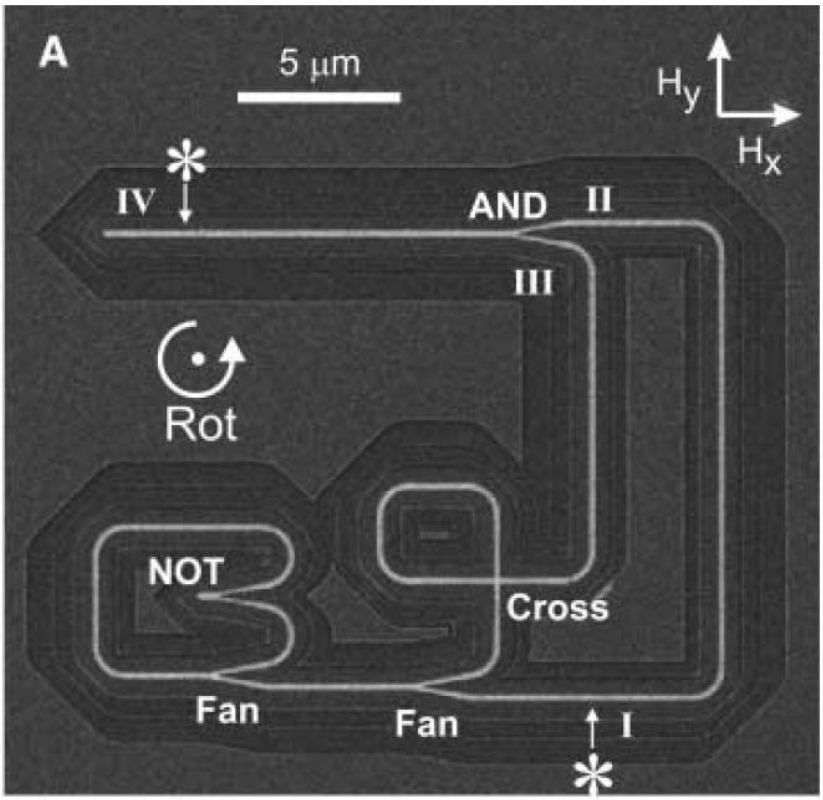

Figure 2.2. FIB image of a magnetic nanowire network containing domain wall logic elements [16].

According to the easy-axis (which is the energetically preferred direction of magnetic moment in materials and will be interpreted in the following paragraphs.) of ferromagnetic materials used for NML, NML can be further divided into two types, namely in-plane NML (iNML) and out-of-plane NML (oNML). The difference is depicted in Fig. 2.3. Here we take the two most contributive research group as representatives of each kind of field-coupled NML.

2.2.1 In-plane Nanomagnet Logic

I am grateful to Prof. Wolfgang Porod for initializing the research work on NML in University of Notre Dame, where Permalloy nanomagnets were firstly fabricated for information computing. Permalloy is a nickel-iron alloy, compositing 20% iron and 80% nickel. Based on their earlier extensive computational study [23] - [31] and experimental study [32] [33] [34] [35], the Notre Dame research

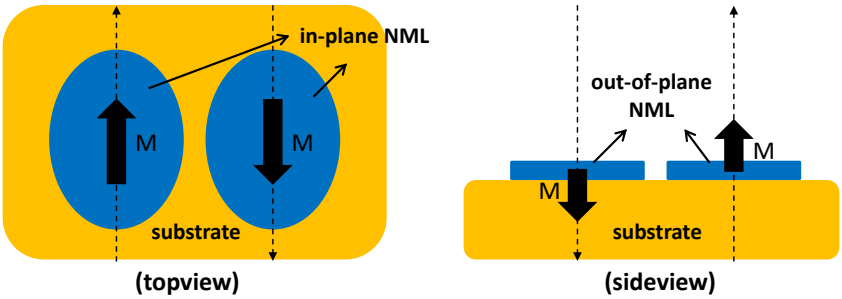

Figure 2.3. Field-coupled NML with (a) in-plane easy axis and (b) out-of-plane easy axis.

group presented a majority gate for MQCA in [36], where the state of output dot (nanomagnet) is determined by the majority vote of the three input dots owing to the magnetic interaction. The structure of this majority gate is shown in Fig. 2.4. The Permalloy dot is elongated. Due to the shape anisotropy (which will be introduced in detail in Chapter 3), the magnetization prefers to align long the long axis, which is energetically preferred and called the easy axis. Two energetically equivalent states along the easy axis stand for the two logic states in NML. With one of the input dots fixed to either logic '1' or logic '0', majority gate can accordingly operate as an OR gate or an AND gate. NOT gate can be realized by putting two dots 'head to tail'. Consequently, all the logic functions can be implemented by majority gates integrated with nanochains built with single-domain dots. To our knowledge, a full adder comprised of 53 magnets is the most complex magnetic circuit attempted to date [37].

The Permalloy dot-arrays are fabricated on silicon dioxide substrate by electron beam lithography on Poly(methyl methacrylate) (PMMA), e-beam evaporation of Permalloy and lift-off process. A line of nanomagnets is shown in Fig. 2.5. The size of each individual dot needs to be small enough (sub-100nm) so as to posses single-domain behavior, and the thickness is only about 20 nanometers. Due to the shape anisotropy, the magnetization of each Permalloy dot lies in-plane. Actually, most of the ferromagnetic materials with the same geometry, such as iron, nickel, and ferromagnetic alloys, all have an in-plane easy-axis.

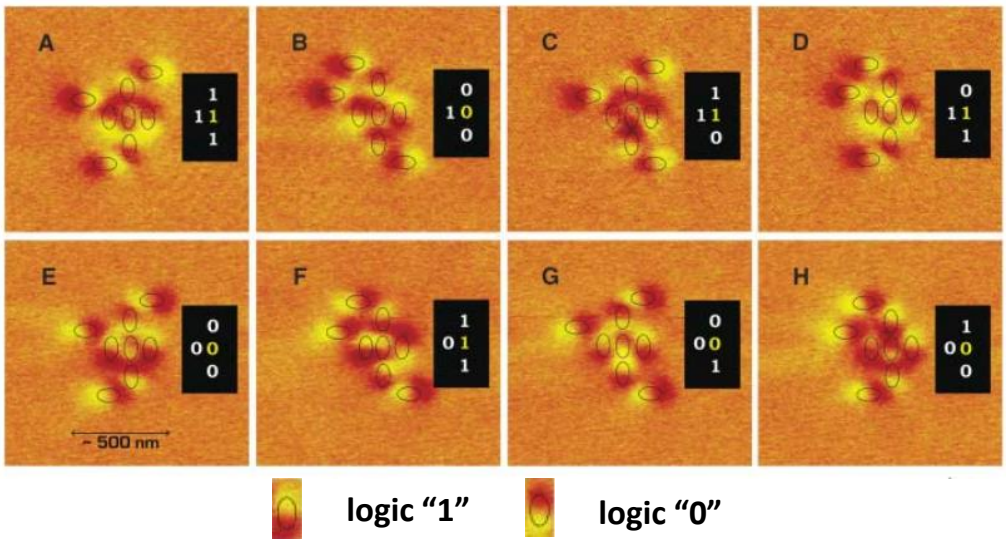

Figure 2.4. MFM images of a majority gate with different input configurations presented in [36]: The location of the magnets is drawn superimposed on the MFM data. Horizontally placed dots and an horizontal external field are required to write the input states.

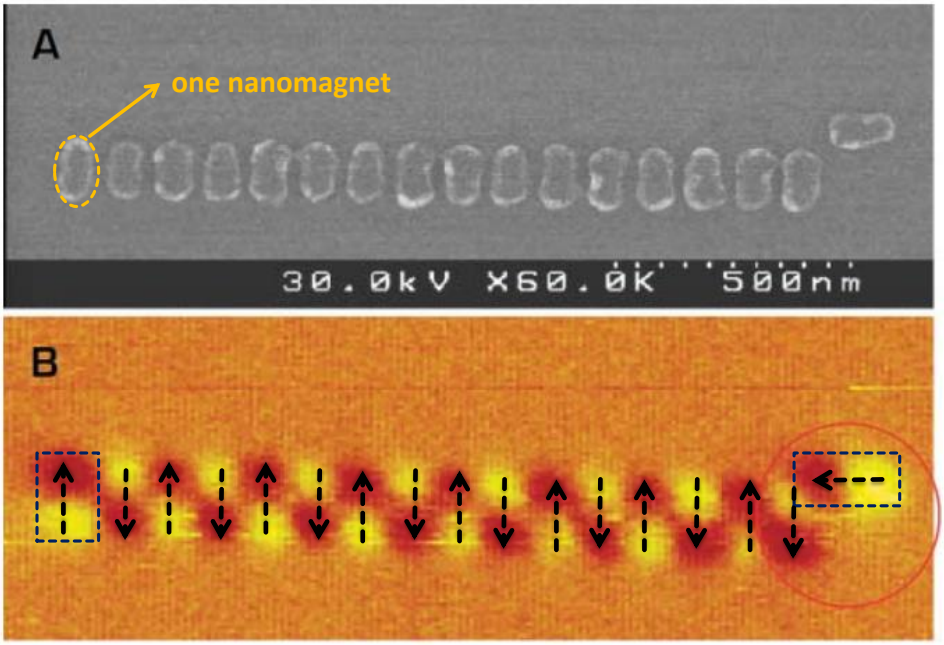

Figure 2.5. (A) Scanning electron microscope (SEM) image of a chain of 16 coupled Permalloy nanomagnets. (B) Magnetic force microscope (MFM) image of the same chain shows alternating magnetization in antiferromagnetic ordering as set by the state of the horizontal magnet (in the red circle) [36].

Recently, new techniques such as electroplating and nanoimprinting [38] are attempted in experiments as new approaches of fabricating large-scale dot-arrays, but the quality is still not as good as that fabricated from the conventional methods. Further improvement is required.

As one may have already noticed in Fig. 2.4, with a global external clocking filed, the horizontal dots (input dots) have to be placed at different positions in order to get all the input combinations. Local control of input dots is required to achieve all the logic configurations. Moreover, variations in nanomagnet shape and edge roughness, together with thermal fluctuations, lead to a variation of switching field from dot to dot. It is found even strongly coupled dots with high-quality lithography exhibit reliable magnetic ordering over only 10 to 20 magnets. Therefore, a large-scale device has to be operated by means of local clocking of subarrays that controls a few gates only. With a current pulse through metal wires, a magnetic field can be generated and acts as the local clocking signal. One sketch of local clocking structure is illustrated in Fig. 2.6, where current wires underneath generate clocking fields for the gates array.

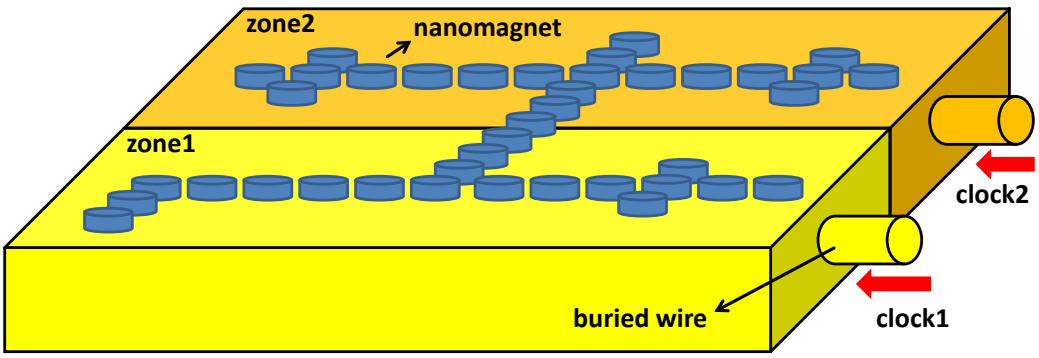

Figure 2.6. Clocking wires are buried underneath the nanomagnets. Each wire only clocks a number of nanomagnets in the corresponding zone.

The power dissipation in field-coupled nanomagnets is analyzed in [39] [40], where the method of adiabatic switching is outlined. However, the clocking signal

needs to be sufficient to drive the dots. In [41], the estimates for magnetic field that a current carrying wire could provide were made. In order to fulfill this request, the current density turns out to be on the order of 10^6 A/cm^2. Such a high current density causes a large amount of Joule heat and the wires become power-hungry.

More recently in [42] [43] [44] [45], the implementation of multiple-phase clocking was proposed and energy performance was analyzed, indicating NML technology has the potential to outperform low power CMOS equivalents with similar energy requirements. Potential approaches to have additional energy saving were also summarized:

1. A sidewall yoke structure allows current carrying wires to generate stronger magnetic fields so that the demand on current density is reduced.

2. Surrounding nanomagnets with high permeability materials (increasing the absolute permeability) offers another effectively way for lower energy dissipation. The study on enhanced permeability dielectric (EPD) materials [46] is ongoing.

3. The switching properties of nanomagnets are magnet-shape-dependent [47]. Shape engineering of the dots can further bring down the energy cost [48].

With shape engineering, the design of a non-majority gate was introduced in [48] [49] and experimentally demonstrated in [50]. This design can significantly reduce the footprint, increase operating speed, and improve the reliability.

2.2.2 Out-of-plane Nanomagnet Logic

Magnetic thin films with perpendicular magnetic anisotropy (PMA) are extensively studied in nanostructures and have been already applied in magnetic recording industry [51] [52] [53]. However, to our knowledge we are the first group employing out-of-plane field-coupled nanomagnets for logic computation.

Originally, it was expected to use pillar-shaped Permalloy dots with out-of-plane easy axis to enhance the coupling strength so as to implement logic computing [24]. However, the Permalloy pillars with high-aspect ratio turned out to be quite challenging for fabrication. Hence, the ultra-thin ferromagnetic media exhibiting PMA aroused our great interest. The PMA of these ultra-thin films results from inherent crystalline growth and layer configurations. Fig. 2.7 is a sketch showing the difference in contrast to the iNML nanomagnets. PMA films have been proposed in data storage applications to improve the recording density and sensitivity [54] [55] [56] [57]. Among these multilayer systems exhibiting PMA, Co/Pt, Co/Pd and Co/Ni have been the most studied as patterned recording media [58] [59] [60] [61] [62].

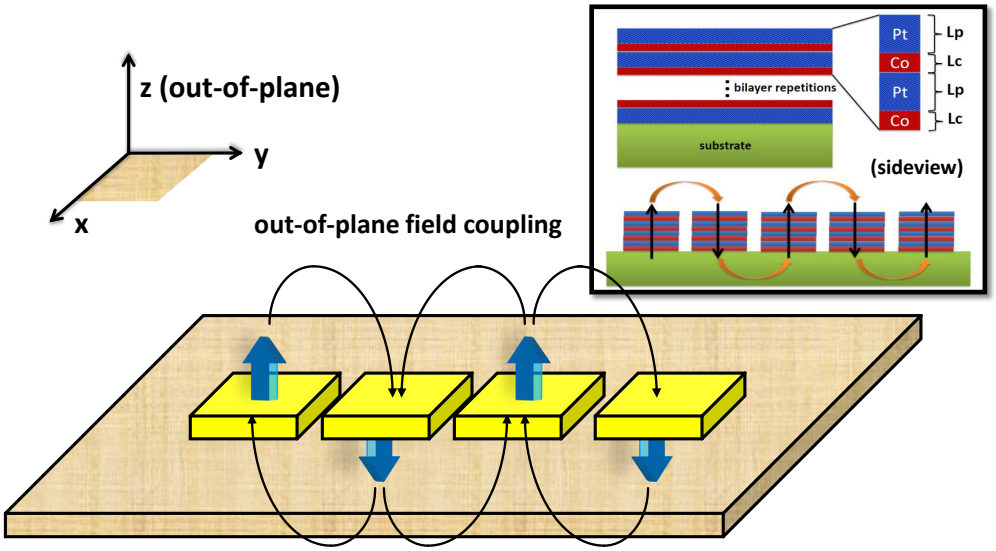

Figure 2.7. Field-coupled nanomagnets with out-of-plane easy axis. The inset demonstrates the layer composition of Co/Pt multilayer with PMA.

In [63], for the first time planar Co/Pt multilayer was suggested to replace three-dimensional magnetic pillars in magnetic logic devices. Ultra-thin Co layer (< 1.2 nm) sandwiched between Pt layers exhibits strong perpendicular anisotropy due to alloy formation and short-range interface effect. The layer composite of Co/Pt is sketched in the inset of Fig. 2.7. The complicated origin of magnetic

anisotropy is beyond the scope of this dissertation. For fundamental theory of ultra-thin magnetic film, see [64]. A wealth of experimental study on Co/Pt multilayers is well established in early 1990 mainly for magneto-optical drives [65] [66] [67] [68] [69], where the magnetic coupling between neighboring dots is taken as 'noise' and minimized. However, for NML applications, strong coupling is more than welcome. In experiments, the following prerequisites are expected to be satisfied for NML devices:

1. Narrow and precisely controlled separation between dots $\longrightarrow$ strong coupling
2. Low switching field variation (narrow switching field distribution) from dot to dot $\longrightarrow$ a better control of the dots switching.
3. Low switching field of dots, but meanwhile being robust against thermal fluctuations $\longrightarrow$ lower power dissipation
4. The reversal behavior should be somehow well adjustable $\longrightarrow$ precise control and more flexibility in design

In the year 2005, Dr. Markus Becherer pioneered the experimental study on out-of-plane NML with Co/Pt multilayer-based nanomagnets at Technische Universität München. After Co/Pt film deposition with sputtering, patterning the dots can be done by chemical etching, lift-off, focused ion beam (FIB) irradiation, or combinations of these techniques. The technique using focused ion beam irradiation provides the advantage without actually removing any material from the surface. It is known the magnetic properties of Co/Pt films can be changed by local ions irradiation [70]. Generally speaking, the irradiation intermixes the layers and leads to a decrease of perpendicular anisotropy. Consequently, the film turns softer and its coercivity reduces. A sufficiently high dose of FIB irradiation can even entirely eliminate the perpendicular anisotropy. Since the highly irradiated part can be assumed non-magnetic, this process is utilized to 'cut' the dots from the continuous Co/Pt films. In [71], a long-range checker-board patterned by FIB

was presented, indicating a strong coupling and acceptable switching field distribution (SFD). This fulfills prerequisite 1 and 2. Experiments verified a separation of $10 - 20$ nm is achievable by FIB cutting.

In as-grown Co/Pt films, the nucleation event starts at randomly distributed sites due to spatial inhomogeneity of the layers. These sites are usually called pinning sites. The dots containing pinning sites may switch at a lower nucleation field. Meanwhile, the FIB patterning arises the roughness at edges: a number of non-focused ions irradiate the edges and locally change the magnetic properties there. Both of the two factors broaden the SFD. However, this problem can be solved by local irradiation. With a proper ion dose, local irradiation can artificially lower the coercivity and create a weakest site which dominates over the other pinning sites and soft edges. The reversal behavior of dots can be engineered with creating nucleation sites, which potentially further optimizes the SFD and more importantly, brings down the nucleation field (coercivity), meeting the needs of prerequisite 3.

Furthermore, local nucleation sites can be designed and placed at different parts of dots, which we call partial irradiation. Partial irradiation can change the coupling strength from neighboring dots and contribute to an asymmetrical coupling, which ensures uni-directional information flow and offers more freedom in NML circuit design (prerequisite 4). The NML design with partially irradiated dots is the highlight of this dissertation, and we will look into details in the later chapters.

In experiments, a tailer-made extraordinary Hall-effect sensor (EHE) [72] and Magneto-optical Kerr effect (MOKE) setup are in use for magnetization measurements. The magnetic characteristics of field-coupled Co/Pt multilayer dots, such as the reversal behavior and switching field distribution (SFD) are fully studied in [73] [74] [75] [76] [77] [78] [79]. With the support of plenteous experimental data, we carried out computational study and developed a specific model for Co/Pt dots with FIB irradiation [80]. So far, we haven't found any other publication

particularly dealing with modeling of the reversal behavior of Co/Pt multilayer structures. Our computational study shows in principle non-reciprocal coupling from partially irradiated dots can result in error-free NML with great reliability, where the ordering frustrations [81] can be completely wiped out in an effective global clocking [82].

The initial study of coupling behavior of partially irradiated dots is discussed in [83]. More recently, basic NML elements, such as an inverter chain [84], a majority gate [85] and fanout structure [86] are experimentally demonstrated, verifying the feasibility of non-reciprocal coupling in partially irradiated Co/Pt dots. More experiments are ongoing towards large-scale NML circuits.

CHAPTER 3

MICROMAGNETIC THEORY

3.1 Theory of ferromagnetism

The spin of an electron, combined with its electric charge, is the origin of magnetism. In physics, different types of magnetism are briefly distinguished as diamagnetism, paramagnetism, ferromagnetism (including ferrimagnetism) and anti-ferromagnetism. Ferromagnetism is the only type that creates magnetic field strong enough to be felt, and is the basis of many electronic and electromechanical devices, such as electromagnets, electronic motors and transformers, and nowadays magnetic storage devices.

There was no real progress in understanding ferromagnetism until Pierre Weiss made his hypothesis of the molecular field in 1906 [87]. This hypothesis can be summarized as two assumptions: (a) spontaneous magnetization – a molecular field acts in a ferromagnetic substance, and this field is so strong that it can magnetize the substance to saturation; (b) division into domains – a ferromagnet in the demagnetized state is divided into a number of small regions called domains. Each domain is spontaneously magnetized to the saturation value M_s, but the directions of magnetization of the various domains are randomly distributed so that the specimen as a whole has no net magnetization.

However, the Weiss theory of the molecular field says nothing about the physical origin of this field. The physical origin was not understood until 1928, when Heisenberg showed it was caused by quantum-mechanical exchange force, which is entirely nonclassical and dependent on the relative orientation of the spins of electrons. Exchange force is a consequence of the Pauli exclusion principle, applied

to two atoms as a whole. This principle states that two electrons can have the same energy only if they have opposite spins. The term 'exchange' arises by considering the two electrons in adjacent atoms exchange places. This consideration introduces the energy term into the expression for the total energy of two atoms. If two atom i and j have spin angular momentum $\mathbf{S}_\mathrm{i}h/2\pi$ and $\mathbf{S}_\mathrm{j}h/2\pi$ respectively, then the exchange energy is given by

$$E_\mathrm{ex} = -2J_\mathrm{ex}\mathbf{S}_\mathrm{i}\mathbf{S}_\mathrm{j} = -2J\mathbf{S}_\mathrm{i}\mathbf{S}_\mathrm{j}\mathrm{cos}\phi \tag{3.1}$$

where J_ex is called exchange integral, which occurs in the calculation of the exchange effect, and ϕ is the angle between the spins. If J_ex is positive, E_ex is a minimum when the spins are parallel ($cos\phi = 1$) and a maximum when they are antiparallel ($cos\phi = -1$). If J_ex is negative, the lowest energy state is the result of antiparallel spins. In ferromagnetic materials, J_ex is positive so that exchange forces cause the spins to be parallel, which is also a rare condition because J_ex is usually negative in other materials.

Both Weiss theory and Heisenberg approach are based on the assumption of localized moments. However, the localized moment theory cannot explain the fact that the observed moments per atom $\mu_\mathbf{H}$ in metals are nonintegers. In order to remove this question mark, the band theory [88] is applied to give a reasonable explanation. Firstly back to Pauli exclusion principle: no two electrons in the atom can have the same set of four quantum numbers. Three of them define the shell, while the fourth defines the spin state. In other words, each energy level in an atom can hold a maximum of two electrons with opposite spins. According to this, in solids the energy levels split to bands. For instance, in nickel the split $3d$ and $4s$ bands overlap in energy. By calculating the density of levels as a function of energy, it can be found that the number of electrons in $3d$ is a noninterger and the shell is half full. The unbalanced spins in half full bands are the main source of ferromagnetism (as illustrated in Fig. 3.1). The ferromagnetism of the most

common ferromagnetic material Fe, Co and Ni is due to the spin unbalance from $3d$ band. All of them satisfy the following criteria:

- Unbalanced spins in partially filled $3d$ band result in a net magnetic moment.
- The atoms are at a proper distance apart so that exchange force can align the d-electron spins.

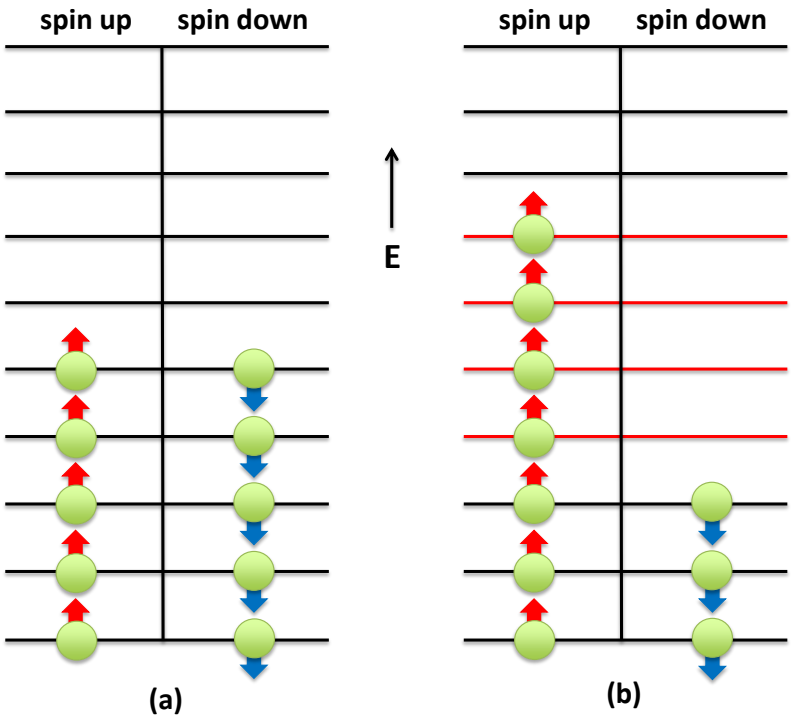

Figure 3.1. $3d$ energy band with (a) balanced and (b) imbalanced spins.

However, of all the transient elements, only Fe, Co and Ni meet the second requirement. Many of the rare earths are ferromagnetic below room temperature, where the spontaneous magnetization is due to spin unbalance in their $4f$ bands. Ferromagnetism is also found in the binary and ternary alloys of Fe, Co, and Ni with one another, in alloys of Fe, Co and Ni with other elements. Some of the alloys can even be tailor-made to achieve better characteristics for specific applications [89] [90].

The most employed Permalloy in iNML is composed of about 80% Ni and 20% Fe, while in this dissertation our interest lies on Co/Pt multilayer for oNML, which

is made of ferromagnetic Co and non-magnetic Pt. Both Permalloy and Co/Pt multilayer exhibit strong magnetic coupling and potentially low switching fields, which are quite suitable for NML applications.

3.2 Energetics in ferromagnetic materials

In micromagnetics, the total energy E_{total} in magnetic materials is the resultant of several different energy terms. The arrangement of elementary moments is characterized by the classical magnetization distribution of function $\mathbf{M}(\mathbf{r}, t)$. Magnetization equilibrium means the magnetic torque per unit volume acting in the material vanishes and the free energy arrives at the minimum. In magnetization equilibrium, the density of moments in a homogeneous material is constant everywhere, $|\mathbf{M}(\mathbf{r}, t)| = M_s$ is called saturation magnetization of the material. Any static micromagnetic problem can be solved by seeking this final equilibrium state.

The system energy E_{total} can be described as the sum of all these terms below:

$$E_{\text{total}} = E_{\text{demag}} + E_{\text{ex}} + E_{\text{anis}} + E_{\text{Zeeman}} + E_{\text{therm}}. \tag{3.2}$$

In this equation, E_{demag}, E_{ex}, E_{anis}, E_{Zeeman} and E_{therm} are demagnetizing energy, exchange energy, anisotropy energy, Zeeman energy and thermal energy respectively.

3.2.1 Demagnetizing energy

Demagnetizing energy is also called dipolar energy, which arises from the force between magnetic dipoles (also called dipole-dipole magnetic interaction). This force acts in a long-range and tends to align spins 'head-to-tail'. Therefore, it exerts a demagnetizing effect and contributes to demagnetizing energy.

The demagnetizing energy between two adjacent dipoles is written as:

$$E_{\text{demag}}^{\text{i,j}} = \mu_0 \left[\frac{\mu_{\text{i}} \mu_{\text{j}}}{|r_{\text{ij}}|^3} - \frac{3\left(\mu_{\text{i}} r_{\text{ij}}\right)\left(\mu_{\text{j}} r_{\text{ij}}\right)}{|r_{\text{ij}}|^5} \right], \tag{3.3}$$

where μ_{i} and μ_{j} are the magnetic moment of the two dipoles and r_{ij} is the distance in between. The total demagnetizing energy is calculated by extending the sum of each dipole to all the possible combinations of other dipoles within the scope of demagnetization force, as shown in Eq. 3.4:

$$E_{\mathrm{demag}} = \frac{1}{2}\sum_{\mathrm{i}}\sum_{\mathrm{j}\neq\mathrm{i}} E^{\mathrm{i,j}}_{\mathrm{demag}}. \tag{3.4}$$

3.2.2 Exchange energy

In Section 3.1, the exchange interaction has already been briefly talked about. In ferromagnetic materials, according to Pauli exclusion principle, two electrons with the same spin cannot have the same 'position'. Therefore under certain conditions, when the orbitals of the unpaired outer valence electrons from adjacent atoms overlap, the distribution of their electric charge are further apart in space when the spins are parallel aligned than anti-parallel aligned. This reduces the electrostatic energy, so the spins of electrons tend to line up. This difference in energy is called the exchange energy.

Exchange interaction is very strong and dominates over classical dipole-dipole interaction in short distances, aligning nearby spins parallel to each other:

$$\mathbf{H}_{\mathrm{exch}} = \frac{2A_{\mathrm{exch}}}{M_s^2}\nabla^2\mathrm{M}(\mathbf{r}), \tag{3.5}$$

where A_{exch} is called 'exchange stiffness' and it is a material dependent parameter. The short-range exchange interaction is only active within the distance called exchange length λ_{ex}, which equals to:

$$\lambda_{\mathrm{ex}} = \sqrt{\frac{A_{\mathrm{exch}}}{\frac{1}{2}\mu_0 M_s^2}}. \tag{3.6}$$

For Permalloy and Co/Pt, λ_{ex} is in the range of a few nanometers.

In Eq. 3.1, the exchange energy in a two-atom system is already given. The total energy contribution due to the exchange interaction is described by the Heisen-

berg model in a simple formulation as:

$$E_{\mathrm{ex}} = -J_{\mathrm{ex}} \sum_{\mathrm{i,j}} \mathbf{S}_{\mathrm{i}} \mathbf{S}_{\mathrm{j}} \tag{3.7}$$

where J_{ex} is also called exchange constant, $\mathbf{S}_{\mathrm{i}}$ and $\mathbf{S}_{\mathrm{j}}$ are neighboring spins vectors.

3.2.3 Anisotropy energy

Although the exchange interaction keeps spins aligned, it doesn't align them in a particular direction. Magnetic anisotropy is the dependence of the internal energy on the direction of the magnetization vector. There are several magnetic anisotropy existing in ferromagnetic materials. The most common ones are listed below:

- Magnetocrystalline anisotropy: This is the dependence of the energy on the specific direction of magnetization relative to the lattice crystallization (intrinsic to the material), which is the most common one and also called crystal anisotropy. Magnetocrystalline anisotropy is mainly due to the spin-orbit coupling.

- Shape anisotropy: It exists in single-domain magnets due to magnetostatic effects of the shape. Assume there is no net magnetocrystalline anisotropy in a spherical ferromagnetic specimen, the same applied field will magnetize the same extent in any direction. But if it is non-spherical, it will be easier to magnetize along a long axis than along a short axis, because the demagnetizing field along a short axis is stronger than along a long axis. Therefore, the applied field along a short axis has to be stronger to produce the same true field inside the specimen. The shape alone can be a source of magnetic anisotropy. Actually, shape anisotropy just originates from the unbalanced demagnetizing fields in each direction. The elongated shaped Permalloy dots in NML straightforwardly utilize this shape effect.

- Stress anisotropy: Also called inverse magnetostriction, this term is induced by internal strains.

- Anisotropy induced by irradiation, magnetic annealing, plastic deformation and other extrinsic processes. Particularly, as in our work, engineering the anisotropy of Co/Pt multilayer is via one of the extrinsic processes – FIB irradiation.

Co/Pt multilayer is with uniaxial anisotropy perpendicular to the film plane. The energy term E_{anis} is customarily written as

$$E_{\text{anis}} = K_0 + K_1 \cdot \sin^2\theta + K_2 \cdot \sin^4\theta + \cdots, \tag{3.8}$$

where K_0, K_1, K_2, $\cdots$ are constants at a particular temperature and are expressed in J/m^3. Usually only K_0, K_1 and K_2 are considered, since the rest terms are negligible. The angle θ is between the magnetization vector and the easy axis. E_{anis} is minimum when $\theta = 0$.

3.2.4 Zeeman energy

By applying an external field, the atomic magnetic moments tend to align to the direction of the external field, resulting in an increase of the system energy. This increased part is called E_{Zeeman}, and E_{Zeeman} of a magnetized body in an external field $\mathbf{H}$ is formulated as:

$$E_{\text{Zeeman}} = -\mu_0 \int_V M \cdot \mathbf{H}\, \mathrm{d}V, \tag{3.9}$$

where the integral is done over the volume of the body.

3.2.5 Thermal energy

Thermal energy comes from the thermal fluctuations acting on the material. At non-zero temperature, thermal fluctuations lead to vibrations of magnetic moments in a random manner. Temperature-induced effects can result in complex

influence on magnetic behaviors. E.g., thermal fluctuations can eliminate some unstable metastable states; it also influences the coercivity and broadens the switching field distribution; in very small volume, it can wipe out other energy terms and bring about so called superparamagnetic behavior. The thermal fluctuations can be treated as a Gaussian white noise, with a given variance. This variance depends on the temperature and the volume of the material. Usually, the time scale of fluctuation Δt is approximately 10^{-12} second.

We will later on look into those temperature-induce effects, which play an important role in NML.

3.3 Magnetization dynamics: Laudau-Lifshitz-Gilbert Equation

In time-varying regime, the dynamic evolution in ferromagnetic materials is described by the Landau-Lifshitz (LL) equation, which predicts the rotation of the magnetization in response to torques, or in other words, how the magnetization vector $\mathbf{M}(\mathbf{r}, t)$ changes according to time under the influence of an effective field $\mathbf{H}_{\text{eff}}(\mathbf{r}, t)$.

In micromagnetics, the effective field $\mathbf{H}_{\text{eff}}(\mathbf{r}, t)$ represents the sum of all field terms on the magnetization vector:

$$\mathbf{H}_{\text{eff}} = \mathbf{H}_{\text{exch}} + \mathbf{H}_{\text{Zeeman}} + \mathbf{H}_{\text{demag}} + \mathbf{H}_{\text{anis}} + \mathbf{H}_{\text{therm}}. \tag{3.10}$$

In Eq. 3.10, $\mathbf{H}_{\text{exch}}$ stands for the exchange interaction and is proportional to exchange stiffness A_{exch}. $\mathbf{H}_{\text{Zeeman}}$ and $\mathbf{H}_{\text{demag}}$ take into account of external magnetic field and dipole-dipole magnetic field. These two terms together are also called Maxwell magnetic field $\mathbf{H}_{\text{Maxwell}}$, which can be derived from Maxwell's equation. $\mathbf{H}_{\text{anis}}$ is responsible for the anisotropy nature of the material and $\mathbf{H}_{\text{therm}}$ originates from thermal fluctuations. Each field term contributes to the corresponding energy term discussed in Section 3.2.

Landau-Lifshitz equation is described as follows:

$$\frac{\partial \mathbf{M}(\mathbf{r},t)}{\partial t} = -\gamma \mathbf{M}(\mathbf{r},t) \times \mathbf{H}_{\text{eff}}(\mathbf{r},t) - \frac{\alpha\gamma}{M_s}\left[\mathbf{M}(\mathbf{r},t) \times (\mathbf{M}(\mathbf{r},t) \times \mathbf{H}_{\text{eff}}(\mathbf{r},t))\right], \quad (3.11)$$

where γ is the gyromagnetic ratio with the value of $\gamma = 2.210 \cdot 10^5$ $\mathrm{T}^{-1}\mathrm{s}^{-1}$ and α is the damping constant.

LL equation is the most fundamental and important equation describing the micromagnetic dynamics. It can be further interpreted into two terms: the first term $-\gamma \mathbf{M}(\mathbf{r},t) \times \mathbf{H}_{\text{eff}}(\mathbf{r},t)$ describes the precession movement of the magnetization vector $\mathbf{M}(\mathbf{r},t)$ around effective field vector $\mathbf{H}_{\text{eff}}(\mathbf{r},t)$. Hence, it is called precession term. The force is all the way perpendicular to the direction of the processional rotation and there is no power lost. The rest part of LL equation is the damping term, which gives a description how the magnetization vector tends to bend towards the effective field. This damping term dissipates energy. In the end, the magnetization vector lies in the same direction of the effective field so as to reach the lowest steady energy state. Fig. 3.2 illustrates these two terms of dynamics.

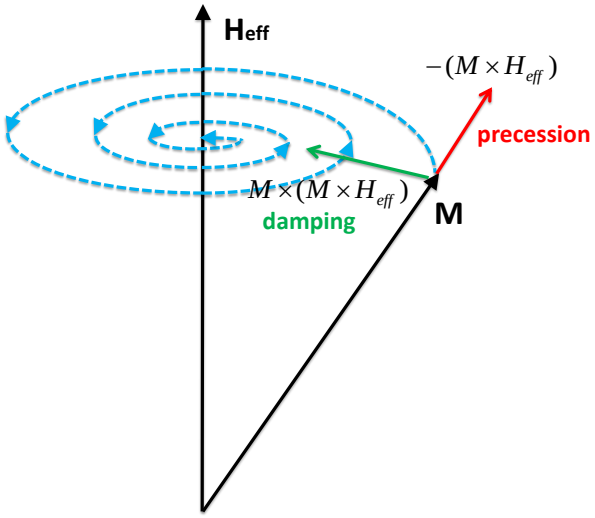

Figure 3.2. The damped precession in magnetic dynamics.

The damping constant α is a 'lumped' effect that takes into account many

phenomena that lead to dissipation. For most of materials, α is in the range of $0.005 - 0.1$.

T. L. Gilbert replaced the damping term in LL equation by one that depends on the time dependence of the magnetic field. It can be transformed into the same form of the LL equation, which best represents the behavior when the damping constant is large. This complete form is called Laudau-Lifshitz-Gilbert (LLG) equation.

3.4 Domain theory in ferromagnetic materials

It was already mentioned in Section 3.2 the competition between demagnetizing field and exchange interaction: demagnetizing field tends to align the spins 'head-to-tail', but exchange interaction lines up spins in the parallel manner. This competition is the origin of the complexity of domain behaviors in ferromagnetic substances.

3.4.1 Single-domain behavior

In a certain small volume, the long-range demagnetizing field is dominated by the short-range but very strong local exchange interaction and / or strong anisotropy. As a result, all the spins of dipoles align in the same direction, and the magnetic moments reach the maximum. This phenomenon is called single-domain behavior. The magnetization in single-domain particles can be characterized by scalar numbers instead of a vector field. It is usually considered that structures smaller than a few times of the exchange length λ_{ex} are well in the single domain regime.

A single-domain particle changes its state by rotating all the magnetization as an unit, resulting in a very large coercivity. The most widely used theory for hysteresis in the single-domain state is the Stoner-Wohlfarth model [91]. This applies to particles with uniaxial magnetocrystalline anisotropy. These particles exhibit abrupt switching along the easy axis, shown in Fig. 3.3

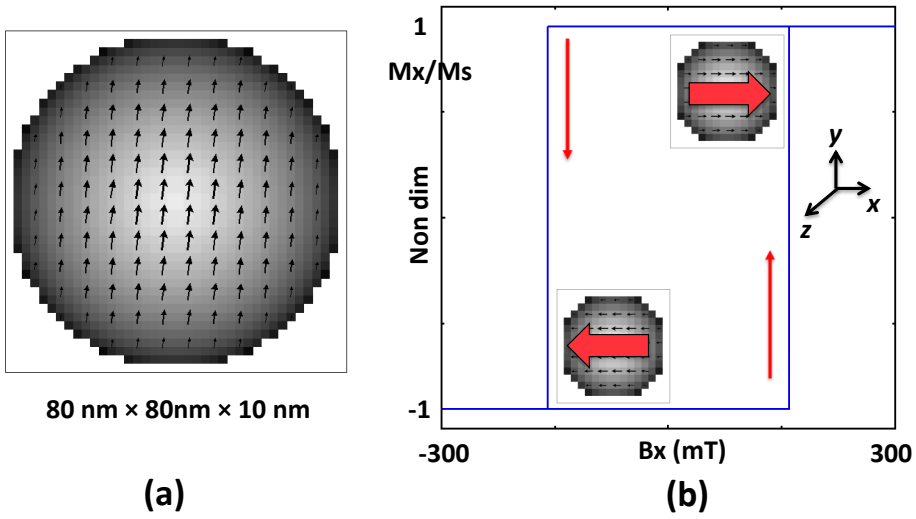

Figure 3.3. (a) Spin orientation in a single-domain particle. (b) Abrupt switching in single-domain hysteresis.

Such single-domain particles act as the main characters in lots of applications due to their high coercivity. They are the main source of hardness in hard magnets, the information carrier in not only memory devices but also our NML design. In Chapter 4, the hysteresis of single-domain nanomagnets will be thoroughly discussed.

3.4.2 Limits on the single-domain size

The size range, in which a ferromagnet exhibits the single-domain phenomenon, is from a few tens of nanometers up to several hundred-nanometers or so. This size range is bounded below by the transition to superparamagnetism and above by the formation of multiple-domain patterns.

As explained in Section 3.2.5, thermal fluctuations cause the magnetization vector to 'dance' around the easy axis randomly. In the single-domain state, the moment seldom strays far away from the stable state. Energy barriers prevent the magnetization from jumping from one state to another. However, if the energy barrier gets small enough, the magnetic moment can jump from state to state frequently, approaching superparamagnetic. The jump frequency is exponentially dependent on the height of energy barrier, and the energy barrier is proportional to

the volume of ferromagnet. Therefore, transition occurs when the volume reaches the critical value. This value is the lower limit of single-domain range.

On the other hand, as the size of a ferromagnet increases, the single-domain state incurs an increasing energy cost due to the demagnetizing field. This field tends to rotate the magnetization in such a way that the total moment of the ferromagnet reduces. Hence, in larger magnets the magnetization is organized in magnetic domains. As the demagnetizing energy and the exchange energy reach a balance, a favored multiple domain is formed. In other words, above a certain critical size, the total energy of remaining in single-domain state is larger compared with the total energy of a certain multiple-domain state, so the latter one is energetically preferred and it tends to be multiple-domain. Fig. 3.4 demonstrates the simulated multiple-domain pattern in a Permalloy film.

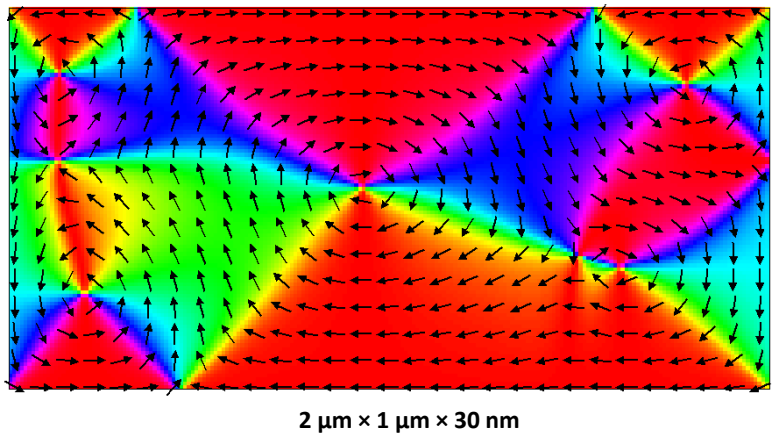

Figure 3.4. Simulated relaxed multiple-domain pattern in a 2 μm$\times$ 1 μm $\times$ 30 nm Permalloy film. The colors indicate the orientation of spins.

For NML design, it is required that the size of fabricated nanomagnets lies in the single-domain range, and at best far apart from these two critical limits in order to reduce the possibility turning to the wrong states. We will have a further discussion how the error rate is related to dot size in NML computing in later part of this dissertation.

3.4.3 Magnetic domain wall

In multiple-domain structures, the transition interfaces of magnetic moments with different orientations are called domain walls. Domain wall is a gradual re-orientation of two adjacent domains across a finite distance. This distance usually refers to the width of a domain wall, and it is dependent on three energy terms, i.e. magnetocrystalline energy, anisotropy energy and exchange energy. All of these energy terms tend to be as low as possible so as to be a more favorable energetic state. The magnetocrystalline energy and anisotropy energy is lowest when the individual magnetic moments are aligned with the crystal lattice axes anti-parallel thus reducing the width of the wall. Whereas the exchange energy prefer to align the magnetic moments parallel to each other and thus makes the wall thicker due to the repulsion between them. In the end, an equilibrium is reached and the width is set.

The domain wall energy can be calculated by the difference before and after the domain wall is created. An ideal domain wall is independent of position. However, the unavoidable imperfections known as defects (or pinning sites) in the medium can prevent the formation of a wall and inhibit its propagation. Consequently, a greater external field is usually required to overcome these sites.

Distinguished by the rotation axis of the magnetic moments with respect to the normal vector which defines the plane of the wall, domain walls can be classified into two types: Bloch wall and Néel wall [92]. For a Bloch wall, the magnetic moments rotate along an axis which is perpendicular to the normal vector, unlike that in an Néel wall where the rotation axis is parallel to the plane of wall. The gradual rotation of these two kind of walls is sketched in Fig. 3.5. There also exists domain walls appearing a mix-type [93], but it is not under discussion here.

3.5 Micromagnetic simulation packages

With the recent rising of spintronics, micromagnetic simulations play an significant role in better understand the sub-micron regime. To date, several well

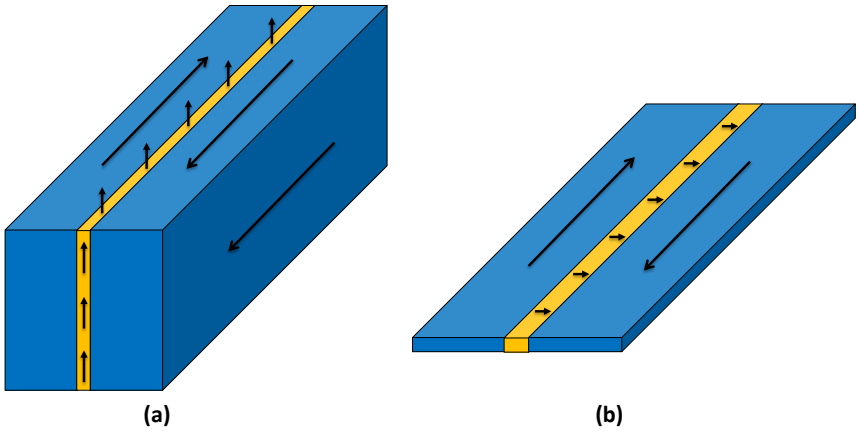

Figure 3.5. (a) Bloch wall. Note free poles appearing where the wall intersects the surfaces. (b) Néel wall in thin sample. Free poles appear along the surface of the wall.

developed micromagnetic simulators are extensively used, such as the OOMMF (Object Oriented MicroMagnetic Framework) [94], LLG micromagnetic simulator [95] and Nmag simulation packages [96].

Through our work, the release of OOMMF 1.2 alpha 3 and most recently, the latest developed snapshot of OOMMF 1.2 alpha 4-pre [97] have been used as the main interface of our micromagnetic simulations . In order to carry out more flexible and more specific three-dimensional simulations, Matlab-based script is prepared with point-wise changing micromagnetic parameters and afterwards loaded by OOMMF eXtensible Solver Interactive Interface (Oxsii). Note in all these simulations, we assume the temperature is at zero Kelvin, i.e. the temperature-induced effects are not taken into account.

In order to study the temperature-induced effects and verify the feasibility of NML operating at room temperature, simulations are implemented in an extension module of OOMMF – thetaevolve release developed from University of Hamburg [98]. We will present some related study in Chapter 4.

The particular flow of simulation procedures is given in Fig. 3.6. Note in the simulations throughout this dissertation, magnetic fields are expressed in teslas. Free-space values of magnetic field and flux density are converted using the $B =$

$\mu_0 H$ relation.

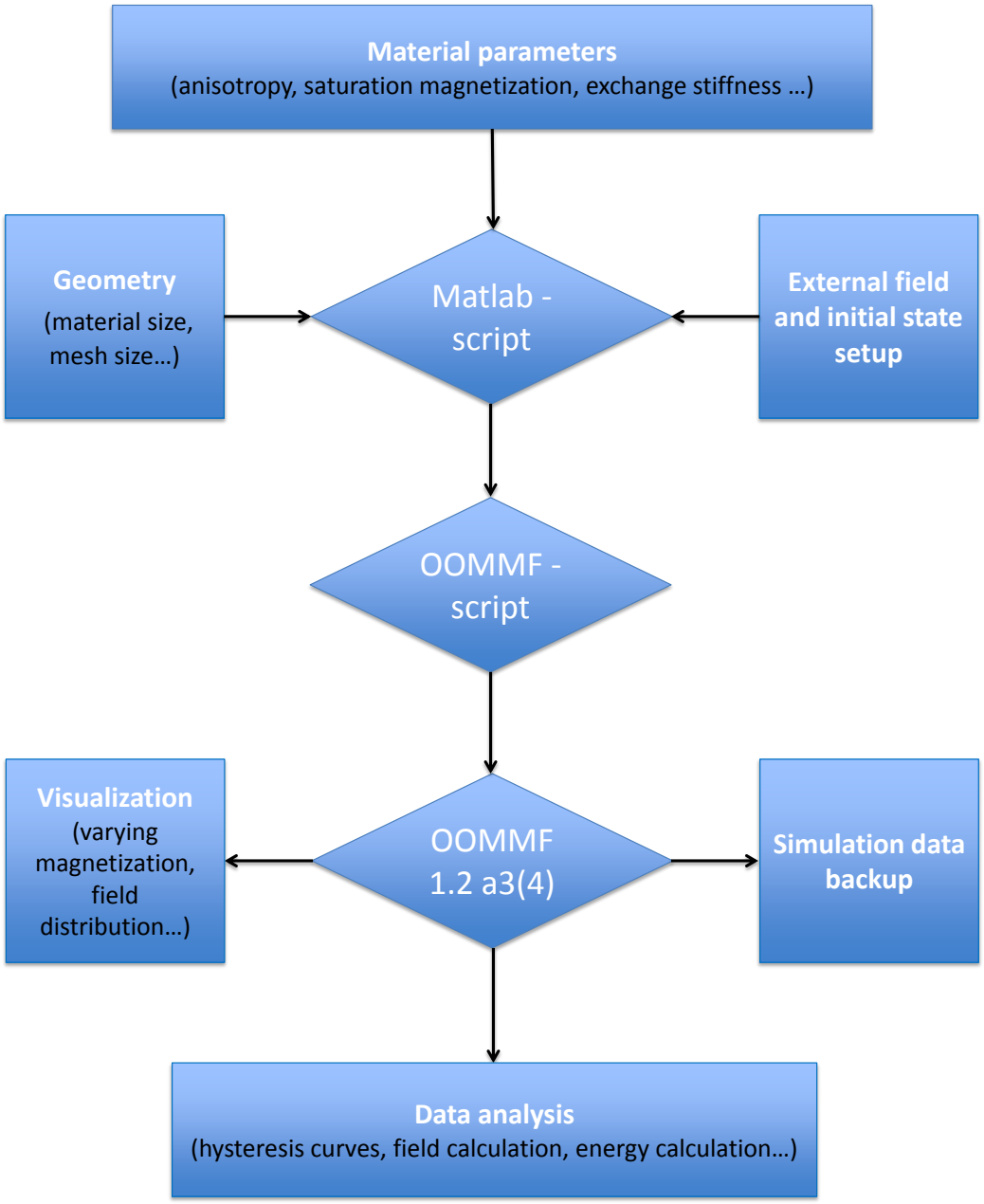

Figure 3.6. A brief simulation flowchart.

In addition, Nmag is used for some specific three-dimensional structures, e.g. the three-dimensional domain-wall clocking structure involved in Chapter 7.

CHAPTER 4

FIELD-COUPLED Co/Pt MULTILAYER NANOMAGNETS

In Chapter 2, the fabrication process of Co/Pt nanomagnets is briefly reviewed. Here, a particular description of the fabrication process of 5 multilayer (ML) Co/Pt nanomagnets is given. This multilayer system is chosen to illustrate how to calibrate the magnetic parameters in our micromagnetic simulation model. With these calibrated simulation parameters, the reversal behavior of a single standalone dot and field-coupled dots is presented.

4.1 Fabrication of Co/Pt multilayer films

In our group, the Co/Pt multilayers are fabricated in a similar process as described in [68]. Co/Pt multilayers are RF-magnetron sputtered using an Alcatel A450 system at a base pressure of 2.3×10^{-7} mbar with substrate temperatures ranging from room temperature to 200 °C. Unless otherwise indicated, multilayer structures are grown on silicon substrate at room temperature with the composition of $\mathrm{Pt}_{5\mathrm{nm}} n\times [\mathrm{Co}_{0.3\mathrm{nm}} + \mathrm{Pt}_{0.8\mathrm{nm}}]\, \mathrm{Pt}_{4.5\mathrm{nm}}$, where the Pt layer at the bottom and top are seeding layer and capping layer respectively. The cross-section view of n ML Co/Pt stacks is shown in Fig. 4.1. Here n stands for the number of cobalt and platinum bilayer repetitions. This number decides the thickness of the multilayers.

In [99], the dependence of the as-grown domain size of Co/Pt multilayer on the layer composition (where similar composition was used) was fully studied. The domain patterns of Co/Pt multilayer films vary as the thickness changes. Fig. 4.2 presents the trend, where the thickness stands only for $n\times [\mathrm{Co}_{0.3\mathrm{nm}} + \mathrm{Pt}_{0.8\mathrm{nm}}]$, which is the effective part. This curve in Fig. 4.2 can be distinguished into two

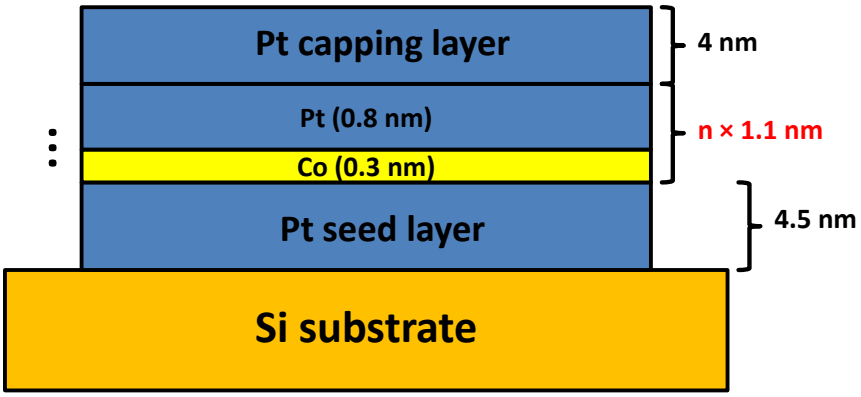

Figure 4.1. n multilayer Co/Pt stacks.

parts in the trend, separated by the red dash line. The single-domain size initially decreases dramatically as the total thickness increases up to about 30 nm. At the turning point, the single-domain size reaches the minimum value of sub-100 nm. As the thickness keeps rising from 30 nm, the single-domain size appears a linear and slow increase.

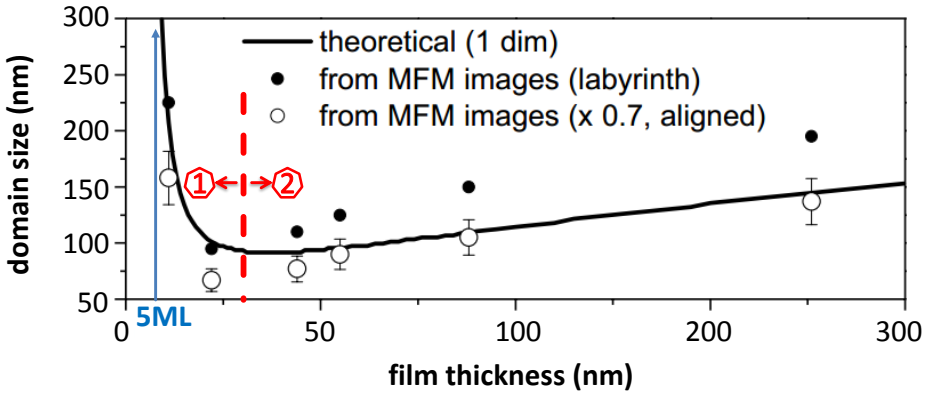

Figure 4.2. Domain size versus the Co/Pt multilayer thickness from [99].

Based on this characteristics and return to the elementary request of NML devices: the dots experiencing thermal noise at room temperature need to stay in a robust single-domain state. Therefore, multilayers with larger natural domain sizes are favorable. In our experiments, the proper number of n was chosen as 5

(correspondingly, the total thickness is around 5.5 nm), with which the theoretical domain-size is above 300 nm. However, 5 ML Co/Pt films actually present natural domain sizes larger than 1 μm in experiments.

4.2 Micromagnetic parameters of Co/Pt multilayer nanomagnets

Following Chapter 2, single-domain states of nanomagnets stand for the logic states in NML. Strong magnetic field coupling is expected among the magnets, resulting in a good ordering. In micromagnetic simulations, the central issue is to find the precise values of micromagnetic parameters, such as the saturation magnetization M_s, the anisotropy constant K and the exchange stiffness A_{exch}, which decide the coupling strength and reversal characteristics of single-domain nanomagnets.

The simulation of magnetic multilayers is somewhat more involved than the modeling of bulk magnetic materials owing to the complicated interface effect. It is possible to measure most of the micromagnetic parameters directly via experiments [100] [101]. However, some of the magnetic parameters of Co/Pt multilayer system, such as the anisotropy and the exchange constant, strongly depend on the layer thickness, number of layer repetitions and deposition conditions. A change of one of those factors may lead to a significant difference to the magnetic properties. Meanwhile, some of these measurements are quite tricky and time-consuming, it's inefficient to implement all the measurements for every piece of fabricated samples. Compared with direct measurements, fitting experimental hysteresis curves with micromagnetic simulations offers a more efficient way for our study. Following the calibration procedure in [71], standard micromagnetic simulators can be used to simulate multilayer materials.

To study the parameter dependency of Co/Pt multilayer reversal, here we first implement hysteresis simulations with a simple model, where we assume all the micromagnetic parameters are constants in homogeneously as-grown Co/Pt films.

Saturation magnetization $\mathbf{M_s}$

Saturation magnetization of Co/Pt films can be estimated from the ratio between the total layer thickness of cobalt (t_{Co}) and the total thickness of the multilayer ($t_{\mathrm{Co+Pt}}$), as in Eq. 4.1.

$$M_s = M_{Co} \times \frac{t_{Co}}{t_{Co+Pt}}. \tag{4.1}$$

Form literature [102], M_{Co} is approximately 1.4×10^6 A/m. According to this equation, the estimated M_s is about 3.8×10^5 A/m. However, the measurement from superconducting quantum interference device (SQUID) revealed that M_s is much larger, at about 7.0×10^5 A/m [103]. The larger value extracted from measurements could result from the polarization of the Pt atoms influenced by neighboring Co atoms. We take SQUID measured value for our simulation. Additionally, the assumption is made that M_s is a constant over the whole film.

Magnetic anisotropy K

Magnetic anisotropy value is the most critical parameter in determining the reversal behavior of Co/Pt ML films. In Co/Pt ML films, the anisotropy consists of several terms:

$$K = K_V + \frac{2K_S}{t_{Co}} - \frac{\mu_0}{2}{M_s}^2. \tag{4.2}$$

K_V is the volume anisotropy, K_S stands for the interface anisotropy and $\frac{\mu_0}{2}{M_s}^2$ represents the shape anisotropy term. If $K > 0$, the easy axis of Co/Pt ML is perpendicular to the ML surface; while the easy axis lies in ML plane if $K < 0$.

As anisotropy increases, the Co/Pt ML becomes harder so that the coercivity grows. Take M_s as 7.0×10^5 A/m, the hysteresis curves with different anisotropy values simulated by OOMMF are shown in Fig. 4.3.

Exchange stiffness $\mathbf{A_{exch}}$

Exchange stiffness constant A_{exch} is another key parameter in micromagnetic simulations. Together with anisotropy, it plays the decisive role in determining the shape of hysteresis curve of a single-domain nanomagnet. Fig. 4.4 shows hysteresis

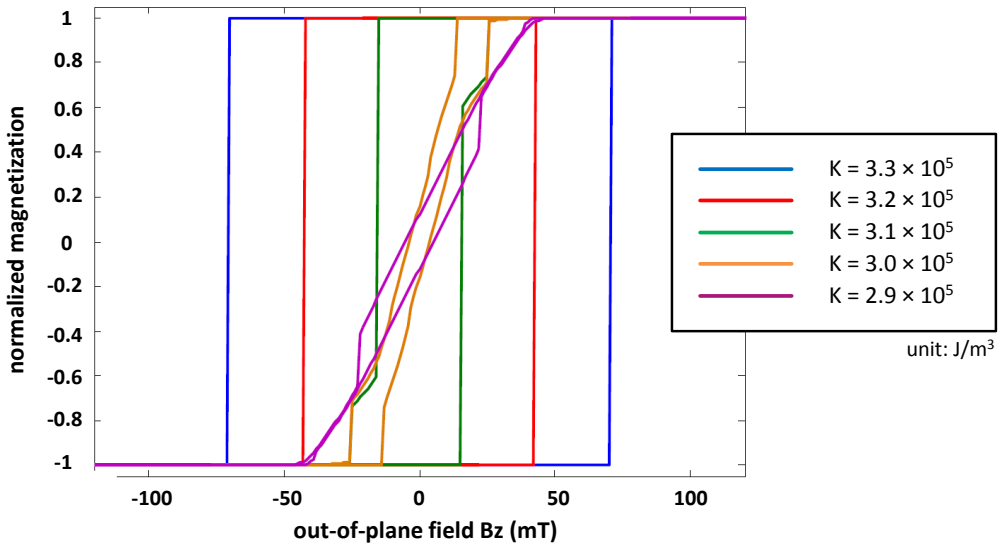

Figure 4.3. Hysteresis curves of a 1 μm $\times$ 1 μm Co/Pt film with different anisotropy values.

curves with different exchange stiffness constants, while M_s and anisotropy K remain unchanged.

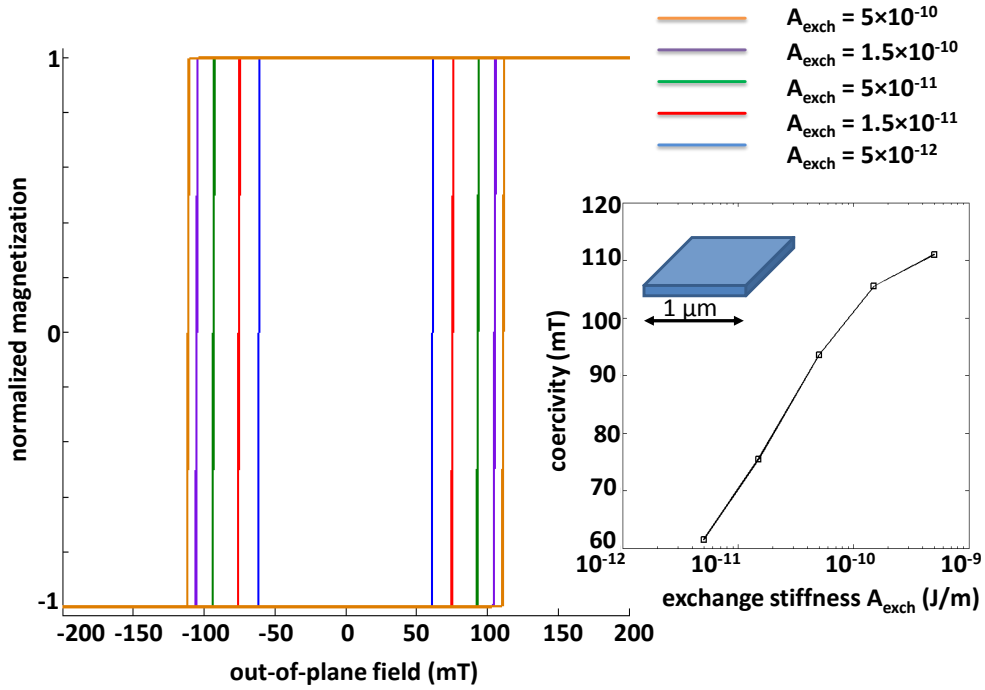

Figure 4.4. Hysteresis curves with different exchange constants. The inset shows coercivity vs. exchange constant.

Nanomagnet size dependency

In principle, the coercivity of large Co/Pt ML films is much smaller than that of small single-domain Co/Pt nanomagnets because the demagnetizing fields in large films contribute more to nucleation process, which subtract one portion of external field required for the reversal of magnetization. In small Co/Pt dots, the exchange forces dominate over the demagnetizing fields, holding the dipoles and hindering the reversal. Therefore, small dots exhibit a large coercivity. The size dependency of reversal behavior is presented in Fig. 4.5. The coercivity reaches a saturation value (minimum) as the film size grows up to a few micrometers.

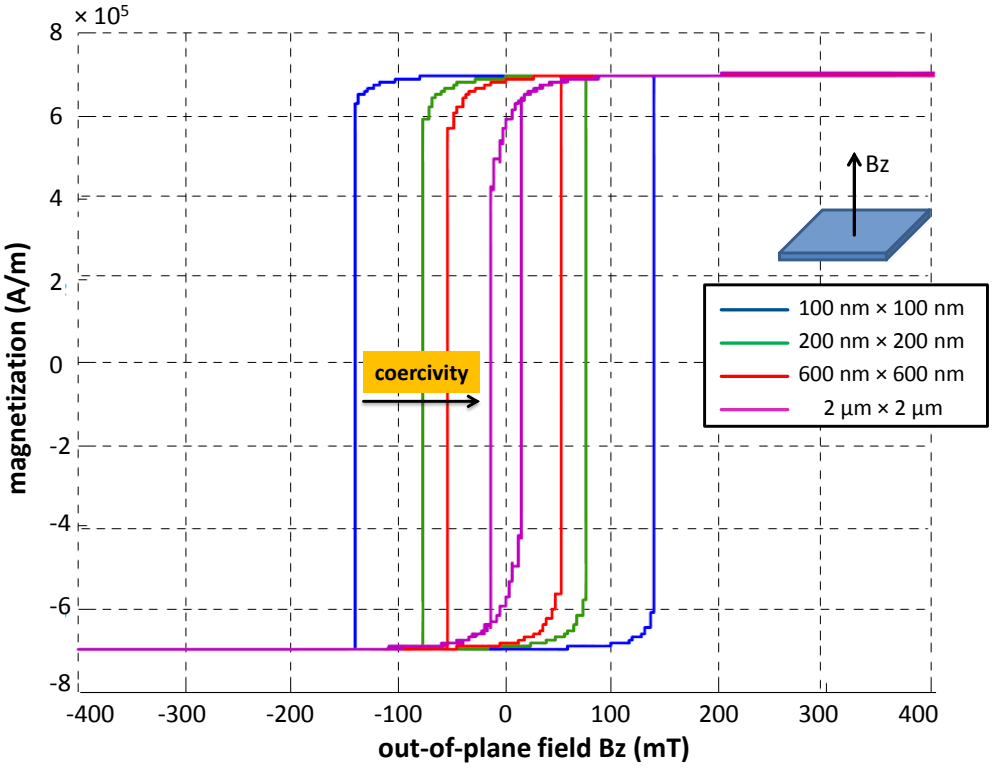

Figure 4.5. The coercivity increases as the dot size scales down.

By tuning the anisotropy and exchange stiffness in OOMMF simulator, the best fitting with experimentally obtained hysteresis can be achieved. Via this fitting method, the optimal values are found for our micromagnetic modeling. For one 5 ML film, we take $M_s = 7.0 \times 10^5$ A/m, $A_{exch} = 1.5 \times 10^{-11}$ J/m and K in the range of $3.08 - 3.2 \times 10^3$ J/m^3. Note that these values are for ideally homogeneous

Co/Pt films. For more details, see [76].

4.3 Calibrated model of Co/Pt multilayer nanomagnets

Here we again consider a five-layer stack of magnetron-sputtered Co/Pt films ($\mathrm{Pt_{5nm}}5 \times [\mathrm{Co_{0.3nm}} + \mathrm{Pt_{0.8nm}}]\,\mathrm{Pt_{4.5nm}}$). By the best fitting with experimental curves, we found that our annealed, unpatterned films are best described by the saturation magnetization of $M_s = 7.0 \times 10^5$ A/m, exchange stiffness of $A_{\mathrm{exch}} = 1.5 \times 10^{-11}$ J/m and an out-of-plane anisotropy of $K = 3.08 - 3.2 \times 10^5$ J/m^3. The value of the exchange constant is the least accurate, but our estimate is consistent with reported data in [104]. There are relatively few measurements for A_{exch} in Co/Pt: the value we used fits well to hysteresis measurements of our thicker films and is lower than a literature value from [105].

All the simulations are under the assumption that the parameters are globally applied to the films. However, the magnetic properties of the films may locally differ from each other. Especially, as described in Chapter 2, FIB irradiation can lead to changes in local irradiated area by means of locally intermixing the thin metallic layers and altering the magnetic properties of the layer stack [59] [106]. It is usually assumed that a high-dose irradiation ($> 10^{15}$ cm^{-2} with 50 keV $\mathrm{Ga^+}$ ions) effectively destroys magnetization and renders the film paramagnetic [107]. This high-dose irradiation process is applied to pattern single-domain dots in a continuous Co/Pt films. This 'cut' is very delicate: the film is not sputtered; only its magnetic properties are altered. Dot size may go all the way down to a few-ten nanometers and these nanomagnets are surrounded by the paramagnetic medium. Clearly, the transition between the magnetic and paramagnetic (non-magnetic) region is not abrupt and magnetic parameters undergo a continuous change in the boundary of non-irradiated and strongly irradiated zones.

In our work, the Micrion 9500 EX FIB is in use. A detailed description of this equipment is given in [77]. At a acceleration voltage of $V_{acc} = 50$ kV, the FIB beam diameter reads at the scale of 5 nm. However, this value would be

broadened when interacting with metal/insulator films. The FIB patterning in Co/Pt films with focused Ga^+ are thoroughly described in [106] [108] [109]. For our specific multilayer stacks, SRIM/TRIM (stopping and range of ions in matter/transmission and range of ions in matter) simulations [110] [111] are carried out to study the ion penetrating depth and beam diameter. The simulation result from [77] suggests for metallic Co/Pt films, the transversed depth of $10-30$ nm and the beam diameter in the range of $20-40$ nm. SRIM simulations also estimate the extent of the transition region, illustrated in Fig. 4.6 a). In this example a line cut is formed by placing dwelling points 10 nm apart. Each dwelling point receives 100 ions – this corresponds to dose of 10^{14} cm^{-2} or 1.6 nC/cm line dose. Along the y direction (the cut) the dwelling points overlap to a narrow non-ferromagnetic line. Along the x axis an approximately 15 nm wide partially irradiated region is formed. The local dose ($D(x)$) changes according to a Gaussian distribution.

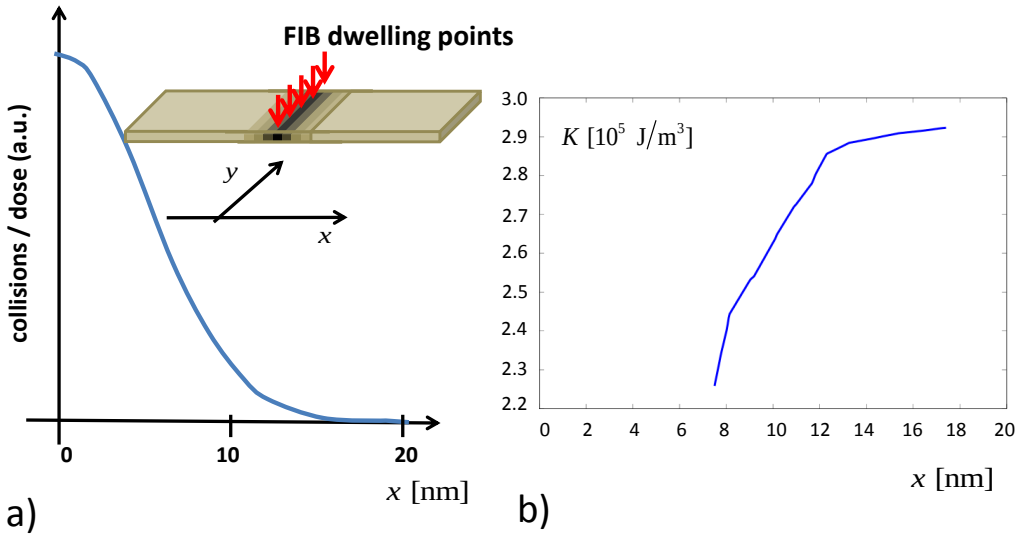

Figure 4.6. Part a) illustrates the dimensions of the irradiated region at the side of a nanomagnet and the distribution of ion collisions along the boundary. Panel b) demonstrates how we calculated the anisotropy profile from the irradiation profile based on experimental data of a large film. The experimental curves are based on [107].

Based on the discussion above, it is clear that the FIB irradiation can't be entirely focused. Within the beam diameter, the dose of irradiation ions appears

a Gaussian-like distribution, i.e. if ideally we expect to separate two dots with a distance of 10 nm, then a number of ions disperse from the focused center and are shoot on the edge of the dots, as sketched in Fig. 4.7 (b). Compared to the idea cut shown in Fig. 4.7 (a), a side effect occurs. Now one question is addressed: will this side-effect influence the characteristics of patterned Co/Pt dots?

To answer this question, we look into how the magnetic properties of the film change in the vicinity of the cut, with published data of irradiated films [106] [107] and from our recent measurements [75]. These works characterize the effect of homogeneous Ga^+ ion irradiation on the saturation magnetization and the coercive field (anisotropy) of a large-area film. We assume that the physical processes caused by ion irradiation act similarly on the few-ten nanometer scale than on large-area films. The spatial dependence of the anisotropy ($K(x)$) then can be determined from the simulated distribution of ion collisions.

First, we find the relationship between coercivity B_c and the $D(x)$ dose distribution [75]. Then we use micromagnetic simulations to find the relationship between the coercivity and the anisotropy of the film ($B_c(K)$) [75]. The $K(x)$ curve of Fig. 4.6 is then straightforwardly determined from the spatial dependence of the irradiation ($D(x)$, as calculated from SRIM simulations) and from the $B_c(D(x))$ and $B_c(K(x))$ functions. For small K values ($K < 2.3 \times 10^5$ J/m^3), the film turns in-plane and this procedure cannot be followed. Based on this map, FIB cutting induced lower-anisotropy edges is demonstrated in Fig. 4.7 (c).

Simulation results also confirmed that it is sufficient to consider low-anisotropy 'rings' at the perimeter of the dot while leaving M_s and A_{exch} constant in the ferromagnetic region. The reversal process remains almost the same in this simplified ring-model and we employ this simplification in most of the simulations.

To implement point-wise changing magnetic parameters in OOMMF, we developed a Matlab-script based pre-processor package. It prepares an input file, giving the K, A_{exch}, M_s parameters at each point of the simulation lattice. The simulation is then performed with the three-dimension version of OOMMF (Oxsii)

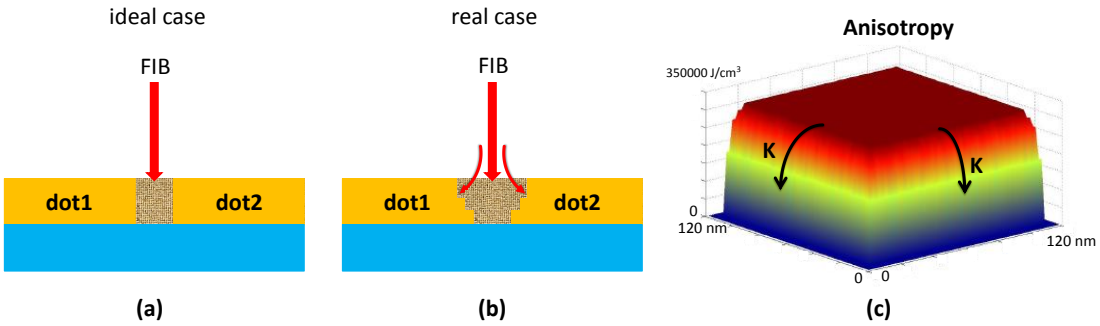

Figure 4.7. (a) ideal case of FIB cutting. (b) real case: irradiation-induced side effect. (c) the anisotropy of a single-domain dot: the K value is smaller at the edges.

[94]. The simulations ignore temperature-related effects. Despite the extensive literature on Co/Pt multilayers, we could locate only one paper [112], which used a similar simulation approach to FIB-defined dots in perpendicular media.

4.4 Reversal behavior of a stand-alone nanomagnet

Co/Pt single-domain nanomagnets switch by a nucleation event followed by domain wall propagation. The location and characteristics of the nucleation site(s) play a decisive role in the reversal [112]. FIB patterning brings down the anisotropy at the edges of Co/Pt dots. Theoretically, these low-anisotropy boundaries are the most likely place for a nucleation event because it is easier to switch the magnetic dipoles with lower anisotropy.

As a verification, we modeled an FIB-cut 200 nm $\times$ 200 nm nanomagnet with soft edges. Along the boundaries of the dot, K linearly decreases from $K_{\max} = 3.2 \times 10^5$ J/m to $K = 0$ in a 30 nm wide region. The side irradiation is taken into account by changing the anisotropy parameter in the OOMMF simulation. The reversal behavior is illustrated in Fig. 4.8 a), where the snapshots from micromagnetic simulations reveal that in FIB-defined dots, nucleation center starts at the soft edges (edge nucleation). For comparison, Fig. 4.8 b) shows the simulation of the same dot but without taking the low-anisotropy boundaries

into consideration (here K is set homogeneously and goes abruptly to zero at the edges). In this case, reversal starts from the center of the dot, where the demagnetizing field is the largest. Now it is clear that due to the irradiation-induced side effect, the reversal starts at a lower field and at completely different places.

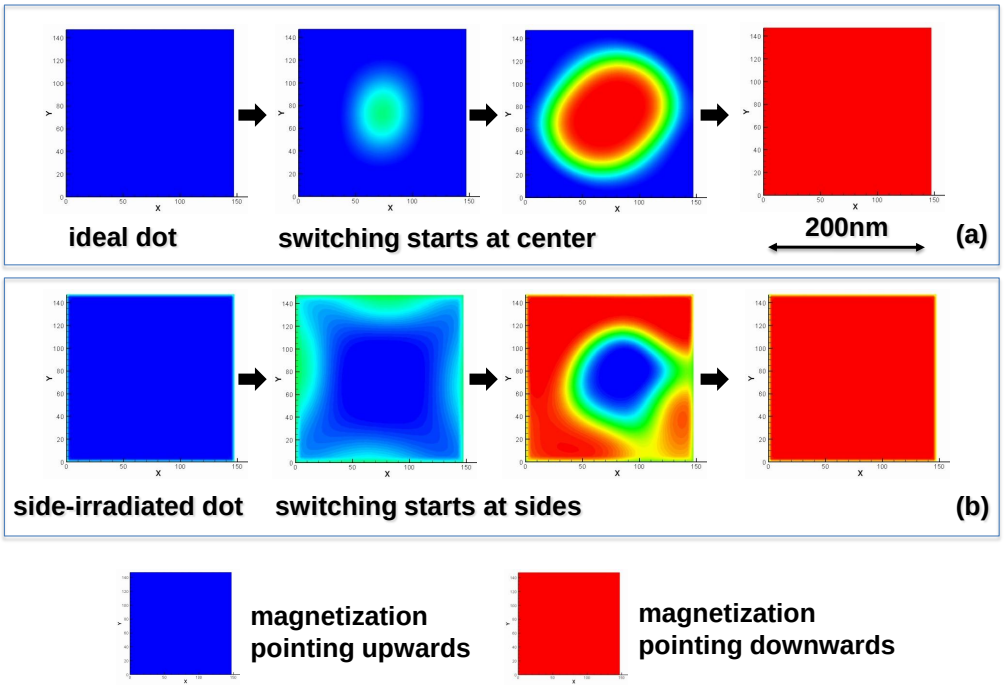

Figure 4.8. Snapshots of magnetization switching for a 200 nm size dot a) irradiation from all sides b) without side irradiation. The irradiated zones were modeled as 30 nm wide low-anisotropy regions, where K linearly decreases from $K_{\max} = 3.2 \times 10^5$ J/m^3 to zero. Non-irradiated zones are all treated with $K_{\max} = 3.2 \cdot 10^5$ J/m^3 anisotropy.

In order to experimentally support this model, we used Extraordinary Hall Effect (EHE) measurements to characterize the switching of irradiated Co/Pt dots. A Hall sensor in split-current geometry was fabricated using FIB lithography and hysteresis curves were recorded for both the as-grown film and for an 800 nm size rectangular dot, cut out by FIB. For a detailed description of the measurement setup, see [75]. The experimental curves are shown in Fig. 4.9 a).

Comparing the experimentally observed switching behavior of a large-area film and the submicrometer-sized dot, one can observe that the film switches more

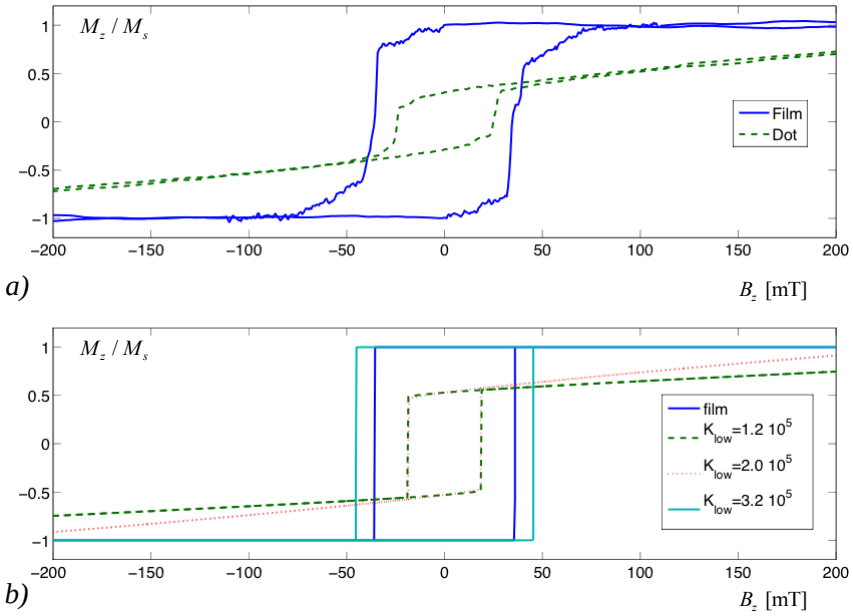

Figure 4.9. Experimental a) and calculated b) hysteresis curves for an as-grown Co/Pt film and dot made out of it. For the dot simulations we considered a 50 nm wide low-anisotropy region at the edges of the dot, which is consistent with estimations based on the sensor fabrication technology [77].

abruptly and at a higher field than the dot. Both effects are closely reproduced by assuming a 50 nm wide, low-anisotropy ring around the dot: the more gradual switching is due to the low-K regions and the lower switching field caused by the easier nucleation starting in these regions. Without taking into account the low-anisotropy ring the smaller dot would experience lower demagnetizing fields (shape anisotropy) and would switch only at higher fields. Partial irradiation also reduces the dependence of the switching field on dot size.

The calculated and measured hysteresis curves in 4.9 b) are similar - except that simulations predict a more abrupt switching. This discrepancy is most likely due to pinning sites in the real film, which were not taken into account in the simulations.

These observations are in close agreement with experimental and simulation findings of [112], although their work investigates the Co/Pd material system.

4.5 Reversal behavior of field-coupled nanomagnets

The reversal behavior of the two field-coupled dots differs from one stand-alone dot due to the existence of coupling. Assuming two Co/Pt dots stand close to each other, the stray field of one dot may help or hinder the switching of the other one, depending on the current magnetization states. In simulations, the coupling strength can be measured by hysteresis curves of two field-coupled dots. As shown in Fig. 4.10, initially two dots with a gap of 10 nm are magnetized to the same direction. One dot is slightly larger than the other at size so that this dot has a smaller coercivity and flips over first when the external field is large enough. The smaller dot with a larger coercivity hold its magnetization and behaves as a helper as the larger dot switches since they have parallel magnetization. As soon as the larger dot is switched, the role of the coupling field changes: the stray field of switched dot prohibits the switching of the non-switched dot. As a result, a further increase of the external field is needed in order to overcome the coupling barrier. We define the coupling strength as one half of the difference between the two switching fields. The coupling strength strongly rests on the material properties (thickness, composition, FIB irradiation $\cdots$), the size of the dots and the separation width.

The coupling strength of two 200 nm $\times$ 200 nm dots as a function of separation width is plot in Fig. 4.11, where we could see with a separation width larger than 150 nm, two dots almost experience no coupling. We take this as a conclusion for the later simulations that strong coupling only exists between the nearest neighboring dots. The coupling from other dots are ignorable (the distance is too faraway).

4.6 Single-domain state and metastable states in Co/Pt multilayer films

All the nanomagnets in NML devices are expected to be in single-domain state, standing for either logic 1 or logic 0. In in-plane NML, due to the shape anisotropy

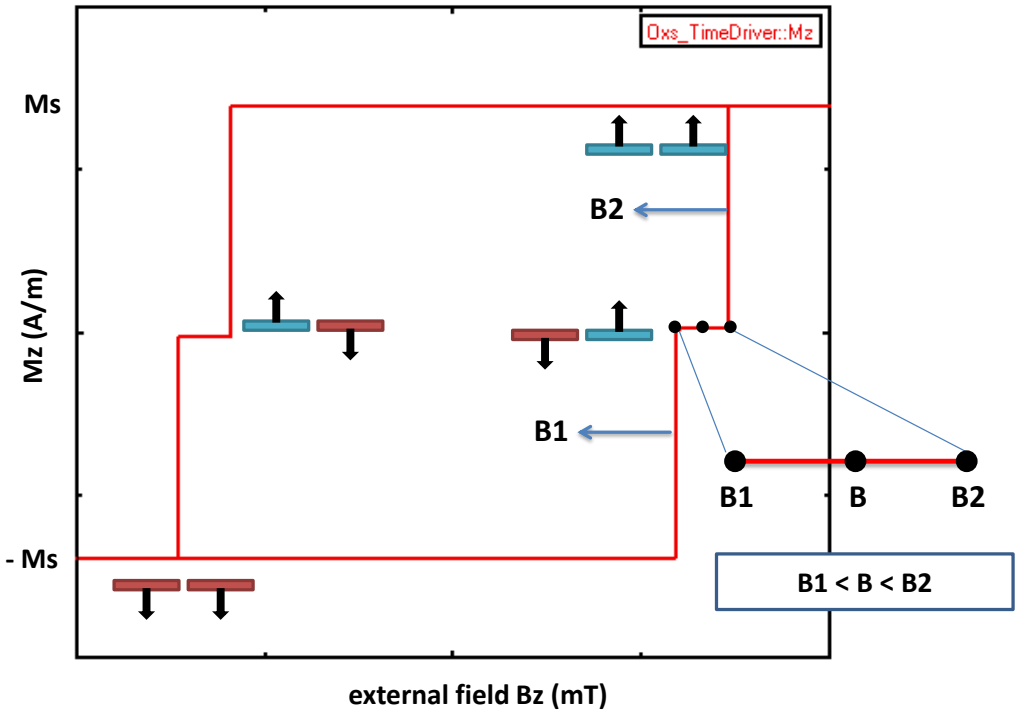

Figure 4.10. The hysteresis curve of two field-coupled dots. The coupling results in a shift in the hysteresis, and the coupling strength decides the shift width in the hysteresis curve.

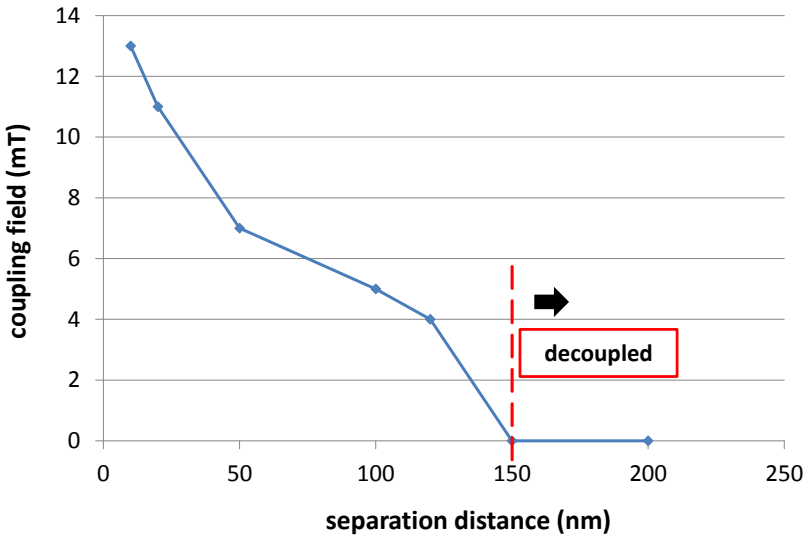

Figure 4.11. The coupling strength as a function of the separation width for a 200 nm $\times$ 200 nm dot.

of elongated Permalloy dots, the magnetization prefer to align along the longer axis (easy axis). Two logic states have equal possibility (50%) and are distinguished from the two opposite directions of magnetization. The size of the Permalloy dots should be sufficiently small so as to avoid falling to the metastable states. The most often observed metastable state appearing vortex-like magnetization pattern is shown in Fig. 4.12 (b). However, there is no such a well-defined value, with which one can hundred-percent tell if the nanomagnet is in single-domain state or multiple-domain state. There is an intermediate range of dot size, in which dots are possible to relax to either single-domain or multiple-domain states, depending on the initial magnetization state. We analyze the statistics of the evolution of individual Permalloy dots, which relax to the final state from an initial random magnetization state by a great number of OOMMF simulation, where the dot size is the variable, but the length-width ratio sticks to a constant 1.5. The result is given in Fig. 4.13.

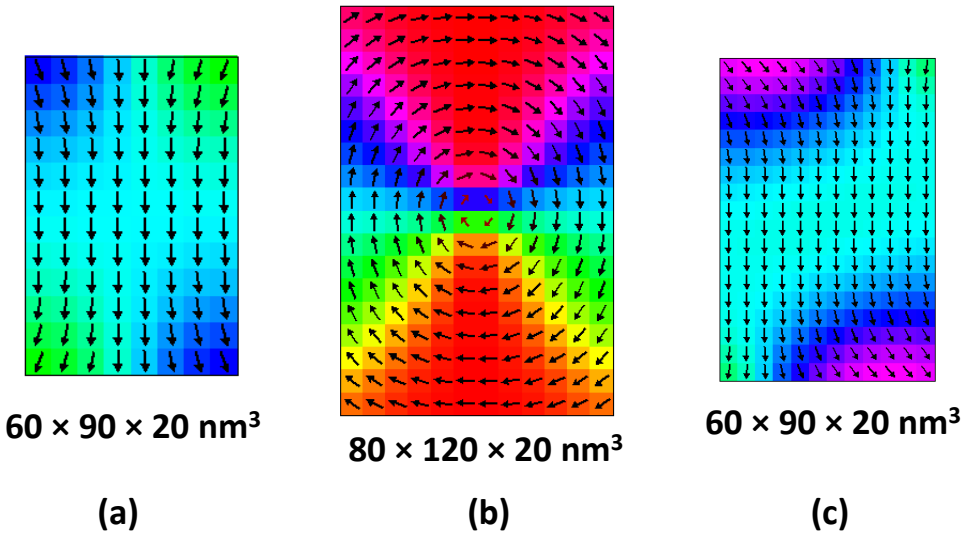

Figure 4.12. (a) Single-domain state, (b) multiple-domain state (vortex pattern) and (c) one of the end-domain states (see Appendix A).

Most recent research shows, even dots with a size in sub-100nm range usually exhibit one of the end-domain states due to the imperfection of dot shape from fabrication (Fig. 4.12 (c)) [113]. However, with a good alignment of the dots and

the external filed, we could assume the end-domain states only originate from the shape variations. Since the shape variation is random, the magnetization vector of a large number of dots along the hard axis are canceled. Hence, dots in end-domain states can be briefly considered as in single-domain state.

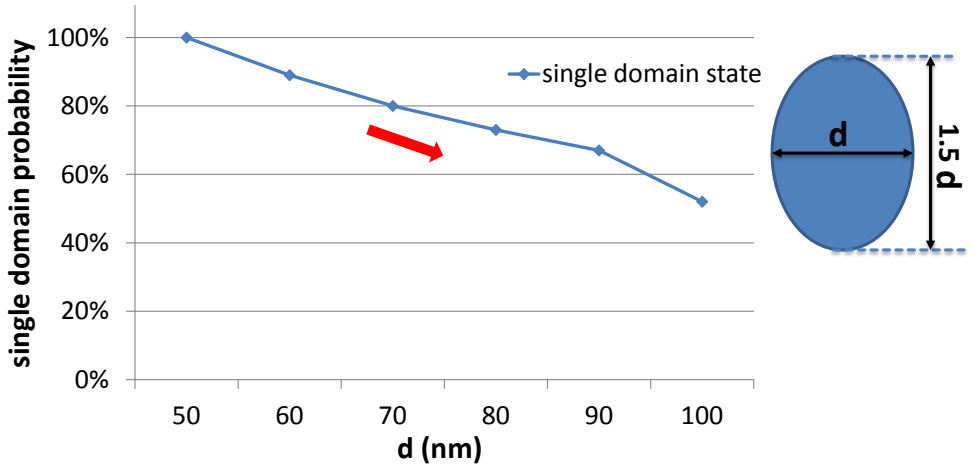

Figure 4.13. The magnetization of one Permalloy dot with ellipsoid shape is initialized with random spins orientations. The possibility of relaxing to the single-domain state increases as the dot size reduces. The thickness was chosen as 20 nm in the simulations.

Similar to Permalloy dots, Co/Pt based dots also need to be small enough to be in the single-domain range. However, as a single-domain state turns to multiple-domain state, a small part of magnetization first reverses and this is the nucleation event of switching. After that, the domain wall created from nucleation process propagates until a stable multiple-domain state is formed. Instead of having a vortex-like pattern of multiple-domains in Permalloy dots, the Co/Pt dots usually split to a 'half up - half down' pattern (though the domain wall doesn't have to lay exactly in the middle), meaning one part with magnetization pointing upwards and that of the other part downwards, as shown in Fig. 4.14.

As talked over in Chapter 3, the single-domain size means a transitionary interval between the upper and low limits. To our knowledge, there is no such a clear quantitative definition on this critical size. Here we introduce our method

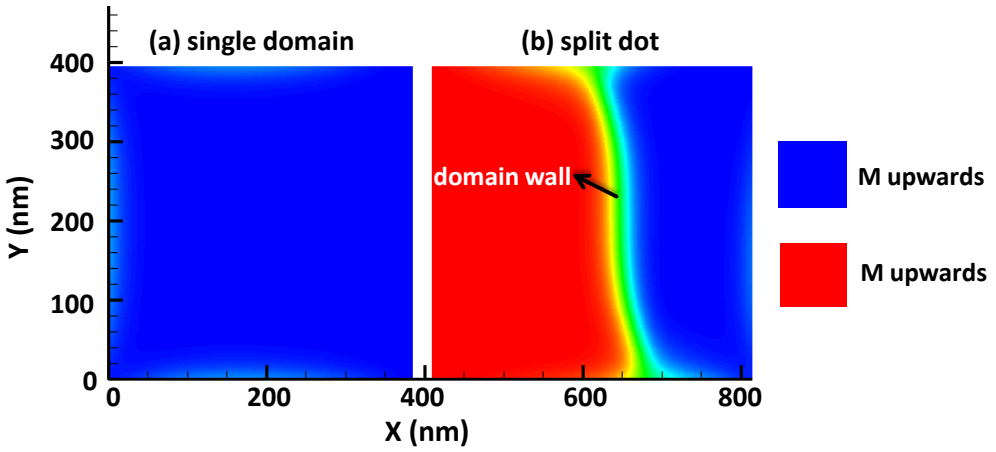

Figure 4.14. The single domain state (a) and split domains state (b) of 5 ML Co/Pt dots with a size of 400 nm × 400 nm.

to define the domain size for Co/Pt nanomagnets by means of energy calculations with OOMMF. More specifically, we define the single-domain size in such a way that we calculate the total energy of Co/Pt nanomagnets in single-domain state E_1 and in split multiple-domain state (split from the middle) E_2 respectively. Then a comparison between E_1 and E_2 is made. At a certain size, the total energy of the two states equal to each other. This equilibrium indicates the quantitative value of single-domain size. If $E_1 > E_2$, the split state is energetically preferred since it locates at a lower energy level. While below the single-domain size, $E_1 < E_2$ so that the single-domain state remains.

Single-domain size is dependent on the ML properties. By fixing the anisotropy to 3.2×10^5 J/m^3 and exchange stiffness to 1.5×10^{-11} J/m, the comparison is made on 5 ML Co/Pt dots with different sizes. The data are listed in Table 4.1. There the single-domain size turns out to be 600×600 nm^2 as E_1 equals to E_2 (in red).

Due to the intentional FIB irradiation treatment and unintentional fabrication variations, the anisotropy values of Co/Pt dots differ from each other. Assuming the anisotropy is homogeneous over the dots, with the same method we analyzed how the single-domain size relies on the anisotropy. The result is plot in Fig.

TABLE 4.1. ENERGY COMPARISON BETWEEN SINGLE-DOMAIN STATE E_1 AND SPLIT STATE E_2

dot size (nm)	E_1 (J)	E_2 (J)
50×50	3.5999×10^{-18}	4.7931×10^{-18}
100×100	1.5961×10^{-17}	1.7631×10^{-17}
150×150	3.7374×10^{-17}	3.9230×10^{-17}
200×200	6.7903×10^{-17}	6.9809×10^{-17}
250×250	1.0758×10^{-16}	1.0944×10^{-16}
300×300	1.5642×10^{-16}	1.5816×10^{-16}
400×400	2.8164×10^{-16}	2.8297×10^{-16}
500×500	4.4363×10^{-16}	4.4436×10^{-16}
600×600	6.4243×10^{-16}	6.4243×10^{-16}
700×700	8.7805×10^{-16}	8.7719×10^{-16}

4.15. The simulations verified that the single-domain size arises as the anisotropy increases, which makes sense because the reversal of dipoles is more different in magnetically harder films.

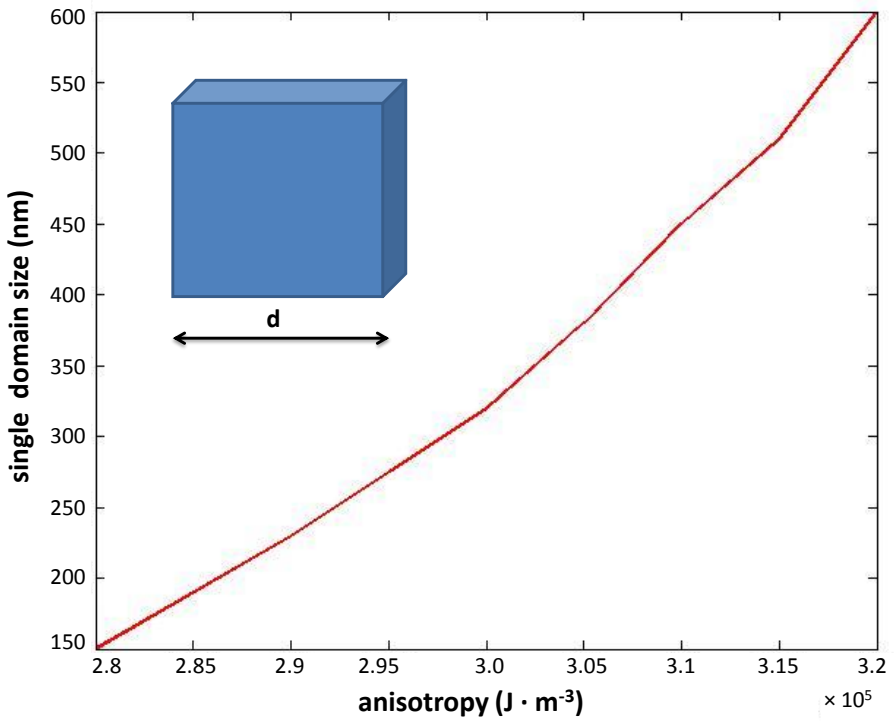

Figure 4.15. The single domain size (d) is strongly dependent on the local anisotropy value of Co/Pt material.

As the size of the Co/Pt ML increases from 'dot scale' to 'film scale', the

Co/Pt films tend to appear in more complex multiple-domain patterns. This way mentioned before to detect single-domain size is not valid any more. However, it is possible to see the trend from the formed patterns.

Sticking to the same layer composition, we implemented simulations to explore the relationship between the total film thickness and the single-domain size. The simulations were carried out as follows: n ML Co/Pt square films with a length of a few μm was demagnetized with an easy-axis demagnetizing external field. After demagnetization, the Co/Pt films appeared multiple-domain domains, for instance, the pattern simulated in Fig 4.16 (a). The average width of the domain stripes reveals the single-domain size. The characteristics are depicted in Fig 4.16 (b). Note that the single-domain size in Fig. 4.16 (b) actually stands for the average stripe width, which is theoretically smaller than the critical domain-size we defined earlier by means of calculating the total energy. However, the trend from the curve agrees very well with the experimental result in [99], suggesting the proper layer number to use in order to achieve larger single-size and prevent the dots from splitting.

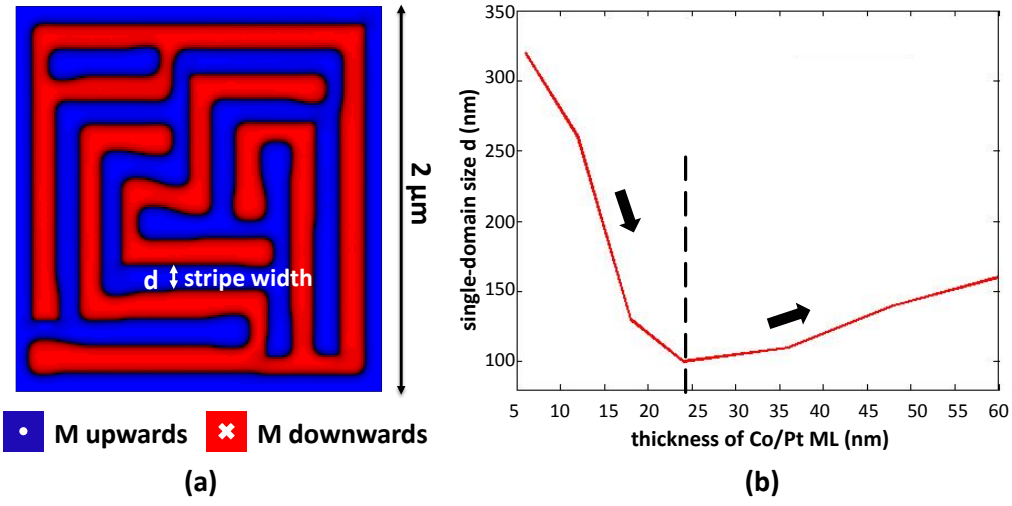

Figure 4.16. (a) the multiple-domain pattern of a 15 ML Co/Pt film after demagnetizing: the average width of domain stripes is about 130 nm. (b) Single-domain size (average width of domain stripes) as a function of the thickness of Co/Pt ML films.

4.7 Errors in field-coupled Co/Pt multilayer based Nanomagnet Logic

The operation of NML devices is based on magnetic ordering. Frustrations of ordering will result in computing errors. In this section, we present the most often observed errors of Co/Pt based NML in our experimental and simulation study and explore the sources of these errors.

In experiments, Co/Pt ML nanomagnets possessing large perpendicular anisotropy exhibit strong dipolar coupling [71]. Nanomagnetic chains made up with a small number of Co/Pt multilayer dots have been proven working reliably after demagnetization process [75]. However, it is noticed that errors often occur in Co/Pt based NML made from a relatively larger number of dots. Co/Pt multilayer dots pointing to the wrong direction or splitting into multiple-domains are the two types of most frequently identified errors. Here we analyze the mechanisms of these error formations based on simulations and provide strategies to avoid them. Our proposed method to achieve error-free computing with partially irradiated nanomagnets will be described in detail in Chapter 5.

4.7.1 Frustrations of ordering in nanomagnet arrays

As shown in Fig. 4.17, an easy-axis demagnetizing field is applied to drive all the nanodots to the 'up-down-up-down' computational ground state and achieve anti-parallel ordering. However, MFM image shows some neighboring dots with parallel-aligned magnetizations appear in the chains after demagnetization. Consequently, the magnetic information is not transmitted correctly from the input (leftmost) dot to the output (rightmost) dot.

Due to inevitable process variations and thermal fluctuations, the switching properties of dots may differ from each other. A dot with lower switching field decouple earlier from the demagnetizing field and end up in a random (possibly wrong) state, which is not decided by the couplings. Susceptibility to errors is further increased by reciprocal (bidirectional) signal propagation due to symmetrical coupling. Symmetrical coupling means one dot in the chain experiences the same

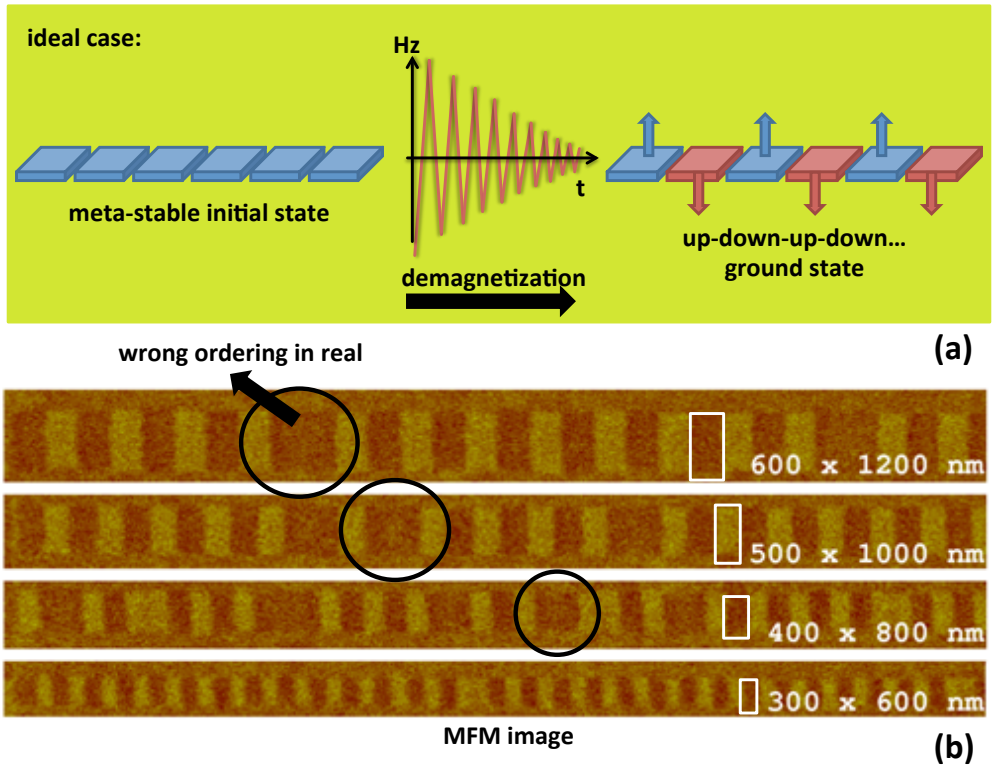

Figure 4.17. (a) Model of idea alignment after demagnetization. (b) Ordering problems observed in our experiments [77].

amount of coupling strength from the neighboring dots at both sides, as illustrated in Fig. 4.18 (a), where we assume dot (i) and dot (iii) have initially anti-parallel magnetization. Due to symmetrical coupling from these two dots, the middle dot (ii) could easily switch to the wrong logic state. Since the signal propagation with symmetrical coupling is not uni-directional, a nucleated error cannot easily leave the structure.

Properly ordering the dots in majority gates becomes even more challenging. Errors most probably happen to the middle dot in majority gates. Fig. 4.18 (b) reflects the problem because of the back-influence from the output dot to the middle one. There the coupling strength from each input equals to that from the output dot. Assuming that one of the three input dots and the output dot are in the same logic state, while the rest two inputs dots have the opposite, the coupling to the middle dot are canceled so that it is 50% chance that the middle

dot switches to the wrong state. Though the coupling strength from neighbors can be tuned by changing the dot size, errors are ineluctable in large-scale devices.

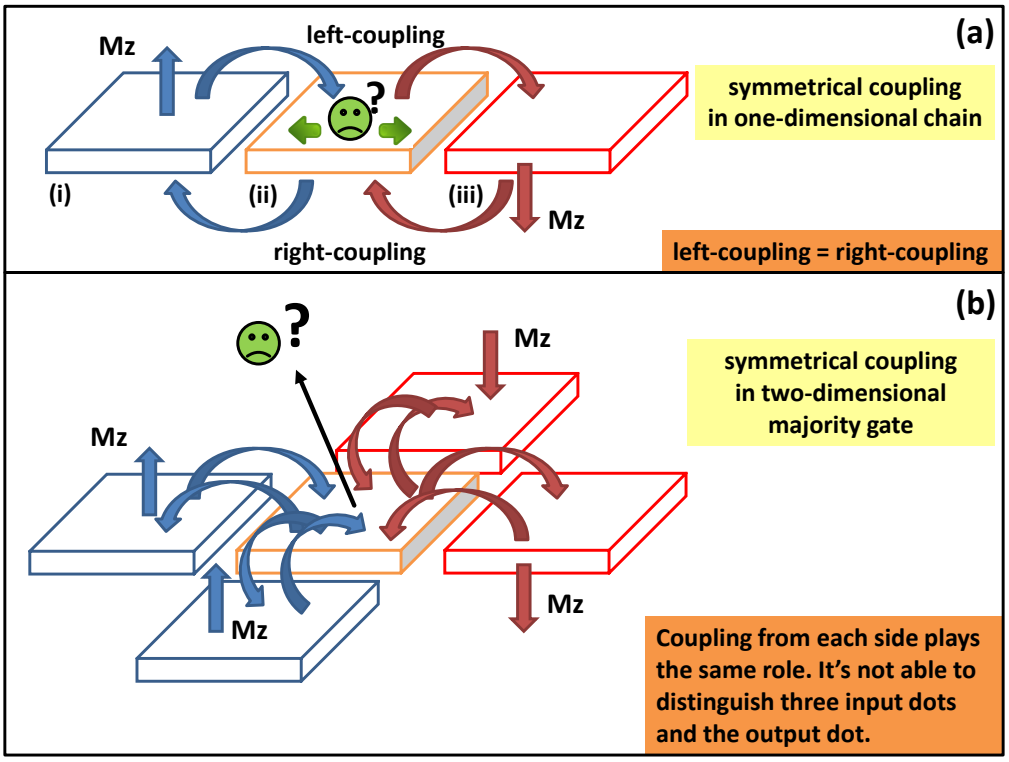

Figure 4.18. Possible errors due to symmetrical coupling in (a) an one-dimensional nanomagnetic chain and (b) a two-dimensional majority gate.

Note the ordering error not only exists in Co/Pt based oNML, but also in iNML, where Permalloy dots may also relax to the wrong states, even when locally clocked. Symmetrical coupling is the main cause that leads to the ordering frustrations. In other words, the essential way to clear up this kind of errors is to get rid of, or at least weaken as much as possible, the unwelcome back-propagation in NML structures.

4.7.2 Splitting to multiple domains

Besides the frustration of ordering in single-domain nanomagnets, split nanomagnets are another issue needed to consider – split dots represent no logic value in NML and have lower stray fields. They are only weakly coupled to their neighbors and interrupt the signal flow. An MFM image of demagnetized coupled dots

is shown in Fig. 4.19, where several split ones are observed. As it is already discussed, the single-domain size of Co/Pt dots is strongly dependent on magnetic properties and dipolar coupling from the surrounding neighbors helps with stabilizing the multiple-domain states [99]. For this reason, dot size well above the single-domain size should be avoided in NML applications.

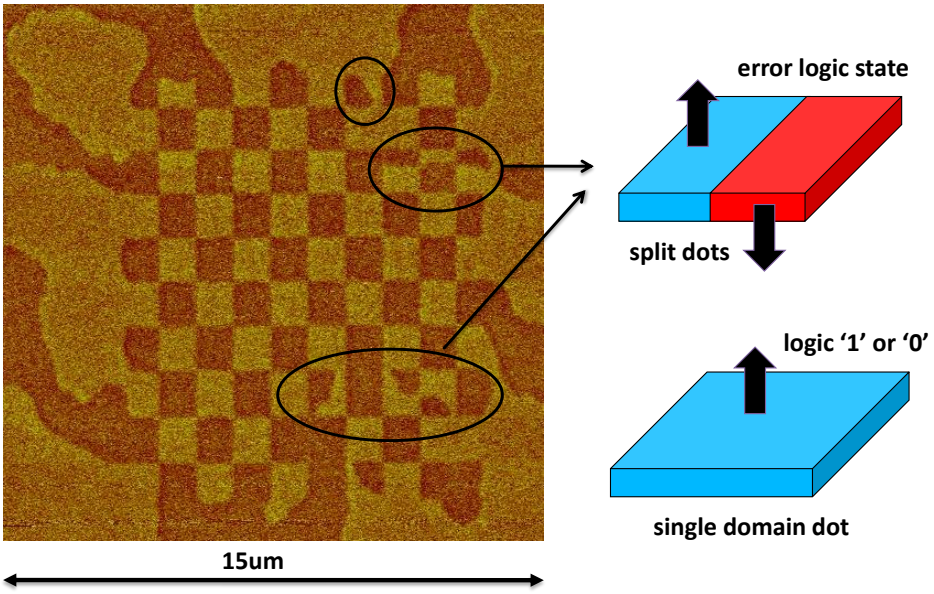

Figure 4.19. MFM image showing several split dots in our experiment [77].

However, experimental and simulation results showed that some small Co/Pt dots split, even if the single-domain state is energetic ground state. Pinning sites from fabrication process may explain metastable states in certain cases. In addition, our simulations show that domain walls can get stuck even in small dots and yield to long-living metastable states.

Using OOMMF, we investigated the splitting characteristics of Co/Pt dots. The sketch of a domain wall is demonstrated in Fig. 4.20 (a). We performed a number of simulations by initially placing a domain wall at different positions of a 5 ML Co/Pt dot and calculate the total energy. The length/width ratio of the dots is 3 : 1. Simulation result shows that without an external magnetic field the dot either splits in the center or becomes single-domain, depending on where

the domain wall is initially located. The formation of a domain wall raises the anisotropy energy and exchange energy, but lowers the demagnetizing energy. If the dot size is below single-domain size, splitting in the center is the metastable state because then demagnetizing energy reaches a local minimum. As the domain wall position moves from the center to one border, demagnetizing energy starts to increase, which is the main contribution of the energy barrier. An illustration is depicted in Fig. 4.20 (b), where the increasing demagnetizing energy of a 150 nm $\times$ 50 nm dot is calculated. If we estimate the domain wall energy remains a constant before it moves out from the boundary, then the barrier is arising from increasing demagnetizing energy, as given in the sketch of Fig. 4.20 (c). The split dot has to overcome this energy barrier to finally turn to single-domain. In Fig. 4.20 (d), the landscape of barrier height is calculated for dots with dot widths varying from 50 nm to 100 nm. The minimum barrier height is larger than 80 k_BT, indicating the reason that the metastable state can last for a long time at room temperature. Using the extension module of OOMMF [98], we verified with these barrier heights, the splitting metastable states are robust to thermal noise up to 300 Kelvin. The minimal external field sufficient to overcome the energy barrier of a 150 nm $\times$ 50 nm dot is calculated to be 16.3 mT, which gives a hint about minimal energy consumption to get rid of the split states.

Taking temperature fluctuations into account, more simulations were implemented on smaller square dots. In these simulations, again initially we placed a domain wall in the dot. Fig. 4.21 presents the simulation result. Dots smaller than 50 nm $\times$ 50 nm (Fig. 4.21 (a)) turns to the single-domain state only within few nanoseconds. As the dot size grows, it takes longer to drive out the domain wall, as shown in (b) and (c). As soon as the barrier height becomes large enough, metastable state tends to remain (Fig. 4.21 (d)). Thermal fluctuations are not able to remove the domain wall. We conclude that really small dots hardly split since the barrier between single-domain state and split state is very low. Metastable states can be easily eliminated by thermal noise. Hence, the single-domain state

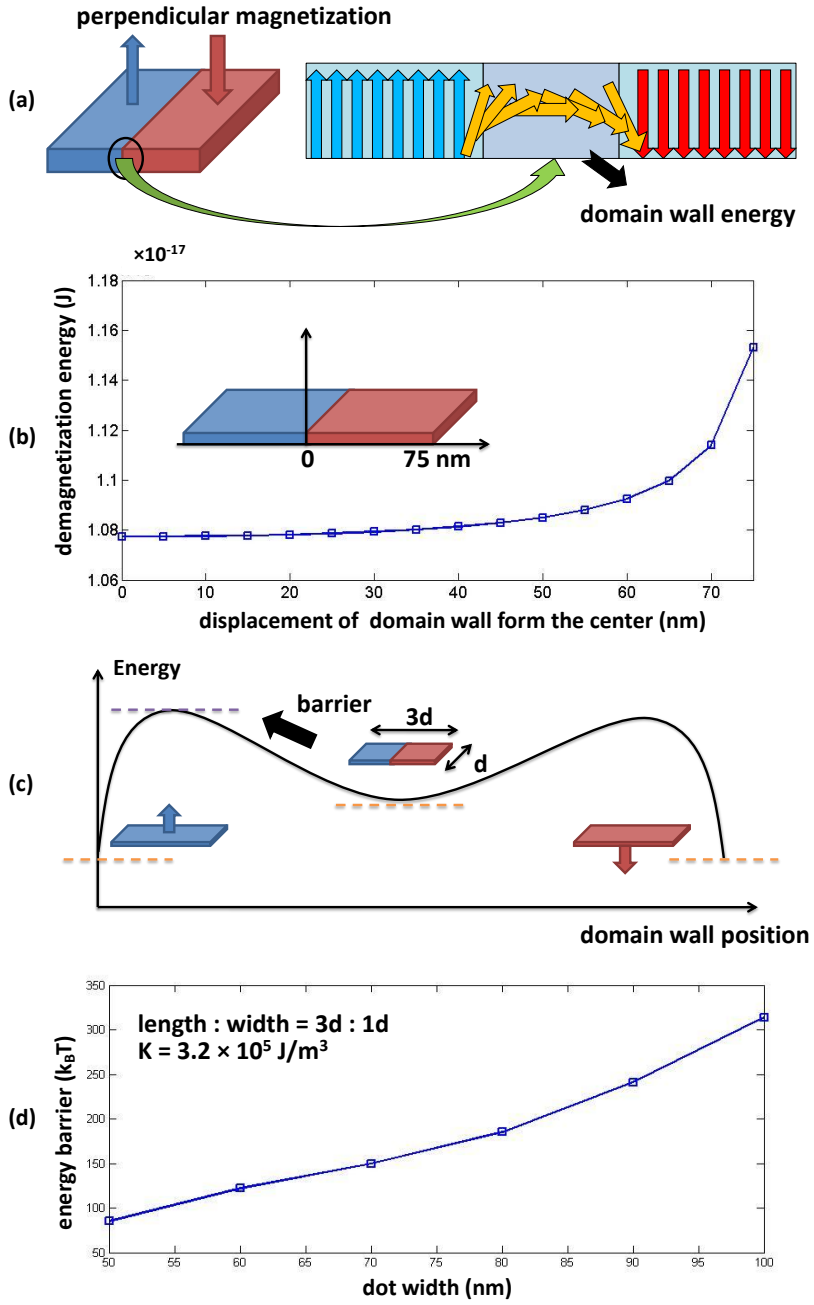

Figure 4.20. (a) A sketch of a domain wall in a Co/Pt dot. (b) Demagnetizing energy increases as the domain wall movers from the center part to the borders. (c) Energy landscape of Co/Pt dot from the split state to the single domain state. (d) Energy barrier as a function of the dot size.

is quite stable. As the dot size increases, the possibility to have error states increases. From our simulation, the critical square dot size turns out to be 80 nm × 80 nm. Once dots with sizes larger than this critical value reach a metastable state, it is necessary to apply an external field in order to remove the domain wall,

which become an additional precondition for Co/Pt based NML.

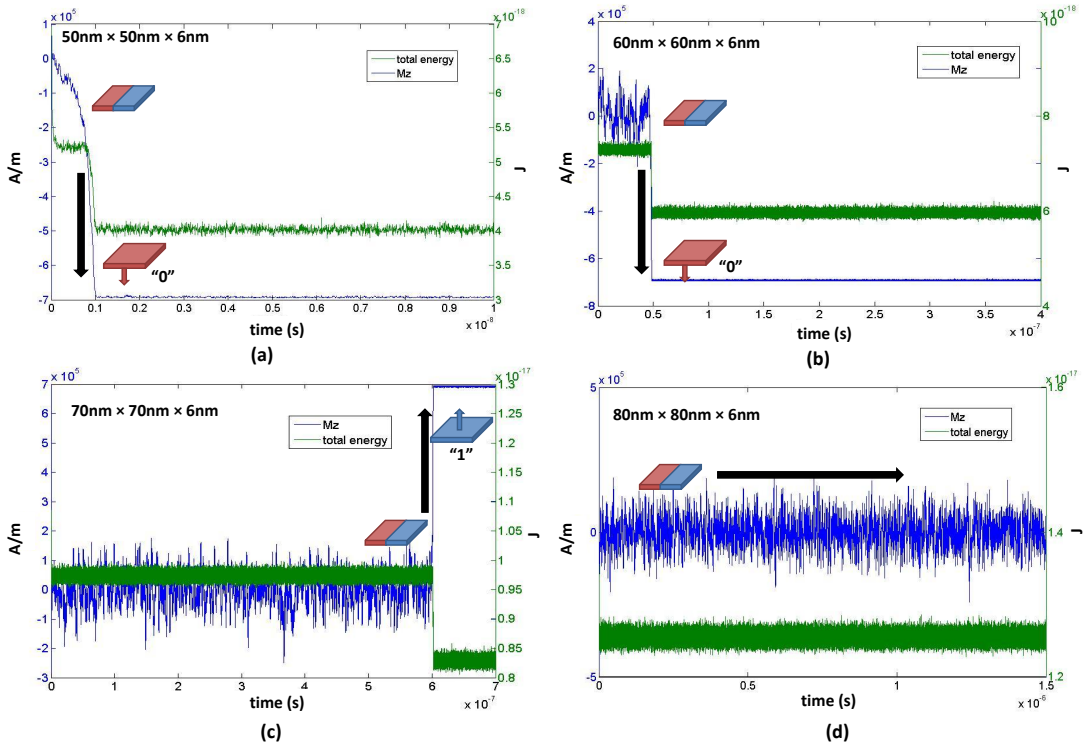

Figure 4.21. Micromagnetic simulation taking thermal fluctuations into account: evolution of domain walls of square dots with different sizes. The domain wall becomes more robust against temperature as the dot size increases.

Based on all the discussion above, we can summarize the following guidelines to reduce the error rate in NML:

- Co/Pt multilayer films with high anisotropy exhibit a larger single-domain size, which is favorable for NML and results in a lower splitting rate. Other approaches which are able to increase the single-domain size of Co/Pt multilayer film are also recommended, e.g. adjusting the number of Co/Pt bilayer repetitions and the deposition conditions.

- Smaller dots are more immune to splitting into multiple domains, which are also advantageous for increasing the device density of NML.

- An external field will significantly decrease the splitting rate with the prerequisite given that the external field is strong enough to drive the domain

wall out of the dots.

An apparent trade-off is that smaller dots with high anisotropy require a higher switching field. In the next chapter, I will propose our approach to solve this problem, by which the power consumption can be reduced to a satisfying level.

CHAPTER 5

NANOMAGNET LOGIC WITH PARTIALLY IRRADIATED CO/PT NANOMAGNETS

The operation of Nanomagnet Logic (NML) devices relies on the magnetic ordering of single-domain nanomagnets. This ordering is initiated and controlled by an external clocking field. Frustration of ordering translates to errors in the magnetic computation. It is well known from physics that a large Ising-like system of coupled magnets (dipoles) will never order perfectly [114]. Thermal fluctuations, variations in magnet shape and dynamic effects may all lead to problematic frustrations. This limits the number of the nanomagnets that can order simultaneously by a homogeneous clocking signal. To make NML operation reliable and scalable to non-trivial circuit sizes, localized clocking fields must be used. Localized clocking fields affect only a limited number of interacting magnets at the same time [42] [115] and one block of magnets orders after another. This clocking scheme comes at a price: it significantly complicates device construction and on-chip generation of localized magnetic fields is inefficient, which requires relatively large currents and yields to dissipation via Joule heating in the clocking apparatus.

In Chapter 4, the point-wise computational model of FIB patterned Co/Pt dots was introduced. It is demonstrated that FIB irradiation can alter the switching and coupling characteristics of nanomagnets. In this chapter we take advantage of FIB irradiation to modify the magnetic properties. This modified switching characteristics may effectively yield to frustration-free magnetic ordering through non-reciprocal coupling. These new engineered Co/Pt dots can be exploited to

build NML devices with a more efficiently global clocking scheme and attractive circuit characteristics.

In Section 5.1, we first introduce the idea and our computational study of implementing partial irradiation to modify the magnetic properties of Co/Pt dots. The modified coupling behavior results in non-reciprocal coupling, which is a breakthrough of NML in controlling information flow. The discussion is presented in Section 5.2. Error-free NML built from partially irradiated dots is achieved from our simulations. The elementary logic units and in particular, a shift-register is shown in Section 5.3 and 5.4. Section 5.5 describes our optimization in searching for the most reliable irradiation pattern. The latest and pioneering experimental achievements are exhibited in Section 5.6.

5.1 Reversal of Partially Irradiated Co/Pt Nanomagnets

In Permalloy films, dot shape is the only design parameter: switching characteristics, domain structures can be defined by appropriately-shaped dots. In Co/Pt films, a large dose of FIB was initially implemented to pattern the dots. However, the usage of FIB irradiation is far more than that: a proper dose of FIB irradiation can be applied to engineer the magnetic properties of Co/Pt films, which gives an additional degree of freedom in our design.

In Chapter 4, we presented the reversal behavior of a FIB-cut nanomagnet with our calibrated computational model, where we found out the nucleation centers start from the boundaries due to FIB cutting. However, it is this accidental discovery that triggered our inspiration. A particularly interesting case is the one shown in Fig. 5.1: here the left side of the dot is intentionally irradiated with a higher dose and at larger area (i.e. dwelling points were applied on a wider area). The low-anisotropy region is 30 nm wide on the left side of the dot and only 10 nm along the other boundaries. Simulations show that switching starts from the stronger-irradiated left side, which is different from the reversal behavior in Fig. 4.8 a), where the nucleation sites almost start from every edges

simultaneously. Considering actually there are property variations from edge to edge, then nucleation event takes place randomly from one of the four edge in dots array. However, with partial irradiation on the left side, the nucleation always starts from the irradiated side. The edge where nucleation starts is defined by the extra irradiation and the process is well under control.

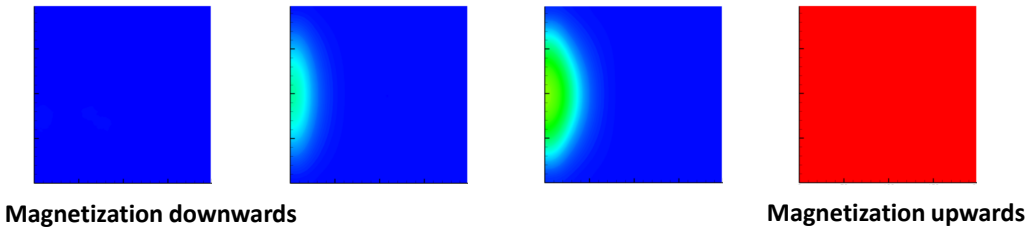

Figure 5.1. Snapshots of the switching of an asymmetrically irradiated 200 nm size dot. Anisotropy is changing linearly from $K_{\max} = 3.2 \cdot 10^5$ J/m^3 to $K_{\max} = 0$. The irradiated zone is 30 nm wide on the left side of the dot and 10 nm wide along other boundaries.

Our model certainly ignores many details about the effects of irradiation. The number of ions that define the edge of a 100 nm size dot is around 1000 – so fluctuations may play an important role. Exchange coupling may survive through the irradiated regions and we have no data about the local anisotropy in the heavily irradiated region where $K < 2.3 \times 10^5$ J/m. Thermal fluctuations certainly play an important role in the behavior of the highly-irradiated zones but considering them is beyond the scope of this dissertation.

Another difficulty is that all magnetic parameters (not only the anisotropy) may depend on the local ion dose. According to the literatures [106] [107], the saturation magnetization M_s remains almost unchanged up to well above the dose of $D_{\text{critical}} = 10^{14}$ cm^{-2}. We could not find data on the behavior of the exchange stiffness. However, since strong exchange is observed also in Co/Pt alloys [115], it is reasonable to assume that A_{exch} remains unchanged up to very high doses. According to our and other groups' experimental findings [109], layers irradiated with a $D > D_{\text{critical}}$ dose must be nonmagnetic / paramagnetic. We treat these highly-irradiated regions simply non-magnetic. The saturation magnetization and

the exchange stiffness (M_s, A_{exch}) are going abruptly to zero in the $D > D_{\text{critical}}$ region and only the anisotropy K changes continuously across the partially irradiated regions.

We tested a number of possible scenarios using different assumptions for the dot boundaries - regardless of the model details the soft edges always introduced nucleation centers and it was possible to create asymmetric switching (i.e. nucleation starting at one side only). We name this asymmetrically irradiated dots partially irradiated dots (PID). In the rest part of this dissertation, we will mainly focus on PID based NML.

5.2 Non-reciprocal coupling of partially irradiated dots

To study the effect of asymmetric irradiation to the stray-field interaction between dots, we investigated the field-coupling between a fixed-magnetization dot and an asymmetrically irradiated free dot. The sole role of the fixed dot is to provide a constant stray field for the free dot.

Fig. 5.2 shows the hysteresis curve of the free dot with the fixed dot being on the left (Fig. 5.2 (a)) and the right (Fig. 5.2 (b)) side. The figure insets sketch the geometry. The non-magnetic separation region between the dots is 10 nm wide.

The magnetic field of the fixed dot superposes on the external field experienced by the free dot. If dot magnetizations are parallel, the coupling field helps flipping the free dot. For the case of having antiparallel dots, the switching is hindered by the coupling. Due to the presence of the fix dot, the hysteresis curve of the free dot is shifted by a $2B_{\text{cpl}}$ field. We interpret the coupling field (B_{cpl}) between the two dots as half of the hysteresis-shift due to the coupling.

As seen from Fig. 5.2, asymmetrically irradiated dots show different coupling field to their left and right neighbor. The nucleation always starts at the higher-irradiated left side of the free dot. If the fixed dot is close to the nucleation site (i.e. it is on the left of the free dot) then ($B_{\text{cpl}}^{\text{left}}$) is large. If the fixed dot is on the right side, then the nucleation site experiences a smaller stray field, so $B_{\text{cpl}}^{\text{left}} > B_{\text{cpl}}^{\text{right}}$.

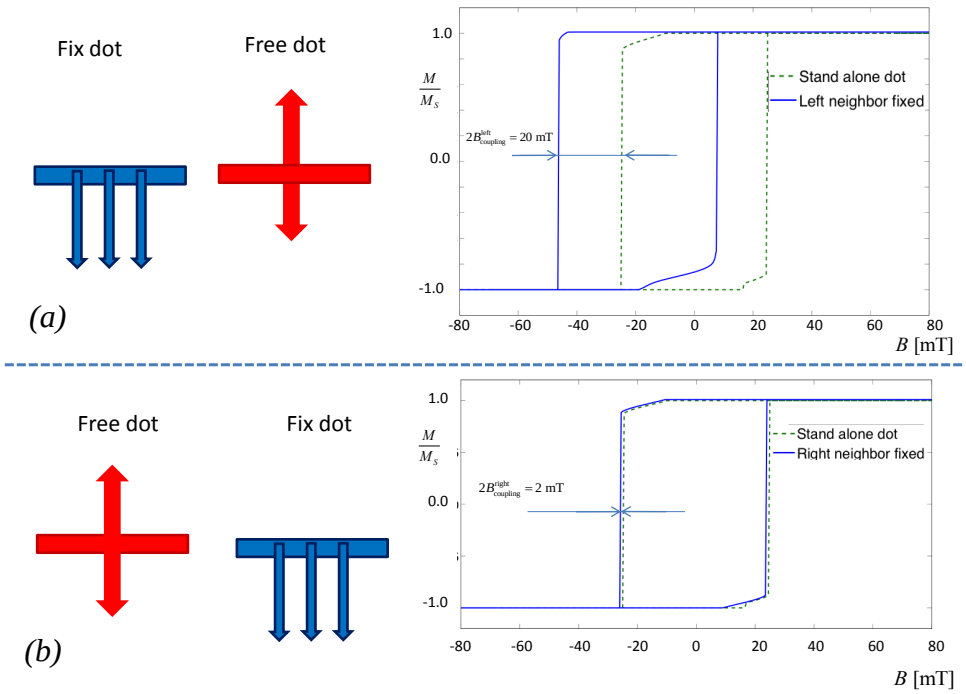

Figure 5.2. Switching of a partially irradiated dot, which is field-coupled to a fix dot from the left (a)) and from the right (b). Both curves are normalized to unity so that $|\mathbf{M}| = 1$. The hysteresis of the stand-alone free dot is also shown. Strong coupling changes the shape (width) of the hysteresis curve too, as the location of the nucleation site changes.

The difference is significant - in the example of Fig. 5.2, $B_{\rm cpl}^{\rm left} = 10$ mT, while $B_{\rm cpl}^{\rm right} = 1$ mT.

Consider now an arbitrarily long chain of nanomagnets with asymmetrically irradiated dots and a fixed dot at the left side. Initially, the chain can be in an arbitrary random (metastable) state. The chain is placed in an oscillating easy-axis (z out-of-plane direction) field. We assume there is only nearest-neighbor coupling. If the $B_{\rm osc}$ amplitude of this field satisfies

$$|B_c| - \left|B_{\rm cpl}^{\rm left}\right| + \left|B_{\rm cpl}^{\rm right}\right| < B_{\rm osc} < |B_c| + \left|B_{\rm cpl}^{\rm left}\right| - \left|B_{\rm cpl}^{\rm right}\right|, \qquad (5.1)$$

then a dot will switch if and only if its left neighbor is parallel-magnetized and the external field is antiparallel with the dot magnetization. B_c denotes the switching field of the stand-alone dot. The switching happens regardless of the magnetization state of the right dot.

Fig. 5.3 exemplifies how perfect antiferromagnetic ordering can be reached in a chain of asymmetrically irradiated nanomagnets. The oscillating external field 'drives out' ordering errors from the nanomagnet-chain and a frustration-free, antiferromagnetically ordered configuration results at the end. The structure decouples from the external field only when each dot is antiparallel to its left neighbor. An N-dot chain needs at most $N/2$ external field cycles to reach the antiferromagnetically ordered ground state. In other words, in the worst case, the information propagates 2 dots forward after each external field cycle.

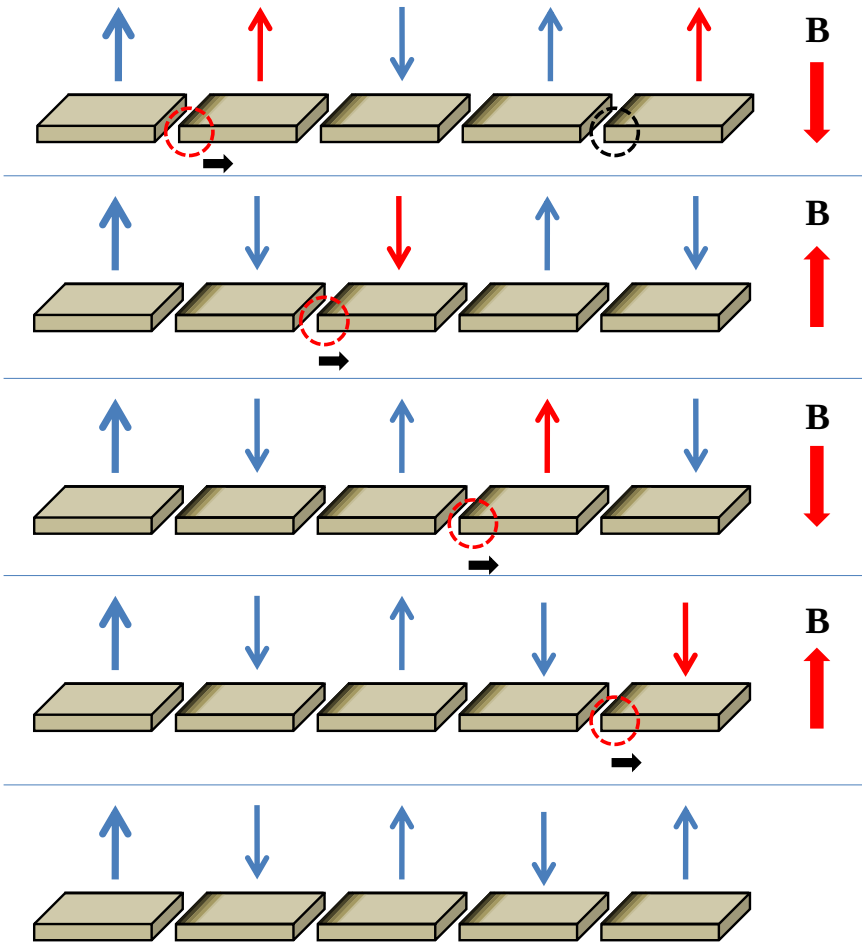

Figure 5.3. Illustration of controlled magnetic ordering of asymmetrically irradiated dots. The arrows on the right illustrate the external field. Each dot 'feels' the superposition of the external field and the magnetic field generated by its neighbors. Circles denote the regions where nucleation and subsequent switching takes place.

From a circuit point of view this structure is non-reciprocal: it allows a mag-

netic signal (the ordering, as it is dictated by the leftmost dot) to propagate toward the right but prevents the back-propagation of signals. Ordering errors (parallel dot-pairs) are driven out of the chain and perfect magnetic ordering results. As long as Eq. 5.1 is fulfilled, switching field variations and thermal fluctuations cannot frustrate the ordering. A sufficiently large margin between $B_{\mathrm{cpl}}^{\mathrm{left}}$ and $B_{\mathrm{cpl}}^{\mathrm{right}}$ provides perfect immunity against ordering errors.

The value of the $B_{\mathrm{LR}} = B_{\mathrm{cpl}}^{\mathrm{left}} - B_{\mathrm{cpl}}^{\mathrm{right}}$ margin depends strongly on the model applied for the irradiated zones. As we discussed at the end of Section 5.1, there are a number uncertainties about the correct $K(x)$ function and the spatial distribution of A_{exch} and M_s. For instance, if K goes all the way down to zero around all edges and the irradiated zones are wide (> 15 nm), then B_{LR} becomes small (nucleation may happen easily at any edge) and dot is prone to splitting into multiple domains. We performed a number of simulations by taking into account various scenarios for the unknown parameters in the micromagnetic model. The calculations showed that for reasonable choice of parameters, B_{LR} will be in the few millitesla range.

It is possible to achieve very high ($10 \sim 20$ mT) B_{LR} values by assuming irradiation (low-K) only at the left side of the dot. Such dots could be realized by a combination of two lithographic steps. For example, depositing the multilayers on a pre-patterned surface, single-domain nanomagnets without soft edges can be made. FIB could be applied subsequently to define nucleation sites along only one boundary of the nanomagnets.

5.3 Nanomagnet Logic from Asymmetrically Irradiated Dots

The concepts in Section 5.2 can be straightforwardly applied to two-dimensional arrangements of nanomagnets, i.e. when a particular nanomagnet has more than two neighbors. Nanomagnetic logic gates still can be constructed this way.

The key component of NML is a majority voting gate [24] [36], which can be turned into NAND / NOR gates to build arbitrary logic function - this is illustrated

in Fig. 5.4. More details about logic gate design in perpendicular media are given in [71] [74].

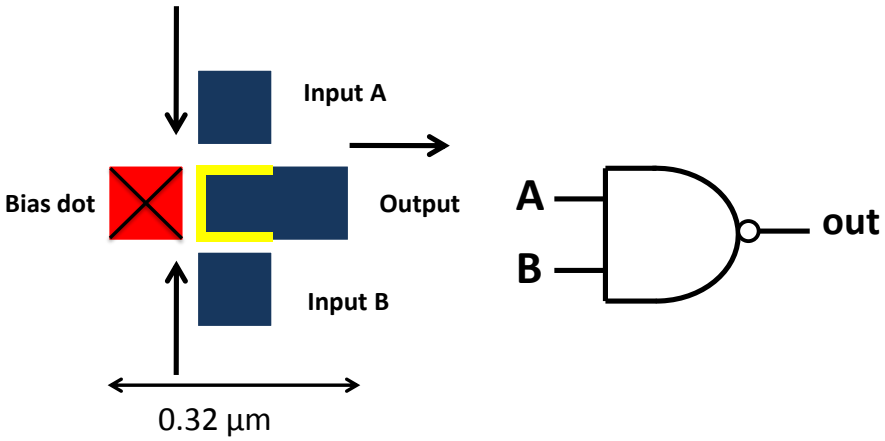

Figure 5.4. Schematics of an NAND gate. Irradiated zones are marked with a yellow line on the input sides of the output dot.

Most logic gates investigated in NML circuits so far were reciprocal and signals from the output could back-propagate toward the inputs. It is possible to separate the inputs and outputs to some extent with a gradient in the magnetic field - this may ensure that the inputs are already fixed when the outputs are switching. The field gradient may be generated by an appropriate clocking scheme on the underlying clocking wires [42] or adding 'block magnets' to the design [116], which modify local magnetic field. The field gradients are not required in the design of Fig. 5.4: the location of the irradiated zones ensures that the output dot is influenced only from the input side.

Sticking to the principle that the external clocking field should be sufficient to drive the metastable states to ground state but not affect the existed ground state, the working margin of the external field can be obtained by considering all the possible configurations in an NAND gate. Fig. 5.5 demonstrates the way to extract the margin in simulations. Since two of the inputs dots are placed symmetrically on the opposite sides of the output dot, the totally eight possible input configurations can be simplified to six cases as shown there. We performed our simulations assuming that dots can either have hard boundaries (without

irradiation) or partially irradiated soft boundaries. The lower anisotropy is 2.42 $\times$ 10^5 J/m^3 at the soft boundaries and 3.1 $\times$ 10^5 J/m^3 at non-irradiated parts. The soft edges are assumed to be 20 nm wide. A_{exch} = 1.5$\times$ 10^{-11} J/m^3 and M_s = 7.0 $\times$ 10^5 A/m are taken as usual. It is not difficult to find out that the working margin 48 $\sim$ 56.3 mT meets the request of an operating clock signal.

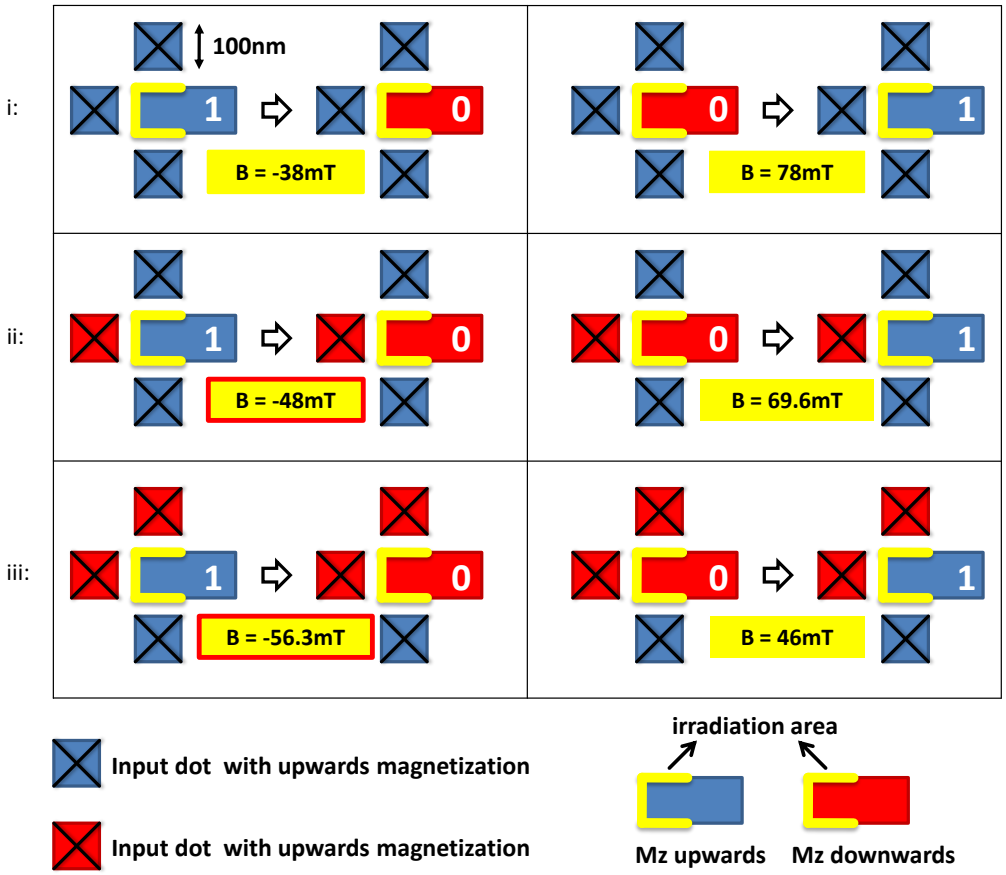

Figure 5.5. The switching fields of output dot in different configurations are simulated to illustrate the method to find the proper amplitude of external oscillating field. Bluish color stands for the magnetization pointing upwards, and reddish for magnetization downwards. Yellow stripes on the output dot indicate the partially irradiated regions.

An example of a more complicated design of an XOR gate is shown in Fig. 5.6. It combines four majority gates, which are operating as NAND gates, as shown in Fig. 5.4. Fan-outs are straightforwardly realized by dots that have multiple neighbors on their non-irradiated sides. There are a few elongated-shaped dots in the layout of Fig. 5.6: they enable the construction of inverting or non-inverting

chain segments with the same length.

The truth table of the XOR gate can be found by propagating the input signal (from A and B) to the output. Each dot relaxes into its ground state with respect to the majority of its neighbors on the irradiated sites. Micromagnetic simulations verified that the system indeed went into the expected state.

The B_c switching fields depend on dot size and the number of soft boundaries (the number of neighbors: some serve as inputs, others as outputs). These result in numerous constraints - in principle, similar to Eq. 5.1 - that should be fulfilled for any dot.

The same NAND gates in Fig. 5.5 are applied in the XOR gate, together with one-side irradiated dots in the chain , where the lower anisotropy is adjusted to 2.6×10^5 J/m^3. All other parts of the dots are set to $K = 3.1 \times 10^5$ J/m^3.

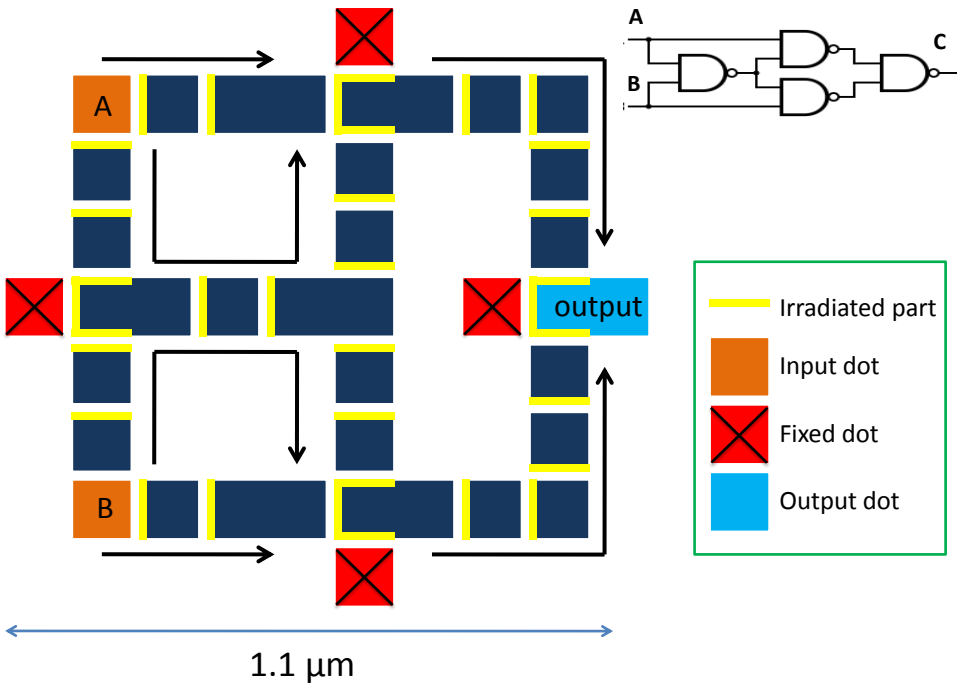

Figure 5.6. Schematics of an XOR gate, built from asymmetrically irradiated dots.

Using these parameters, the magnitude of the clocking field should be 50 mT $< B_{\mathrm{osc}} <$ 56 mT. Choosing $B_{\mathrm{osc}} = 53$ mT, in the middle of the range, so the scheme can tolerate a few milliteslas of switching field variations for each of the

dots.

Smaller B_{osc} clocking fields would be easier to generate on-chip and the device operates with less power. We found that B_{osc} could be reduced all the way down to 10 $\sim$15 mT by using somewhat bigger dots (150 nm size); lower K_{film} value and correspondingly reduced anisotropy for the soft boundaries. Reducing K_{film} can be done by an initial, homogeneous FIB irradiation over the entire film and / or by changing growth conditions and / or layer thicknesses.

5.4 A shift-register type memory device

Nanomagnet logic requires the magnetic system to be ordered into a computational ground state. But the asymmetric dots may also be used to build shift registers where information is represented by the presence / absence of metastable states; and these metastable states propagate in a controlled way.

A possible scheme is to represent binary information by quadruplets of dots. We use the following definitions: if a four-dot segment is in ground state (either in $\uparrow\downarrow\uparrow\downarrow$ or $\downarrow\uparrow\downarrow\uparrow$ state) then it is interpreted as logic '0', while a quadruplet with a metastable dot pair ($\uparrow\downarrow\downarrow\uparrow$ or $\downarrow\uparrow\uparrow\downarrow$) is interpreted as '1'. The shift register carries the information by the presence (or absence) of a metastable pair (parallel magnetized dots) in the middle of the quadruplet. The metastable dots are separated by stable (ordered) sequences. A chain of $N = 4n$ dots may carry n bits of information.

For each external field cycle, the bit pattern steps toward the right. New information can be written in at the left and bits leaving the structure are read out on the right. Fig. 5.7 illustrates the operation of the shift register for a particular sequence of bits. It is easy to verify that neighboring dots never switch simultaneously - the metastable states (the bit pattern) make two steps to the right in each field cycle. This results in a precisely controlled shift of the bit pattern.

There are a number of actively researched proposals to build nonvolatile mem-

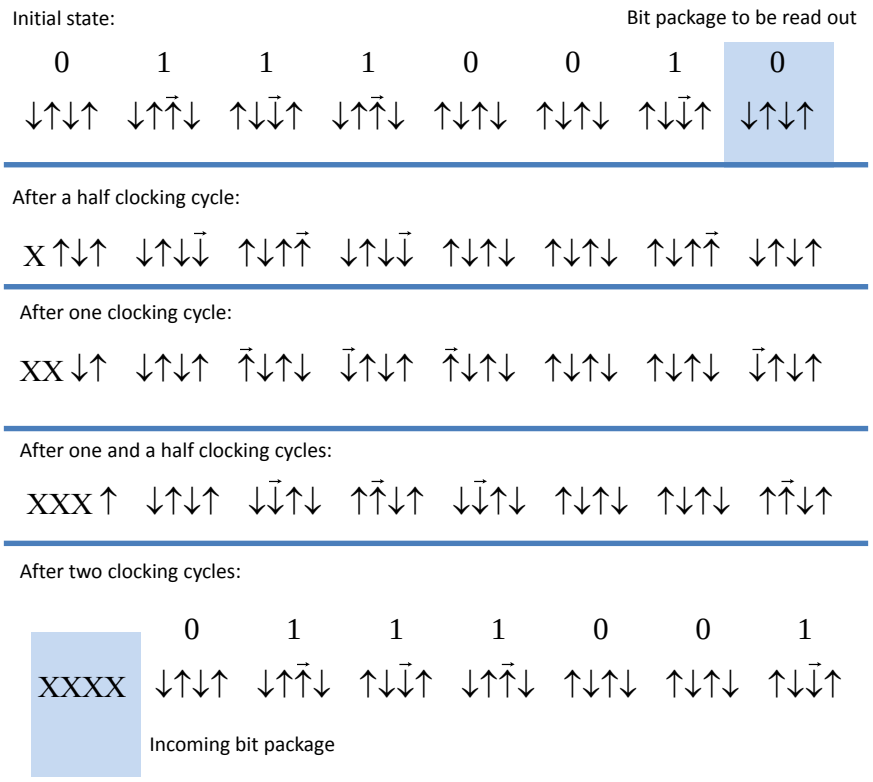

Figure 5.7. Operation of the shift register for a particular bit sequence (01110010). The lines show the migration of the bit pattern after an easy-axis (up - down) field sequence is applied. Dots marked by a small horizontal arrow ($\rightarrow$) are in metastable state and will change in the next clocking cycle. Bits stepping in from the left are denoted by the X symbol - their state is determined by a left neighbor, which is not shown.

ories from magnetic domain-wall shift registers [17] [117]. It is straightforward how to exploit our device for a dot-based shift register. The state of the first (leftmost in Fig. 5.7) can be set by the Oersted fields of a nearby current wire or spin-torque, the state of the last (rightmost) dot is read by a magnetoresistance sensor or a tunnel junction stack. The benefits of such storage device are high integration density, fast data throughput (magnets switch in nanosecond time scale) and no endurance issues (magnets withstand practically infinite number of switching cycles). Power dissipation is in the few-ten k_BT range per switching. The oscillating fields may be generated by on-chip inductors. These inductors clock large blocks of magnets (possibly all of them on the chip - so they could be large and made by an inexpensive technology.

5.5 Optimization of partial irradiation pattern

In short, the technical know-how to achieve non-reciprocal coupling in NML can be summed up as (1) enhancing the expected coupling and (2) bringing down or avoiding the non-expected coupling from the neighbors. Toward this end in view, we made a further optimization on the partial irradiation scheme, though the earlier model proved already working.

The optimization is carried out by changing the irradiation area on the dots. In the earlier work, we assumed the relevant edges were homogeneously and completely (over the area) irradiated, as shown in Fig. 5.8 (a). However, at the corners of the chains and in majority gates, we have observed undesired parasitic couplings because the distance from the irradiated part (in the circle) is close to more than just one neighbors, which may possibly lead to back-propagation. For this reason, we can use elongated dot to weaken this effect at the corners, but at the cost of increasing area consumption. Nevertheless, the parasitic effect cannot be eliminated in majority gates with the former irradiation scheme.

Therefore, we improved our irradiation scheme. The idea is shown in Fig. 5.8 (b), where only the middle part of the edges are irradiated. With this new irradiation scheme, the irradiation sites are further apart from the irrelevant dots so that the parasitic coupling is reduced. It is not only suitable for corners, but also for the majority gates. With implementation of simulations, we verified the shift of hysteresis in a stand-alone irradiated dot remains as long as the irradiation area is above a certain value, which we define as the minimum of nucleation volume (about 30 nm $\times$ 30 nm). In other words, the non-reciprocal behavior remains.

We redid the simulation of the XOR gate with this optimized irradiation scheme. With some minor changes of the irradiation dose, we got similar results. The anisotropy distribution is plotted in Fig. 5.9 (b). In the later experiments, this irradiation scheme is chosen, ensuring better working performance and reducing the error rate.

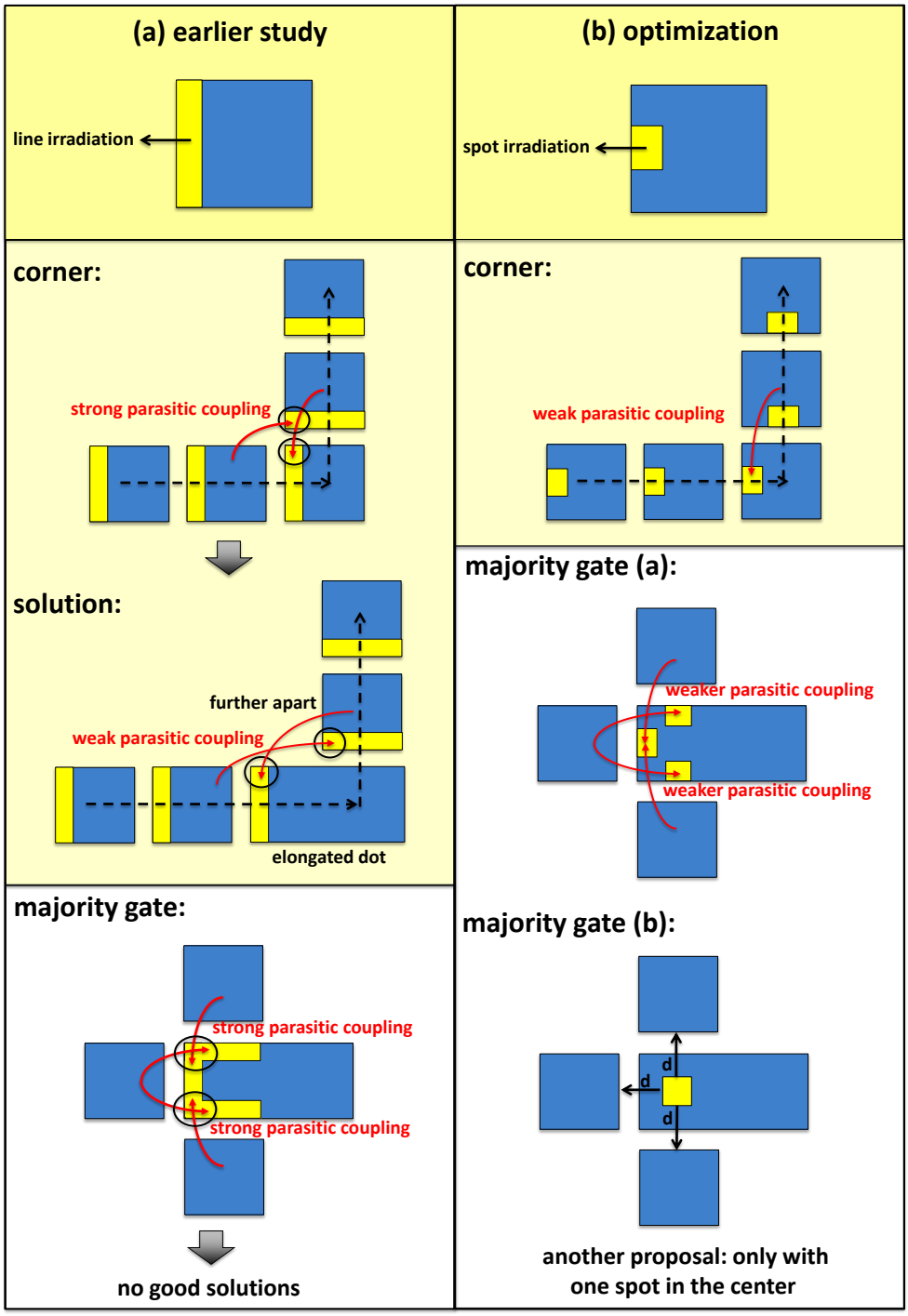

Figure 5.8. Comparison between irradiation schemes.

5.6 Experimental implementations from partially irradiated Co/Pt nanomagnets

Our computational study successfully verified that partially irradiated dots can result in well controlled and error-free information flow. In this section, we

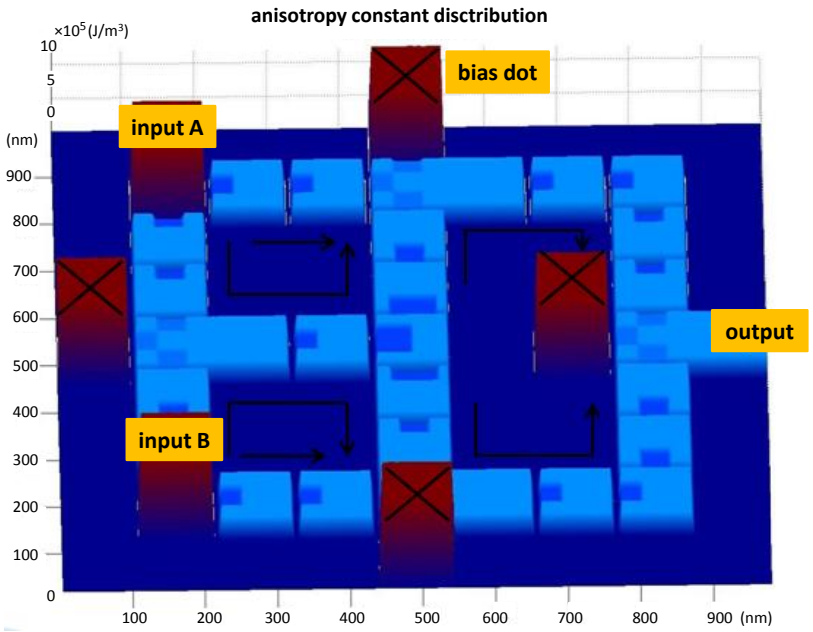

Figure 5.9. Three dimensional perpendicular anisotropy distribution of a XOR gate.

demonstrate some of the latest results from our experiments, including fan-out structures, an inverter chain and a majority gate. The experimental work was done by our experimental group from Lehrstuhl für Technische Elektronik (LTE).

5.6.1 Controlled reversal of Co/Pt dots with partial irradiation

It is already demonstrated a lower switching field of Co/Pt multilayer in [108] [118] [119] and the nucleation event induced by FIB irradiation [120]. Thanks to the great efforts from LTE. Based on their earlier solid study of the magnetic properties of Co/Pt films [71] [72] [73] [74] [75] [76] [77] [78], our group continue our investigations on the reversal behavior of partially irradiated dots for NML.

In [83], partial Ga^+ FIB irradiation on single-domain Co/Pt dots was explored. As a basis of developing complex NML systems, the switching behaviors of Co/Pt dots with varying irradiation doses and sizes were experimental demonstrated. By locally intermixing the interfaces of Co/Pt multilayer, the intrinsic anisotropy can be significantly lowered. It has been verified from this work that the reversal is governed by the artificial FIB irradiation-induced weakest point – nucleation

center. The switching always starts from the nucleation. Also the switching field distribution becomes narrower compared to the as-grown case.

A fanout structure is fabricated as a case study of the reversal of nanomagnetic structure raised from irradiation-induced nucleation. As shown in Fig. 5.10, this structure has one input and two outputs with small pads at the ends for the convenience of MOKE measurements. The middle part of the input pad is irradiated with a high dose of 1×10^{14} ions/cm^2. The switching field of the input pad is reduced to 93.3 mT measured by MOKE. The switching field of two output pads are 94.0 mT and 94.3 mT respectively. The two MFM images in Fig. 5.10 (b) and (c) exhibit the magnetization states before and after the switching. Taking thermal noise into account, these three switching fields equal, indicating that after the reversal starts, domain wall propagates through the whole structure without intermediated pinning. To our knowledge, this is the first time a partially irradiated structure for NML application was demonstrated in experiments.

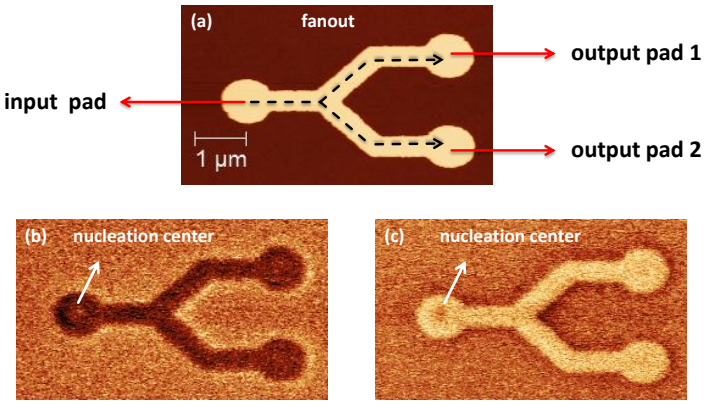

Figure 5.10. The fanout structure with partially irradiation. (a) is the geometry. (b) and (c) are MFM images showing the two opposite states [86].

5.6.2 Error-free, directed signal transmission by an inverter chain.

In logic devices, NOT gates, AND gates and OR gates are the elementary units. With these fundamental logic functions implemented, in principle, any arbitrary digital computing can be realized. In Co/Pt based NML, NOT function

can be achieved using dots with the total number being even; AND and OR gates can be achieved with majority gates. We discussed the ordering errors occurred in long chains before, where no partial irradiation involved. We also theoretically demonstrated that it is possible to achieve error-free ordering by applying partial irradiation via non-reciprocal coupling. However, there we neglected the thermal influence and we assumed a good switching field distribution (SFD). In experiments, the thermal fluctuations and process variations such as shape variations, anisotropy variations and coupling variations all lead to a widened switching field distribution. A broad SFD may significantly diminish or even vanish the working margin of the required external fields. As sketched in Fig. 5.11, the amplitude of a proper external clocking field should lie in the green interval. The ideal case (a) reflects the constant switching field used in our earlier computational study, while case (b) and (c) take the SFD into account. If there is no overlap between the two SFD of two different configured states, the green interval becomes smaller compared to the ideal case, but it still exists there. However, if the SFD disperses too much, one overlap between the two SFD appears, which results in the problem of having possible error switchings during processing [121]. The larger the overlap is, the higher the error rate will be. Hence, in experiments it is important to minimize the SFD in order to have a reliable system.

Now we exhibit our first attempt in experiments by using partially irradiated dots to verify our simulation model and the feasibility of having the green interval for the clocking field. Note instead of the Co/Pt ML stacks used in simulations, here a new thin multilayers – Co/Ni ML stacks have been explored.

The Co/Ni composition ($\mathrm{Ti_{2nm}Au_{10nm}Pt_{5nm}}8 \times [\mathrm{Co_{0.2nm}} + \mathrm{Ni_{0.4nm}}]\,\mathrm{Pt_{5nm}}$) was used in experiments. Co/Ni multilayers contain only magnetic atoms (Pt layer in Co/Pt is weakly or non-magnetic) and are expected to offer higher coupling fields and lower switching fields [122], which both are advantageous in our case. Enhanced coupling ensures error-free information flow; while lower switching fields promises a lower power consumption. The detailed preparation of Co/Ni film is

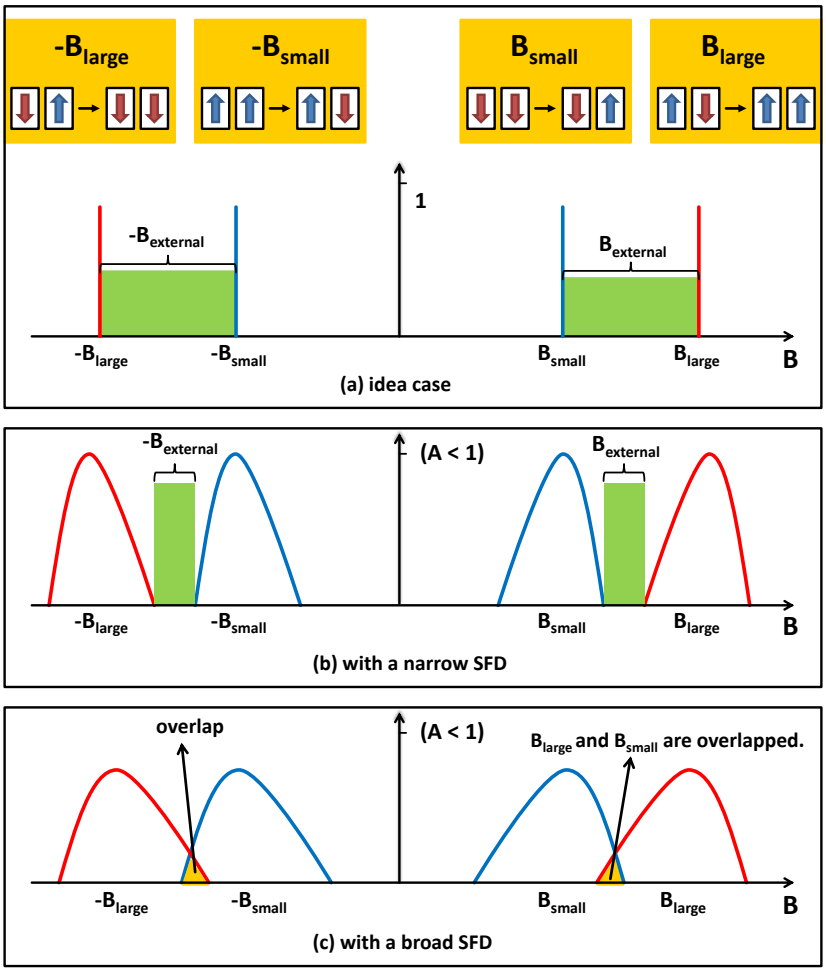

Figure 5.11. The switching field distribution dependence of the working external fields.

described in [84]. The fabricated as-grown dots are demonstrated in Fig. 5.12. These Co/Ni dots are partially irradiated at the middle part of the left end. The dot size is 1 μm $\times$ 1 μm. A global oscillating field is applied to the dots and drive the information propagate from left to right. The MFM images in Fig. 5.12 reveal the states of the dots after every clocking pulse. With the amplitude of external field being 61.5 mT, the correct information steps forward after each pulse until one frustration happens between the 6_{th} and 7_{th} dots. The coupling turns out to be weaker due to the misalignment of irradiation center so that an extra effort need to be made from the external field. A raise of the external field to 65.5 mT is sufficient to drive the information forward. In the end, error-free

antiferromagneitcally ordered state is reached.

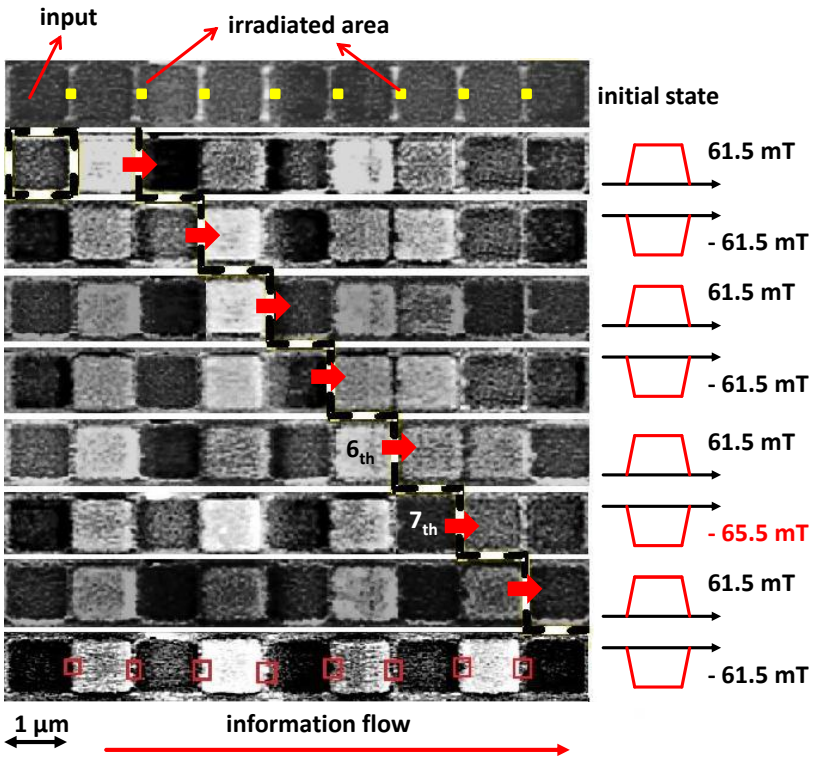

Figure 5.12. Information propagation in the partially irradiated Co/Ni chain [84].

The experimental result further verifies our computational results. With non-reciprocal coupling, the error state can be wiped out by a proper external field and the information can be well controlled by irradiating the corresponding area of the dots. More experimental work is dedicated in having a better control of the information flow with a lower external field in the promising Co/Ni multilayer films.

5.6.3 A majority gate with partial irradiation

In experiments, the proposed irradiation method (a) in Fig. 5.8 turned out not working well because it asks for a very precise control of the FIB. Any inaccuracy, such as the misalignment from beam center to the geometry spot center, may lead to a different coupling strength from different input dots. Compared to (a), the proposal (b) is more practical since there is only one focused irradiation center, which reduces the required precision of FIB irradiation.

The SEM images of our fabricated structure is illustrated in Fig. 5.13 [85]. The multilayer stack is with a composition of $Pt_{5nm}\,[Co_{0.4nm}Pt_{1.0nm}]_{\times 8}\,Pt_{5nm}$. FIB lithography on a PMMA photoresist and ion beam etching are used to pattern the structure. The inset in Fig. 5.13 shows the topology of this majority gate and large pads are for the convenience of MOKE measurements. The output dot is irradiated in the center area of 20×20 nm^2 with a dose of 1×10^{14} ions/cm^2 using 50 kV Ga^+ ions. The central position of the irradiation center ensures equal votes from each input.

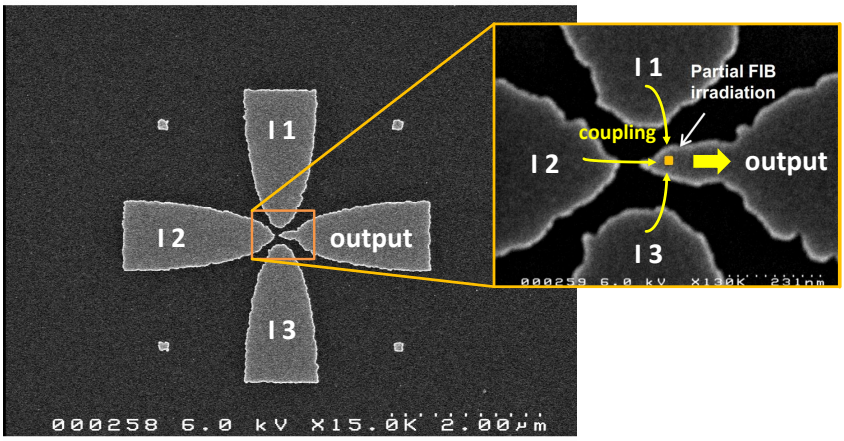

Figure 5.13. The fabricated majority gate with partial irradiation [85].

The coercivity of the three non-irradiated input pads are measured as $B_{I1} = 476$ mT, $B_{I2} = 489$ mT and $B_{I1} = 538$ mT. By applying an out-of-plane external field, the output pad switches at different fields with different combinations of the input magnetization states. The switching fields of the output with all the input configurations are listed in Table 5.1. The imperfections of dot shape and positioning, together with the thermal noise cause the slight difference when there are two inputs at logic '1' and one input at logic '0' (or vice versa), but the mean switching fields of output from '1 to '0' and from '0' to '1' turned out to be very consistent. From the data, theoretically an oscillating external field with an amplitude in the window of 117.5 mT $\sim$ 127 mT can drive the majority gate to the anti-parallel state of the input majority, without disturbing the already

correct ordered dots. In experiments, the switching field distribution is broadened due to the thermal noise. Therefore, the working window is narrowed. An external field with the amplitude of 122 mT successfully ordered the majority gate, and this process is reproducible. Fig. 5.14 shows the MFM measurements of ordered majority gates in an external clocking.

TABLE 5.1. SWITCHING FIELDS WITH ALL THE INPUT COMBINATIONS.

I1	I2	I3	$B_{1\to0}$ (mT)	$B_{0\to1}$ (mT)
0	0	0	-134.5	104.5
0	0	1	-127.5	117.5
0	1	0	-128.0	116.5
1	0	0	-127.0	115.0
0	1	1	-116.0	127.5
1	0	1	-116.0	127.0
1	1	0	-127.0	129.0
1	1	1	-106.5	135.0
Mean value			-121.6	121.5

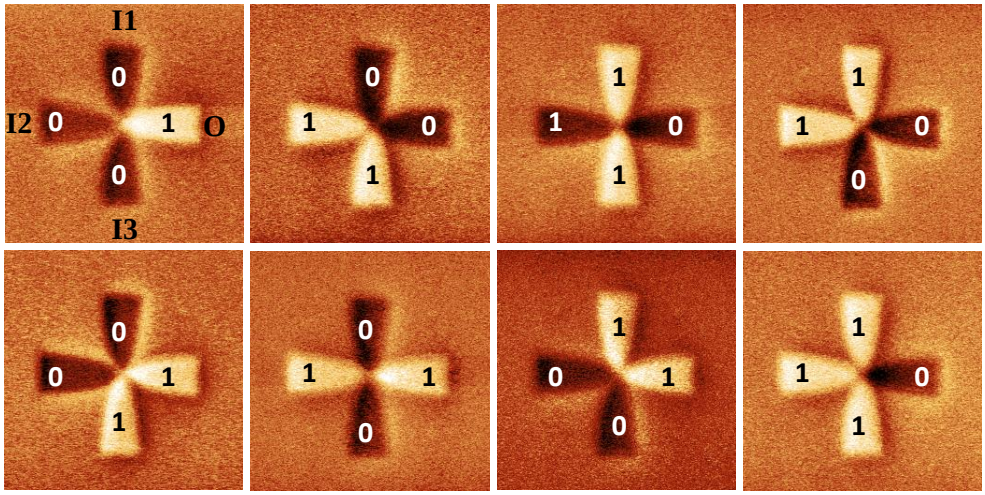

Figure 5.14. The ordered majortity gates with all the input configurations [85]. The output (O) is always antiparallel to the majority of the inputs (I1), (I2) and (I3).

By catching the geometry from the SEM images of this majority gate, we can simulate the reversal behavior of this majority gate with about the same shape and size. We assume besides the irradiated area, the anisotropy is homogeneous. Note here both the layer number and layer composition are different from the formerly

used 5 ML films. Therefore, the simulation parameters need to be recalibrated. The saturation magnetization is taken as 7.0×10^5 A/m. With the measured switching fields of three inputs being 476 mT, 489 mT and 538 mT, we can find anisotropy $K = 4.7 \times 10^5$ J/cm^3 by best fitting the hysteresis curves of each stand-alone input, which is actually much larger than the anisotropy value of the 5 ML film.

We estimate that the lower anisotropy in the irradiated area exhibits a Gaussian distribution. The anisotropy in non-irradiated area of the output is also set to 4.7×10^5 J/cm^3. The lowest anisotropy in the irradiated center is adjusted to 2.0×10^5 J/cm^3 in order to match with the coercivity of output (121.5 mT), regardless of the inputs. The final anisotropy distribution used in our simulation is presented in Fig. 5.15.

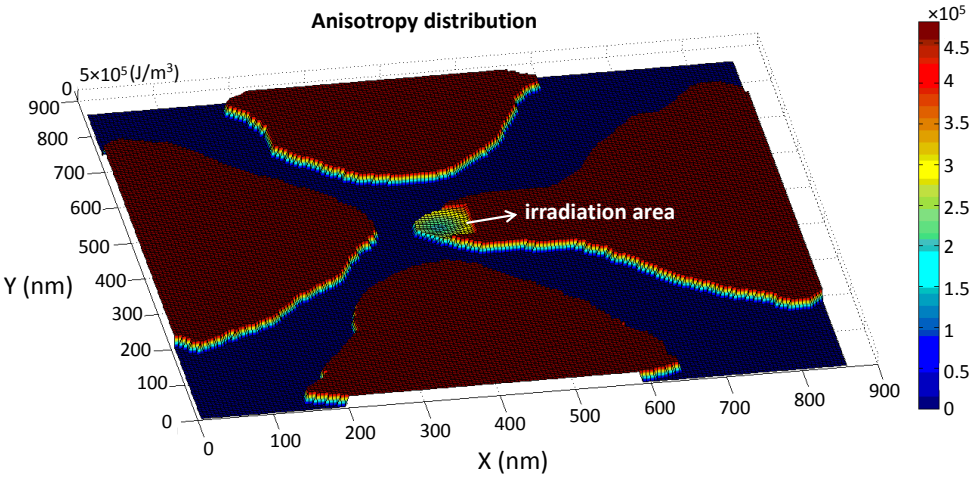

Figure 5.15. The anisotropy distribution used in the OOMMF simulation.

With these simulation parameters, our simulations predict correct operation of the majority gate with the switching fields in the range of 108 $\sim$ 141 mT listed in Table 5.2, which agree very well with our experimental data, further verifying the feasibility of using partially irradiated dots in the design of NML devices.

TABLE 5.2. SWITCHING FIELDS OF OUTPUT FROM OOMMF SIMULATIONS.

I1	I2	I3	$B_{1\to0}$ (mT)	$B_{0\to1}$ (mT)
0	0	0	-141.0	108.0
0	0	1	-129.0	120.0
0	1	0	-135.0	114.0
1	0	0	-123.0	126.0
0	1	1	-126.0	123.0
1	0	1	-115.0	134.0
1	1	0	-120.0	129.0
1	1	1	-109.0	140.0

5.7 Summary

In this chapter we theoretically studied NML devices based on perpendicularly magnetized media. We demonstrated that using appropriately chosen irradiation doses, one can engineer the switching and coupling properties of Co/Pt single-domain nanomagnets. We showed that asymmetrically irradiated dots coupled non-reciprocally, i.e. with different fields to their left and right neighbor. Dipolar ordering under an oscillating field takes place in a deterministic and controlled way, unlike the demagnetization of a reciprocal array, which is a stochastic process, inevitably leading to frustration.

We demonstrated two design examples: an XOR gate ordering in homogeneous field and a shift register. The magnetic ordering is robust and well controlled in these devices and there is no inherent limit to their scalability. We are currently working on the experimental observation of the switching of asymmetrically-irradiated dots and gates.

There is a vast design space for Co/Pt based nanomagnets. Applying different layer thicknesses, layer numbers, shape anisotropy and irradiation profiles all can change their properties. The scalability is limited by the scattering of ions in the film and the substrate, but dot-to-dot separations below 10 nm could be achievable. Other perpendicularly magnetized multilayer systems (such as Co/Pd and Co/Ni) show similar behavior under irradiation and are worth being considered for the

construction of logic devices.

We investigated mainly one particular five-multilayer film. This type of magnetic film is well known to our group [75] so we could make reasonable assumptions to the simulation parameters. Considering other film compositions provides a lot of room for optimization. Reducing the required clocking fields to the few-millitesla range while maintaining robustness of the NML circuit is another focus of future work.

Nanomagnet Logic is one of the promising 'beyond roadmap' nanotechnologies and it offers benefits that are beyond reach with traditional CMOS-based, wired electronic components. Introducing new materials brings new opportunities for engineering novel NML circuits with attractive characteristics. We demonstrated that FIB-induced local change of magnetic properties is a powerful method to achieve new functionalities in magnetic computing.

CHAPTER 6

AN N-BIT SYSTOLIC PATTERN MATCHER FOR NANOMAGNET LOGIC

6.1 What's systolic architecture?

H. T. Kung and Charles E. Leiserson first described the concept of systolic arrays in [123]. In computer architecture, a systolic array is a pipe network arrangement of data processing units (DPU), usually called processing elements (PE). The idea of using systolic architecture is to improve computing speed with parallel computing and reduce the requirement on I/Os in specific applications [124].

In systolic arrays, matrix-like rows of PEs receive, compute and send data streams. The output of one PE usually acts as the input of the neighboring PE. Data streams may flow in different directions in the array [124]. Systolic arrays provide massive parallelism; their regular layout and the lack of long-range interconnections support nanoscale implementations. As with many other 'nano-friendly' circuits, systolic arrays are specialized for particular applications and it is difficult to configure them for general computing tasks.

The structure of a systolic array is demonstrated in Fig. 6.1, where identical PEs compute data and communicate with their neighbors. Only the PEs at the border of the array can communicate outside. The task of one PE can be summarized as: receiving data – computing data – transmitting data.

Systolic structure has the advantages of parallel computing and good scalability, but at the cost of being expensive and highly specialized for particular applications.

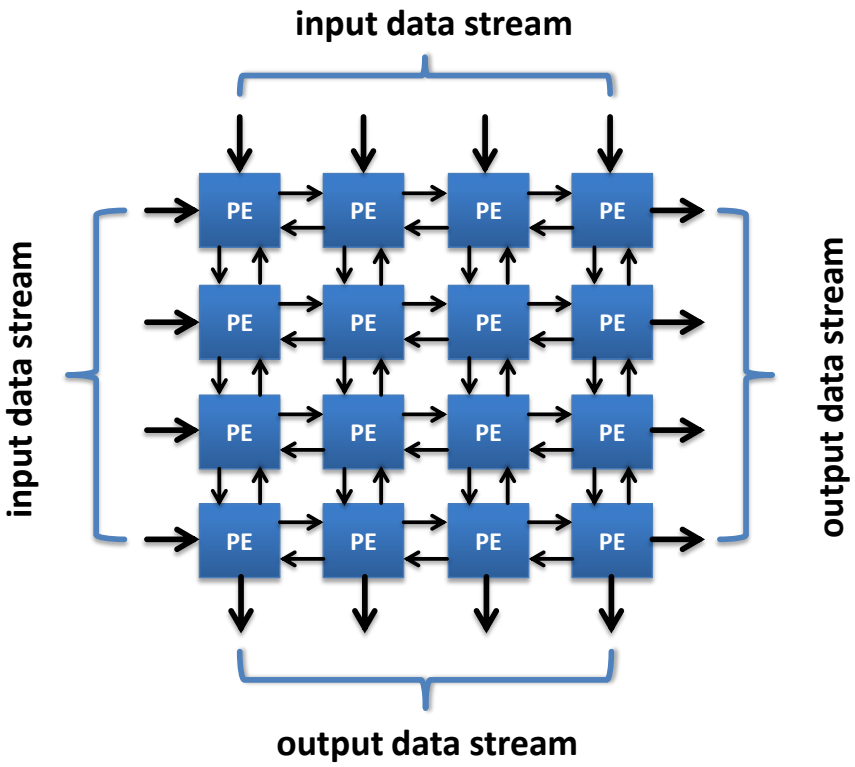

Figure 6.1. The structure of a systolic array.

6.2 Why is systolic architecture suitable for NML?

Basic logic gates (and more recently a full adder [37]) have been already realized, but the scalability of NML for larger-size circuits is yet an open question. Thermal fluctuations, shape variations may be problematic and yield to NML computation errors and it is well-known from physics that larger-scale, interacting systems do not order without frustrations. If the ordering of nanomagnets is well-controlled by appropriately applied clocking fields, then errors can be avoided and the NML systems fall into its computational ground state. The feasibility of scalable NML circuits largely relies on a well-designed clocking scheme [42].

We have demonstrated theoretically [82] and very recently experimentally [84] that FIB- irradiated Co/Pt dots enable an effective clocking scheme, which yields to deterministic, error-free ordering and bit-level pipelining in a homogeneous magnetic field. So far, the concept was demonstrated on few-dot structures and the purpose of this chapter is to show the implementation of a complex, scalable,

practically useful circuit.

On one hand, circuits with irregular layout are challenging to realize in NML: there is no demonstrated solution for wire-crossing and long-distance nanomagnet-wires have long latency. On the other hand, nanomagnets naturally lend themselves for the implementation of pipelined architectures. We choose a systolic architecture to demonstrate large scale NML circuitry, which relies heavily on pipelining and does not require irregular gate to gate connections. The simple structure of systolic array offers the first advantage for NML design. In addition, systolic architecture is built up with PEs and the components in each PE are identical. All the components are scalable, which also makes systolic array a good candidate for NML circuits.

The rest content of this chapter is organized in the following: in Section 6.3 we review the logic-level description structure of an N-bit systolic pattern matcher (SPM), based on the well-established literature of SPMs. Section 6.4 briefly summarizes our earlier, physics-level simulations of FIB-irradiated Co/Pt nanomagnets. Building on this background, Section 6.5 demonstrates the design of the SPM and Section 6.6 presents detailed, physics-based simulations. In the end, Section 6.7 compares the performance characteristics (speed, dissipation) between a CMOS-based SPM and an NML-based one.

6.3 High-level structure of an N-bit systolic pattern matcher

As a specific systolic design, systolic pattern matchers (SPMs) are used to find the occurrences of a binary W pattern in an X binary stream. This functionality has applications in image and sound processing, network security, information retrieval etc. Fig. 6.2 illustrates the structure of a one-dimensional n-bit pattern matcher built up from n PEs (n stands for the number of PEs in this SPM). The fundamental PE in a SPM circuit is relatively simple. Each PE consists of one XNOR gate and one AND gate. The elements of the W pattern are stored in such a way that the first bit W_1 is saved in PE_1 (the leftmost), the second bit

W_2 in PE_2, and the ith bit W_i in PE_i. (Notably, we can take advantage of NML's non-volatility to store this bit directly at the gate – with no static power loss. The W bits are programmable via spin transfer torque (STT).) The input data stream steps in the SPM from left and propagates to right. As soon as the first bit of the input stream reaches PE_1, the comparison starts. Y_i indicates the global matching history for the first i-bit long segment of X. This global histrory (Y_1, Y_2 ... Y_n) is then shifted from right to left, and the final output Y_n is read out from PE_n, telling if the n-bit long segment from the input stream matches with the n-bit pattern. The process in each PE can be decomposed into three steps: 1) the ith PE takes the ith bit from the input segment X_{in} and sends it to its XNOR gate. 2) the XNOR gate compares this bit with the corresponding W_i pattern bit. The result of the comparison is sent to the AND gate of this PE. 3) the AND gate takes both responses from its XNOR gate and the $(i-1)$th AND gate (which is Y_{i-1} from the right PE), generates a new response Y_i, and sends it to the next PE ($(i+1)$th PE on the left side). These three steps repeat n times from PE to PE to achieve output Y_n for this segment. If at any point the output of an XNOR gate is a '0', the accumulated global history is set to '0', which suggests that there is no match in input stream bits $X_m \cdots X_{m+n-1}$.

If and only if the segment of the X input data is completely matched with the W pattern, the output will be logic '1', otherwise the output will be logic '0'. Subsequent values of the Y_n output indicate match / mismatch for the next n-bit long segments of X_{in}.

Note that given this bi-directional dataflow, there are some architectural-level timing constraints that must be satisfied. For instance, bits of the input stream must be 'spaced' two PEs apart to ensure that global history bits and streaming input data meet at the proper time. An obvious detriment to this is that the throughput of the system will be degraded as output bits will also be spaced two PEs apart. However, there is no reason that two different input streams cannot be interleaved within the systolic array. In other words, two different data streams

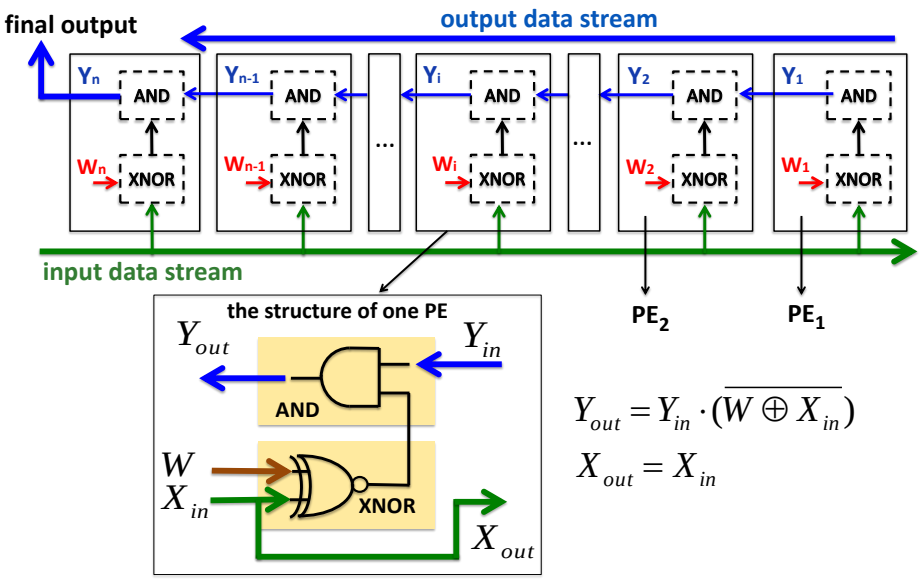

Figure 6.2. Information flow between PEs: input data stream X propagates from left to right; response data stream steps forward from right to left. The output comes out from the leftmost PE.

could share the array hardware – assuming that one would want to search for the same pattern in each. Interleaved dataflow would allow for full hardware usage and the highest possible throughput.

6.4 Physical interactions between patterned and irradiated Co/Pt nanomagnets

Logic operations in Co/Pt based NML are based on majority logic, just as in the case of in-plane NML. Magnetic dipole coupling between single-domain nanomagnets aligns each dot antiparallel with the majority of its neighbors [36] and the ordered ground state of the magnets represents the result of the computation. The reader is referred to [74] [76] [79] [84] [85] for recent results on Co/Pt based NML.

The reversal behavior of Co/Pt nanomagnets is markedly different from Permalloy nanomagnets: while $40-100$ nm size Permalloy dots remain single-domain during switching ('coherent rotation'), Co/Pt nanomagnets in this size range switch through nucleation and domain wall propagation. The nucleation site can be defined by an FIB irradiation: the irradiation locally changes the crystalline structure

and decreases crystalline anisotropy [106], defining a 'soft spot' where the domain wall starts [112]. We developed a computational model of such partially irradiated dots [80], which were later confirmed experimentally [84].

The irradiated spot can be placed on particular sides of the dot, consequently the dot can be couple to its neighbors with different strength. This is schematically shown in Fig. 6.3 a) - here the middle dot couples only to its left neighbor. For a detailed study, see [82]. Since the dot is sensitive only to the coupling field of particular neighbors, error-free demagnetization of coupled nanomagnets can be reached in an uniform oscillating field along the easy magnetization axes. The field amplitude, B_{osc} is chosen in such a way that only metastable dots (i.e. parallel dot pairs) are affected by the field and the metastable state is eventually driven out from NML system. Partially irradiated Co/Pt nanomagnets are inherently pipelined on the bit level. One sketch showing a majority gate and a chain is given in Fig. 6.3 b). After each oscillation period of the external field, the metastable-state ordered chain makes one step toward the output, as illustrated in Fig. 6.3 c). The speed of the device is determined by the period of the clock field T_c. New inputs can immediately be applied after the ordering process completes for the first few dots in the chain.

For the simulations, we used the same parameters as in Section 5.3. The size of each square dot in Fig. 6.3 b) is 100 nm by 100 nm and the size of each elongated dot is 210 nm by 100 nm. The distance between neighboring dots is 10 nm. We use hard, non-irradiated dots as inputs in the design: their switching field is much higher than the switching field of irradiated dots and they deliver a local, constant coupling field to the nanomagnets.

6.5 Design of an N-bit systolic pattern matching circuit

Ideally, the layout of a pattern matching PE should (1) facilitate the dense tiling of arbitrary number of PEs on the chip area and (2) all PE outputs should be computed after exactly the same clocking steps, so that data streams are in

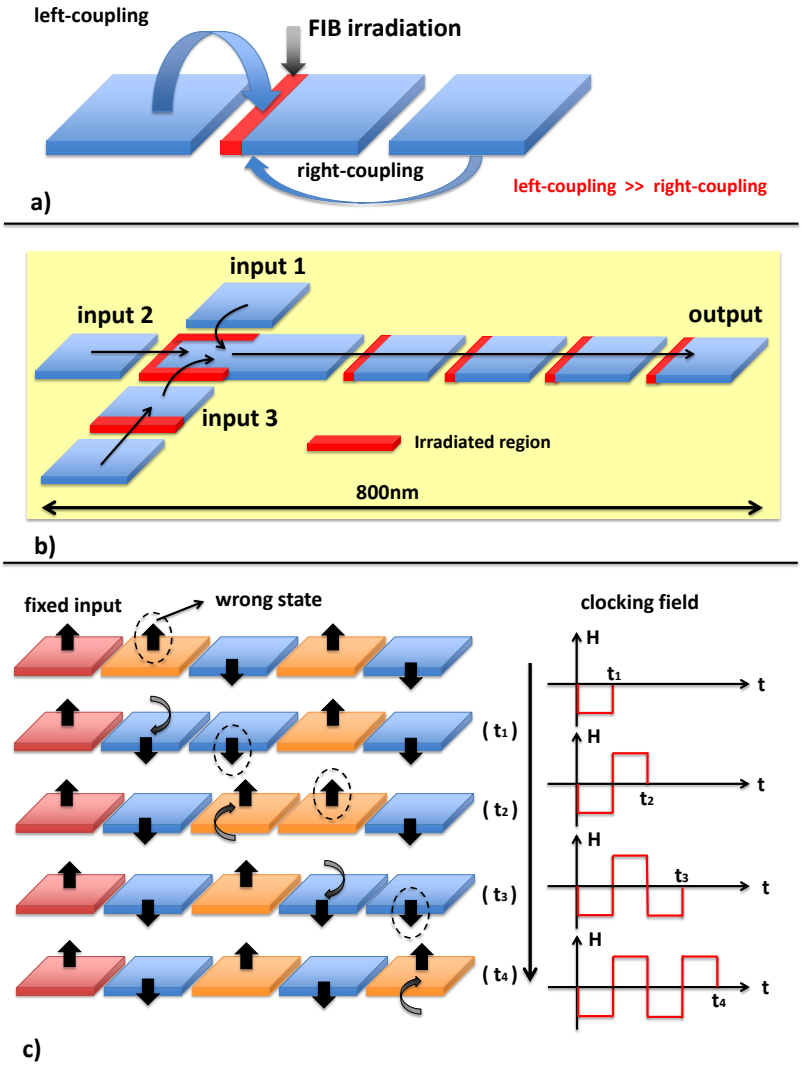

Figure 6.3. a) Non-reciprocal coupling of Co/Pt dots due to partial FIB irradiation. b) Partially irradiated majority gate and magnets chain. c) Error state is driven out by an osclliating field in a pipeline.

order and not mixed up during processing.

Our layout design of the pattern matching circuit is shown in Fig. 6.4, where the arrows indicate how the information propagates. Input data come into the structure from the bottom left and final output is read out from the top left. The pattern to be recognized is stored in dots marked with W_n and the neighboring dot is set to the opposite logic state. Both of these two dots are with hard magnetization and their state remains constant during the clocking process. The bottom left dot X_{in} in each PE is defined as the input dot, which receives incoming data

and the top right dot Y_{in} is the one, which receives response from the former PE. In our layout, the AND gate is implemented with a majority gate with a bias input (the top part in Fig. 6.4) and the XNOR gate (the bottom part in Fig. 6.4) is realized with three majority gates: two of them function as AND gates and the third one works as an OR gate. We optimized the number of dots in the XOR gate to improve the operating speed. Compared to the XOR gate in Fig. 5.6, this design saves more than 50% area.

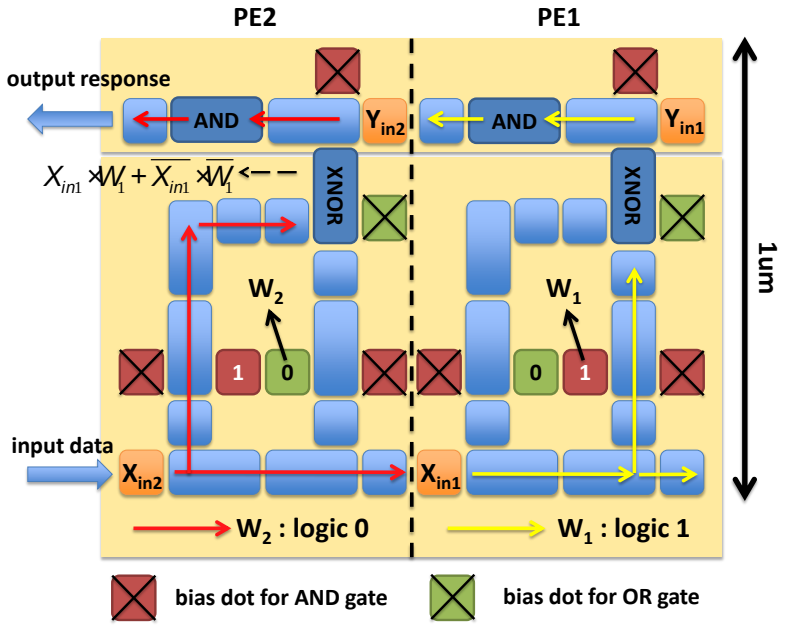

Figure 6.4. Topview of a 2-bit systolic pattern matcher built with Co/Pt nanomagnets. The arrows show the information flow in and between PEs.

In a SPM circuit, the time of receiving input, computing and generating output data has to be synchronized. The timing of these operations is sketched in Fig. 6.5. Since all the PEs share the same layout, the communication time and computing time in each block is a constant. In Co/Pt based NML, it is possible to adjust the time delay by increasing or decreasing the dot number or changing dot aspect ratios in the signal path, earning more freedom for layout design compared to Permalloy-based NML. Adding one dot increases 0.5 T_c extra delay. For the purpose of having the best signal flow synchronized in a systolic pattern matcher, signal connected to different ports of the gates should arrive simultaneously. Clearly, the length of

the signal path should be as short as possible to enhance the circuit performance.

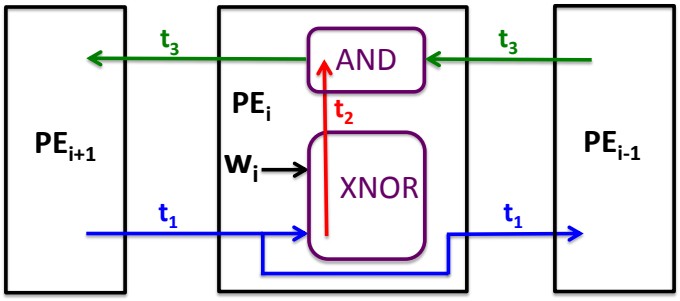

Figure 6.5. Time consuming during information process: t_1, t_2 and t_3 indicate the required time for receiving input, computing data and sending output respectively.

There are two signal paths from the input dot to the output dot in an XNOR gate. But one of the paths is 'shut down' when signal passes through the other one, depending on the logic state of pattern bit W in this PE. Illustrated in Fig. 6.4, if pattern bit W_i is at logic 0 state, taking into account that this majority gate is an AND gate (the bias dot is also at logic 0 state), the logic state of the other input dot is irrelevant for the output of AND gate: the right path is blocked and information only flows along the left path. Similarly, information only flows in the right path when the logic state of pattern bit is logic 1. With our design, neighboring PEs can be connected directly as shown in Fig. 6.4 so that PE to PE interconnection does not require additional dots. An n-bit SPM can be achieved by putting n PEs in a row next to each other.

The time interval between two adjacent bits should in principle be chosen as short as possible, while keeping the data flow in synchronization. In our simulation, we set the time interval to 4 T_c. As shown in Fig. 6.6, there are seven dots (two PEs) between the two adjacent bits X_1 and X_2. The arrows show the traveling trajectories of X_1 and X_2 within 5.5 T_c. After every 4 T_c, the Y response in the top chain steps forward one PE, and the final response comes out from the left end of the top chain after $n \times 4T_c$. If and only if all the pattern bits are matched one after another, the final response will be '1'.

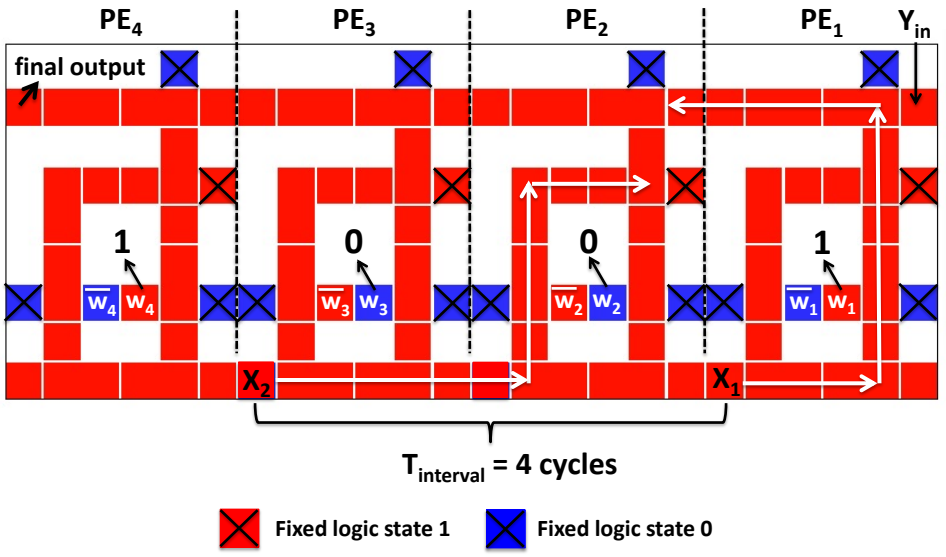

Figure 6.6. The two signal flow of two adjacent bits within the same time period.

6.6 Micromagnetic simulation on a 4-bit NML based systolic pattern matcher

We verified the work flow of a 4-bit NML based SPM using micromagnetic simulations. We made only very few simplifying assumptions similar to the ones discussed in [82]. We assumed zero temperature and 'ideal' magnetic films, i.e. uniform and constant magnetization parameters for the unpatterned, non-irradiated film. OOMMF [94] simulations with these assumptions were found to be in good agreement with experiments [80].

In order to provide the input stream tested SPM, we used a shift register, a chain of Co/Pt dots, which are initialized to a given pattern. This makes it unnecessary to apply localized fields in the OOMMF simulation.

The simulated layout is shown in Fig. 6.7. There are 24 dots in the shift register, and the magnetization states of the dots in the shift register step forward with the applied external oscillating field. Initially, the first bit X_1 situates at the input dot of PE_4 (the most left one). Correspondingly, the logic states of X_2, X_3 and X_4 are predefined in the shift register with a constant interval (shown in Fig. 6.7 (a)). We set X_1, X_2, X_3, X_4 to '1', '0', '0', '1'. The logic state of the dot Y_{in} (labeled in Fig. 6.7 (a)) is set to '1' to initialize the first AND operation of PE_1.

We also set fixed 4-bit pattern to '1', '0', '0', '1' for the test. Several snapshots from our simulation are given in Fig. 6.7. The external clocking field amplitude is $B_{\text{osc}} = 52$ mT, and the period of the oscillations is $T_c = 15$ ns.

In snapshot (f) of Fig. 6.7, logic 1 results as the output, indicating that W_1, W_2, W_3, W_4 is present in the input stream. We also verified that changing one of the four logic state of X_{in} data stream will result in a logic 0 as the final output, telling that the input stream is mismatched with W pattern. Thus, this 4-bit NML based SPM works properly. This work flow can be expanded to a N-bit pattern matcher. The only difference is the latency time, which is dependent on the number of PEs – n.

6.7 Performance evaluation for the nanomagnetic SPM

Extensive simulations indicated that the SPM circuit works without any error for a large number of inputs. This is remarkable since the design did not require careful optimization / tweaking of the material parameters, but we re-used building blocks from earlier work in Chapter 5 [82]. However, it remains to be addressed (1) how robust a large scale SPM made up with thousands of PEs would be in experiments and (2) how competitive this circuit could be with a functionally equivalent CMOS realization.

Robustness and sensitivity to switching field variations

The amplitude of B_{osc} is chosen in such a way, that it is able to switch a particular dot if and only if this dot is metastable with regard to its neighbors on the input side. In Chapter 5, we interpreted how one can choose the B_{osc}^{min} and B_{osc}^{max} parameters so that if B_{osc} satisfies $B_{\text{osc}}^{min} < B_{\text{osc}} < B_{\text{osc}}^{max}$, switching occurs correctly. The range for our design is $B_{\text{osc}}^{min} = 52$ mT and $B_{\text{osc}}^{max} = 57$ mT. In order to avoid errors, the $B_{\text{osc}}^{max} - B_{\text{osc}}^{min} = 5$ mT range should be larger than the switching field variations (caused by film inhomogeneities) and thermally induced switching field fluctuations. We expect that for the parameters used here, thermal

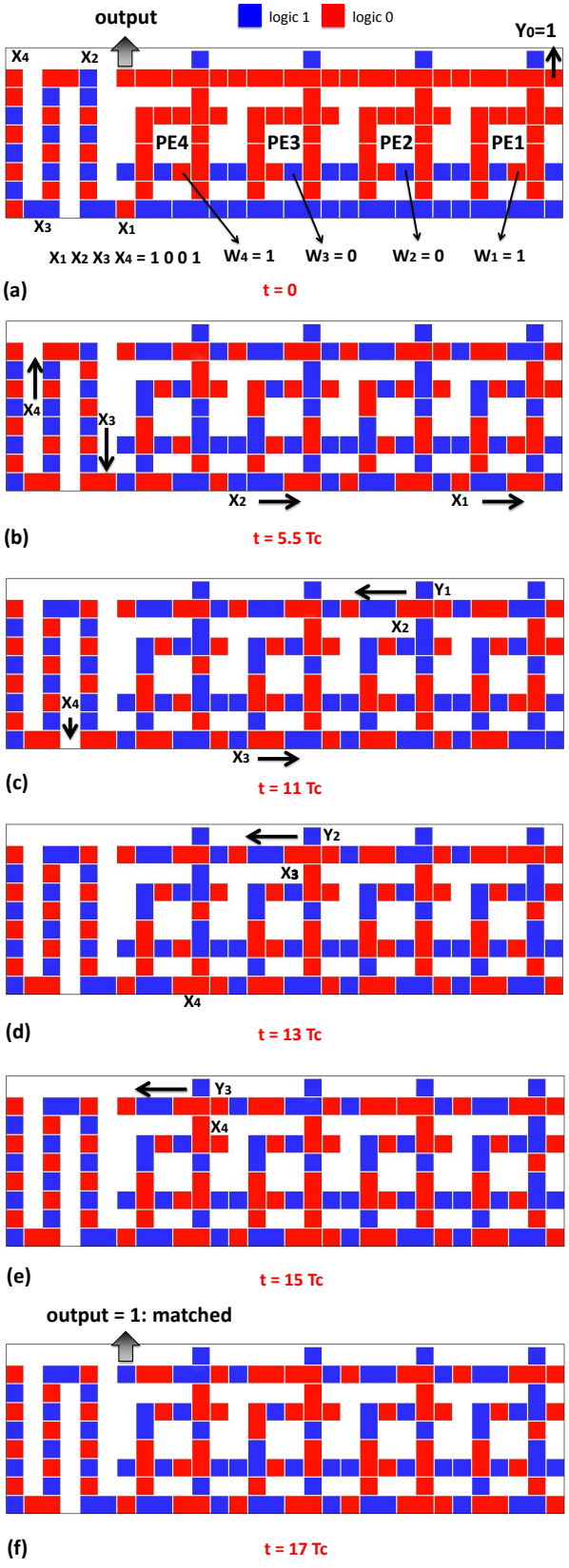

Figure 6.7. Snapshots showing information flow in a 4-bit systolic pattern matcher.

fluctuations will yield to errors, but our studies show further optimization of the design can eliminate those problems [125].

Power dissipation

At each switching event, an energy equivalent to the potential barrier separating the two states will be dissipated (hysteresis loss). This ΔE energy is in the range of 10^{-18} J (a few hundreds of $k_B T$ or a few eV) for the dots here. Assuming a 100 MHz clocking speed, this gives a nanowatt power dissipation per PE and n times as much for the dots of the entire architecture. This is a pessimistic estimate, since on average only 1/8 th of the dots in this structure is switching at any given clocking cycle.

Vast majority of the power will be actually dissipated by Joule heating of the wires (coils) that generate the clocking field. The presented structures require $B_{\rm osc} = 52 - 57$ mT, but preliminary simulations indicate that that switching field of the dots can be reduced to $B_c = 10 - 15$ mT, bringing $B_{\rm osc}$ also in this range, similar to the field range calculated for permalloy-based NML devices [126]. Since Co/Pt devices require homogeneous clocking fields, these are more effectively generated by than the localized clocking fields required by Permalloy-based NML.

Operation speed

Switching of Co/Pt nanomagnets is a two-step process, (1) nucleation and growth of a domain wall (2) propagation of the wall and switching of the entire volume of the ferromagnetic dot. The simulations indicate that both processes take $2 - 3$ nanoseconds to complete. A dynamics simulation showing the dot switching is shown in Fig. 6.8. This results in $T_c = 5 - 10$ns, but making the dots smaller may reduce clock cycles to $T_c = 2 - 3$ ns range. There is clearly a trade-off between switching speed and low-power operations, as switching is generally faster using larger $B_{\rm osc}$ values. Simulation on few-dot systems indicate that clock frequencies above 100 MHz and $B_{\rm osc} < 15$ mT is achievable simultaneously.

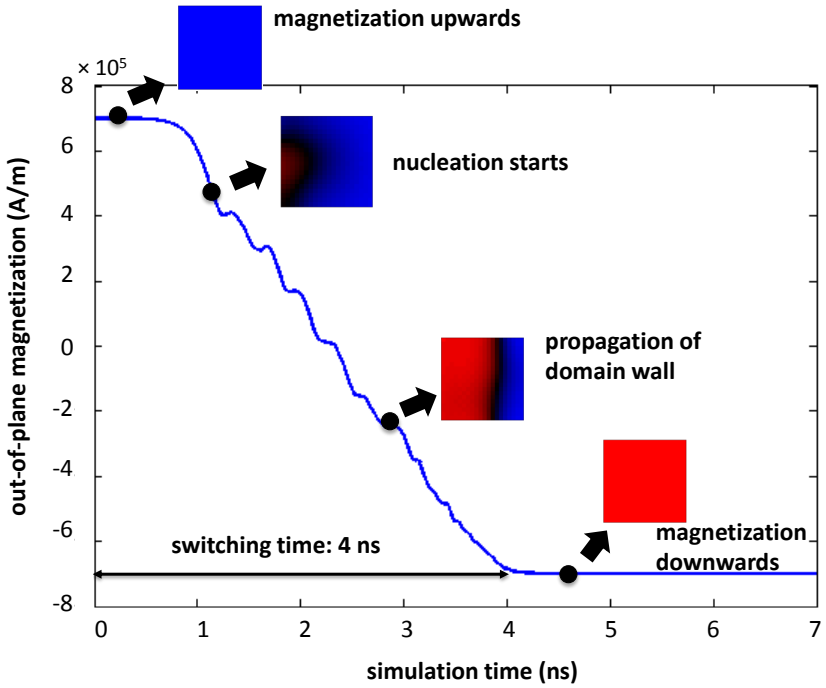

Figure 6.8. The reversal of a partially irradiated nanomagnet.

Benchmarking against CMOS

Of interest is how oNML hardware compares to CMOS equivalents given initial clock and timing requirements, and potential improvements to the above projections. In CMOS, common hardware-based solutions for finding patterns in data leverage reprogrammable hardware or memory-based finite state machines. It would be difficult to make fair comparisons to oNML-based solutions given the extraneous overheads of memory references, etc. As such, for the purpose of comparison, we chose to model a CMOS-based systolic array – where a PE like that shown in Fig. 6.2 was considered in SPICE using ASU predictive models. Projections for energy and delay for a single PE, were made at four different technology nodes (45 nm, 32 nm, 22 nm, and 15 nm), and at different voltages.

In the oNML systolic array, a new pattern sequence would be tested every 60 ns (i.e. $4\ T_c = 4 \times 15$ ns). However, this number could be halved with interleaved data streams. Also, T_c could be reduced to just $2 - 3$ ns. The data of switching energy of square dots and elongated dots used in gates and chains are listed in

Table 6.1. We estimate that the energy associated with magnet switching events during the re-evaluation of a single PE is ∼45 aJ.

Regarding clock energy, we anticipate using microcoils to generate out-of-plane clocking fields [127]. As such, the energy associated with the clock will be a function of: (i) the area of a given PE amortized over the controllable area of a microcoil (the area of a PE could be ∼1 μm^2, while microcoil area could be $\geq 0.01 - 1$ mm^2, (ii) the quality factor Q – a high Q inductor may be used in an LC tank circuit, and a large percentage of the clock-field generating energy can be recycled for the subsequent clock cycles, and (iii) clocking pulse requirements (simulations above suggest field requirements of ∼52 mT, but switching fields of ∼10 mT could be possible – e.g. with Co/Ni layers). However, initial oNML projections for a PM PE without clock overhead are still ∼100X lower than CMOS equivalents at iso-performance.

TABLE 6.1. ENERGY CONSUMPTION OF PARTIALLY IRRADIATED CO/PT DOTS

	dot size (nm^2)	switching field (mT)	power dissipation per switching (J)
in the simulation	100×100	70	2.94×10^{-18}
	210×100	67	5.91×10^{-18}
to be optimized	100×100	10	4.2×10^{-19}
	210×100	10	8.8×10^{-19}

6.8 Summary

While NML is widely considered to be one of the front-runners for post-CMOS nanoscale architectures, so far mostly 'toy circuits' (gates and adders) have been studied experimentally and in simulations. We investigated the possibility of building larger-scale computing devices from out-of-plane NML and picked a particular application (systolic pattern matching circuitry), which is well-suited for nanoscale implementations, and used physics-level micromagnetic simulations to design an SPM circuit that is, in principle, scalable to arbitrary number of dots. The de-

sign of this systolic architecture for NML makes the first step toward large-scale devices.

We studied NML built from Co/Pt dots with FIB irradiation, since we have experimentally verified models for this system. The presented design methods and architectures are valid for Co/Ni and other perpendicular media, whose performance characteristics could be even better.

Comparison to CMOS circuitry indicates that perpendicular NML technology could be very well competitive to CMOS technology, especially for special-purpose applications, where data throughput, low power and robust operation is more critical than fast, general-purpose computing.

CHAPTER 7

CLOCKING NML WITH DOMAIN WALL CONDUCTORS

7.1 To date clocking structure for NML

It is well established that a clocking structure is indispensable in NML devices [39]. An ideal clocking structure should posses the following two main features:

1. The external field generated from clocking structure is able to eliminate the metastable states and drive the dots to computational ground state.

2. This clocking scheme should dissipate as little power as possible so that to maintain power-efficient.

During the last decade, lots of efforts have been made in NML study in order to fulfill these two requisites. In earlier work, experiments verified that a homogeneous clocking field can hardly drive a large number of Permalloy dots perfectly in NML. Local clocking fields covering relatively small area (a few gates) are required to ensure the functionality. In [128], a computational study proved that the idea of local clocking also works in Co/Pt based oNML. The local clocking structure can be realized by current carrying metal wires buried underneath the nanomagnets. However, the calculated current density for both cases turned out to be rather high in order to provide a sufficient magnetic field to drive the dots. These power-hungry current wires bring about lots of heat. Consequently, how to dissipate the heat becomes another troublesome issue. Later on, the idea of cladding the wires with soft magnetic materials [41] and filling enhanced permeability dielectric among the dots has been proposed, which could reduce the current density to an

acceptable level, though it is still not yet experimentally demonstrated how large power reduction can be achieved.

The proposal of partially irradiated dots makes it feasible in oNML that clocking the dots with just one globally homogeneous out-of-plane field. Burying wires are unnecessary in the fabrication. This clocking structure should generate an oscillating field with one prerequisite that its amplitude should be in a certain margin, in which the clocking field can wipe out the metastable states but not disturb the ground state. Operating at the up limit high frequency of a few hundreds MHz, the power required to generate this oscillating field is dominant over the power dissipated from the nanomagnets. Aiming to lower the overhead energy resulted from clocking structure, we verified with our computational study that with a proper FIB irradiation, it is possible to bring down this margin to below 20 millitesla. However, experimental confirmation is still on the way.

7.2 New clocking scheme: clocking NML with domain wall conductors

One of the most promising features of NML is the potentially low power dissipation. However, as we discussed earlier, how to clock the the magnets in the most efficient way is still an open question. The homogeneous external field required in oNML could significantly reduce the difficulty in fabricating the clocking structure and also the power consumption, but still the mount of power needed to generate the clock signal is in several orders over the power cost from the switchings of nanomagnets.

Here we propose a new clock scheme which may yield to a 'power-friendly' clock structure. Instead of generating the clocking field from magnet coils or current pulses, this idea is to utilize the stray field from a domain wall to drive the switching of nanomagnets [129]. In magnetic domain walls, the magnetization changes abruptly within a few nanometer wall width, creating strong, localized magnetic fields. More details about domain wall theory, please refer to Chapter 3. Propagating domain wall can be done just by a weak (a few mT) in-plane external

fields, which concentrate slowly varying homogeneous magnetic fields into strong, localized and quickly propagating field distributions.

The interaction between Permalloy nanomagnets and Permalloy domain wall was already demonstrated experimentally and theoretically [130] [131], where the nanomagnetic dots provide a pinning field for the domain walls, but the domain walls don't have back-influence on the magnetization of the dots. Here we reverse the interaction with a different geometry. We apply the stray-field from a domain wall to affect the magnetization of Co/Pt multilayer dots.

The designed structure is demonstrated in Fig. 7.1, where a Permalloy domain wall conductor (DWC) is placed underneath a chain of Co/Pt multilayer nanomagnets. The domain wall produces a strong in-plane field B_x and out-of-plane field B_z. The stray field interacts with Co/Pt dots. It is dependent on the size of the domain wall and the vertical distance between the two layers that to which degree the field influences the switching behavior of Co/Pt dots. By adjusting the interactions, one propagating domain wall acts as the clocking signal which drives the dots to the expected states.

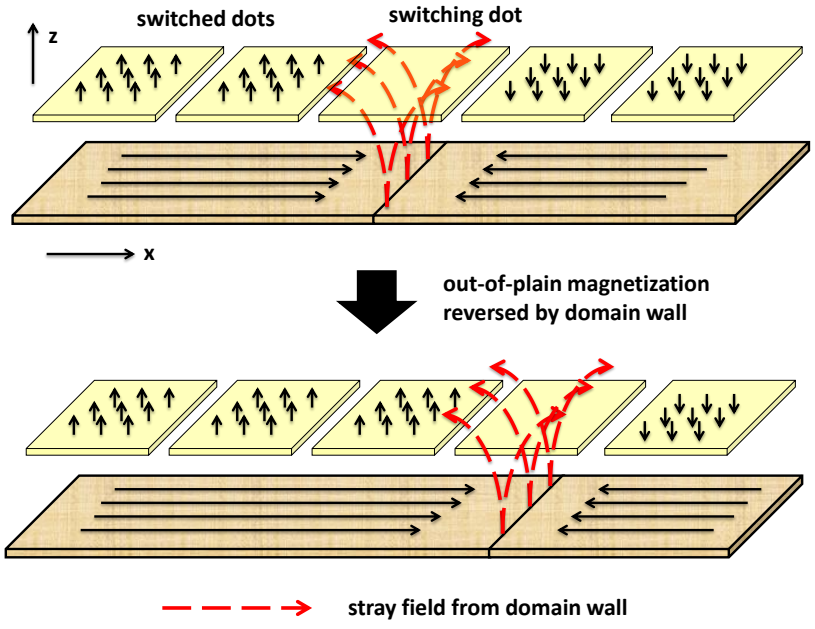

Figure 7.1. Schematics of the Co/Pt dots and underlying Permalloy domain wall conductor system.

This system offers the advantage that the only power-consuming part is from the in-plane external field, which pushes the domain wall forward and is much weaker compared to the out-of-plane field that straightforwardly switches the dots. This further reduces the power dissipation in NML devices. The movement of the domain wall is insensitive to the out-of-plane magnetic field B_z, which helps to avoid a strong back-influence from the Co/Pt dots. Another benefit of this three-dimensional structure is that the Co/Pt dots can be located as close as possible to Permalloy DWC. With few nanometers of vertical distance, the field of the domain wall can have strong interaction reaching the entire volume of the dots.

The domain wall motion is extensively studied in [13] [15] [17] [132] [133] [134]. We verified that the speed of the domain wall can be as high as a few hundreds of meters per second, which ensures that the circuits can operate at high frequency. This frequency could potentially be several times higher than the frequency limit of globally oscillating external field applied to partially irradiated dots.

The most challenging part of this three-dimensional clock scheme is how to generate the domain wall and how well we can control its motion. In order to answer these questions, we implemented experiments and also three dimensional simulations for further investigations. The great efforts in experiments were made by Josef Kiermaier from Lehrstuhl für Technische Elektonik.

7.3 Permalloy domain wall conductor

A domain wall conductor is a nano-scale structure, in which domain walls are created and propagated. In our case, it is made of a Permalloy stripe with a stripe width below the single domain size. In order to generate a domain wall more efficiently, the DWC can be 'L' shaped, as presented in [19]. With an external in-plane field at 45 degree to the long arm, a domain wall can be created at the corner of the conductor, which can be afterwards driven out by changing the direction of the external field along the arm.

The strength requirement of the external field can be further reduced through

the approach of using a DWC with a large pad on one end[130] [135]. With this structure, a domain wall can be generated at a much lower field inside the pad and then driven out from the pad to the thin stripe.

Here a demonstration of obtaining a domain wall in a DWC is shown via simulations. The simulated structure and material parameters are given in Fig. 7.2.

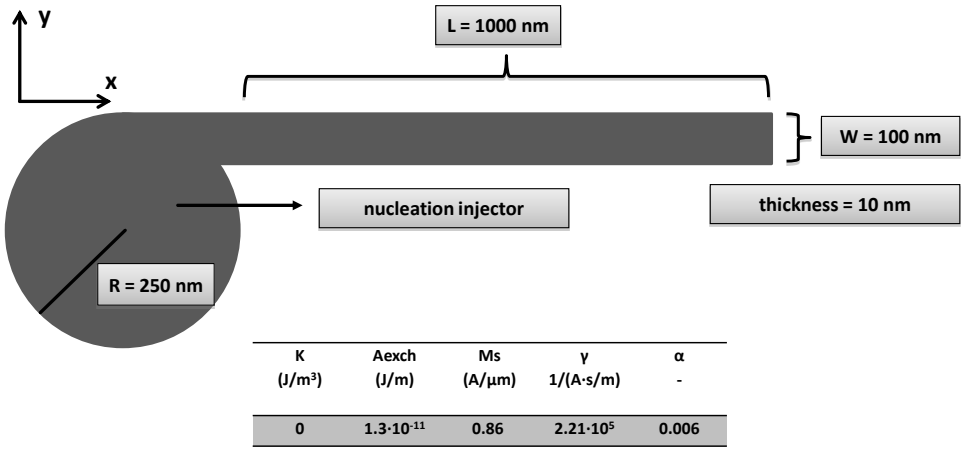

K (J/m^3)	Aexch (J/m)	Ms (A/μm)	γ $1/(A \cdot s/m)$	α -
0	$1.3 \cdot 10^{-11}$	0.86	$2.21 \cdot 10^5$	0.006

Figure 7.2. The geometry and parameters of the DWC used in simulation.

Initially the Permalloy is magnetized in negative x direction. An external in-plane field in positive x direction is then applied to nucleate the domain wall in the pad and drive it in the long stripe. It is observed that nucleation starts at a very low field (∼1 mT, shown in snapshot (a) in Fig. 7.3), but a stronger field is required in order to expand the nucleation (see snapshot (b) in Fig. 7.3), overcome the energy barrier at the left end of the stripe and drive it out from the pad (snapshot (c) in Fig. 7.3). In this case, it is about 20 mT that is able to push the domain wall into the long stripe. Note, with a larger pad, expansion of nucleation becomes easy since thereby the demagnetizing field is larger. However, the minimum in-plane field to push the domain wall in the stripe is dependent on the material properties and the geometry of the stripe. Assuming the thickness is a constant, in principle, a larger width can reduce the minimum value because the energy barrier at the connecting part between the pad and the stripe gets lower.

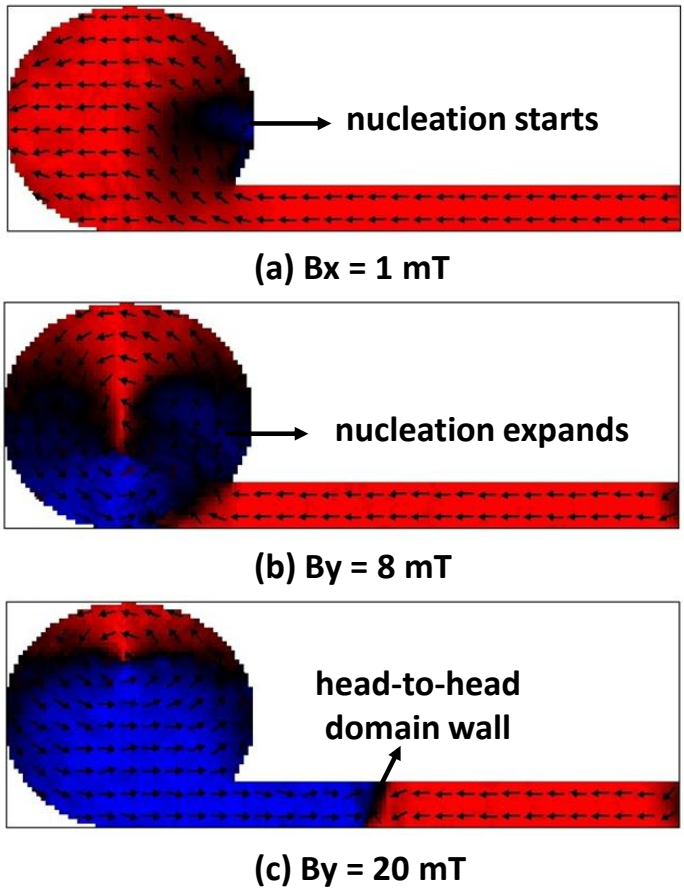

Figure 7.3. Snapshots from OOMMF showing the evolution of generating a domain wall in a DWC.

It is already experimentally and theoretically verified the large pad is always the source of the domain wall [130]. However, it is hard to tell from which end the domain walls start from the DWCs without any pad (e.g. (a) and (c) which will be illustrated later in Fig. 7.5). Our micromagnetic simulations proved that a domain wall is generated randomly from one of the two poles in a symmetrical DWC. The nucleation starts from either of the two ends, or even from both ends simultaneously. It is of great importance where the domain wall starts because this decides the type of the domain wall (head-to-head or tail-to-tail) and the propagating direction. The stray field of a head-to-head wall can be taken as mirrored of a tail-to-tail wall, as sketched in Fig. 7.4. Used for clocking, the type of domain wall has to be under control in order to offer a stable clocking field with a proper amplitude in the right direction.

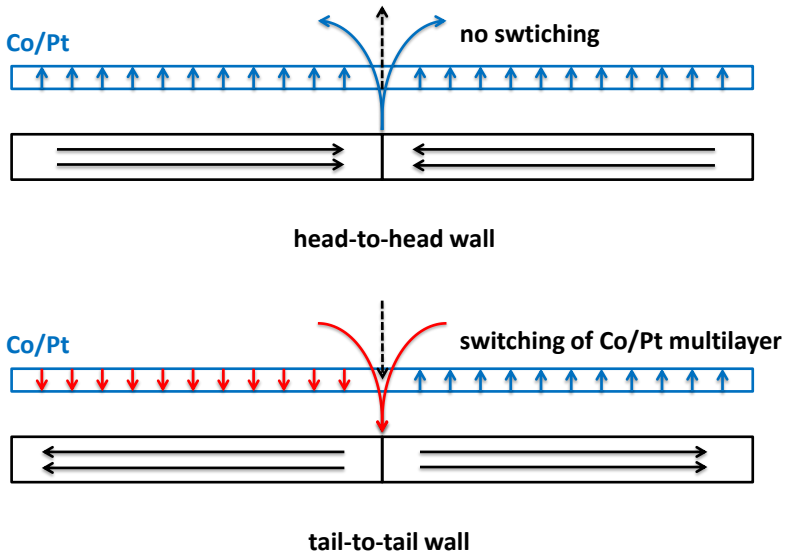

Figure 7.4. The stray fields of a head-to-head domain wall and a tail-to-tail domain wall.

Our fabricated DWCs are shown in Fig. 7.5, where the middle one is with a large pad at the left end. In experiments, the three DWCs are magnetized by an in-plane field in x-direction. Afterwards the external field is applied in -x direction, reversing the magnetic poles of the DWCs. The reversal of the poles results in domain wall creation and propagation. Though the DWC (a) and (c) are without large pads, as the first-step investigation on the interaction between a DWC and the Co/Pt film, they are still quite helpful.

7.4 Interaction between domain wall conductors and Co/Pt multilayer films

In oNML, domain wall conductors are not only proposed in the usage of clocking structure. In [136], a DWC is demonstrated to provide a bias field for one Co/Pt dot. This strong bias field can 'lock' the magnetization of Co/Pt dot to one logic state. Hence, this Co/Pt dot can be potentially used in an input structure in oNML. By reversing the two poles of a DWC, the bias field changes its sign, which makes the input programmable. This can turn an OR gate to an AND gate and vice verse.

Our experimental layout is shown in Fig. 7.6 (a). The Permalloy DWCs are

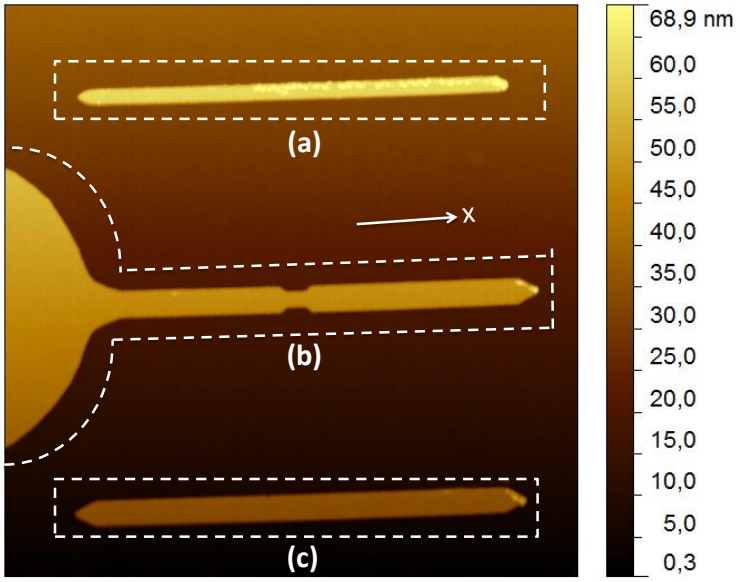

Figure 7.5. The golden parts in MFM image display the fabricated domain wall conductors. The width for stripe (a) is 140 nm; for (b) and (c) are 240 nm [137].

buried underneath and appear as gray bars. Co/Pt nanomagnets are placed right on top of both ends of DWCs separated by a thin dielectric (a few nanometers). The center part of each dot is FIB-irradiated to lower the coercivity and make the switching easier. Instead of experiencing interaction from the domain wall, in this structure the interaction is produced from the two poles.

In experiments, the DWCs are magnetized by weak easy-axis in-plane fields. Subsequently, the Co/Pt dots are driven to ground state by applying an oscillating out-of-plane field with decreasing amplitude. Note that this out-of-plane field won't affect the already magnetized DWCs. The stray field from the two poles is sufficiently strong to decide the magnetization of the Co/Pt nanomagnets, verified by the MFM phase image shown in Fig. 7.6 (b), where all 15 pairs of Co/Pt dots are finally magnetized to the same state, i.e. the left one with magnetization pointing upwards and the right one downwards. This result proved that top-bottom layer coupling could be considered as a new design handle in NML [138].

Based on the fabricated DWCs in Fig. 7.5, we further deposit 5 nm dielectric film as a separation layer and afterwards 10 nm thick Co/Pt multilayer film. The

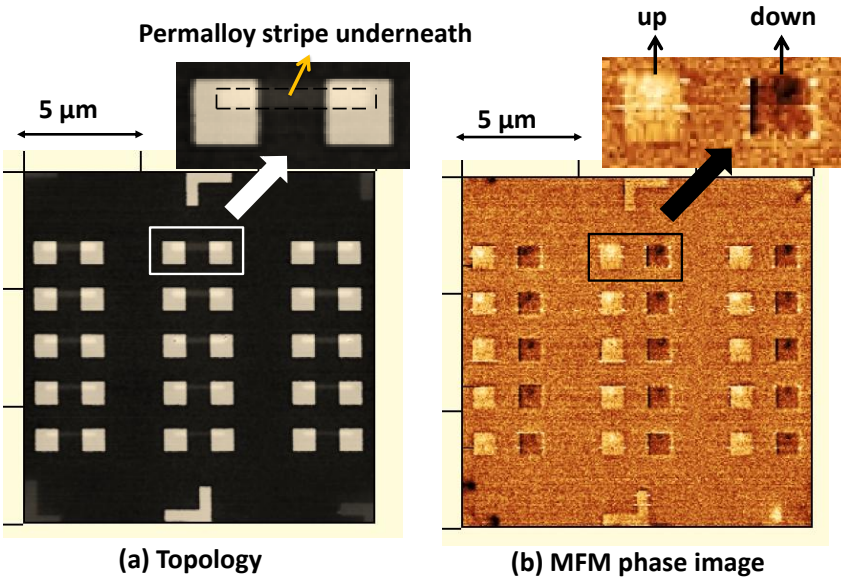

Figure 7.6. This experiment demonstrates strong interaction exists between Permalloy bars and Co/Pt dots: (a) the topology of fabricated structure and (b) the demagnetized state indicating the strong interaction [136] [138].

geometry is sketched in Fig. 7.7.

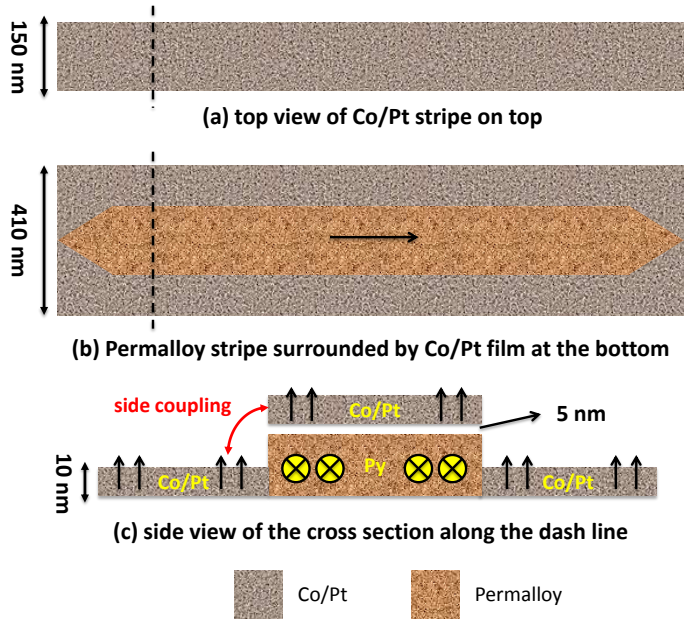

Figure 7.7. Top view and side view of the fabricated structure.

The structure was first saturated by a 700 mT out-of-plane field with an additional x-component of 80 mT. Then it was relaxed by reducing the external magnetic field simultaneously to zero. After relaxation, it was observed at some

parts of the Co/Pt film on top of DWCs, the magnetization flipped over. The MFM phase image is revealed in Fig. 7.8 (a). However, not the entire magnetization on top of the DWCs are switched. The top area split into multiple domains. One possible explanation for this phenomenon is due to the side effect caused by the deposited Co/Pt material surrounding the DWCs (at the bottom layer). The coupling between top Co/Pt layer and bottom Co/Pt layer may lead to the splitting (as shown in Fig. 7.7). This side effect can be removed in future experiments with new fabrication process.

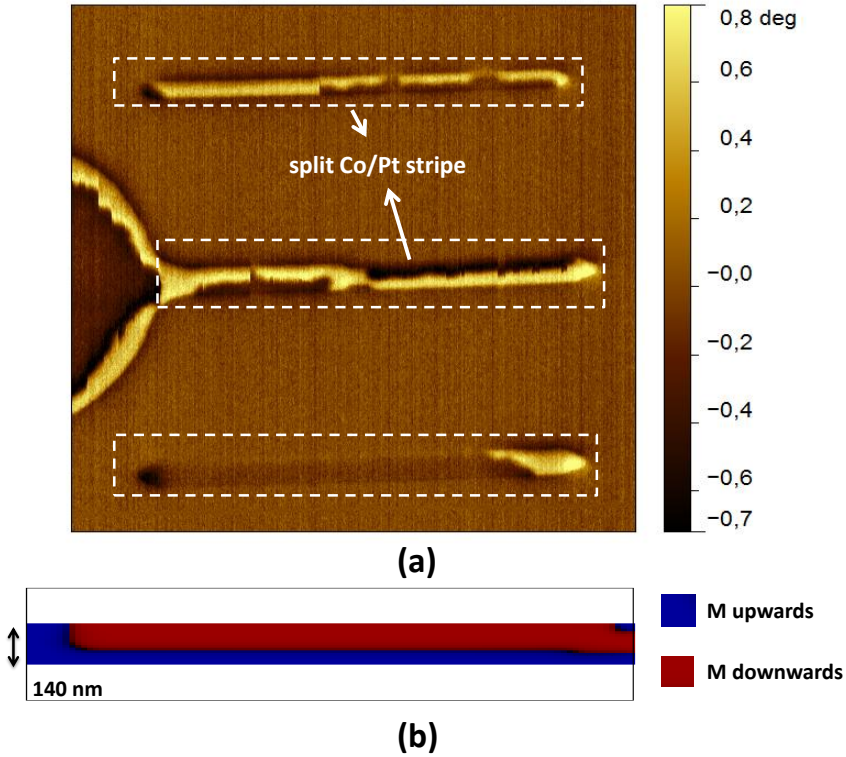

Figure 7.8. (a) MFM image shows Co/Pt film on top of the DWCs turns multiple-domain, suggesting the interaction between the DWC and the Co/Pt multilayer film [137]. (b) Split Co/Pt film from our simulation.

Another reason could be due to the geometry of the DWCs. The domain wall dynamics in thin films is well established in [135] [139] [140] [141] [142] [143]. It is known that the formation and propagation of the domain wall depend on the width and thickness of the DWCs. As the thickness decreases, the domain wall transits from a Bloch wall to an Néel wall [141]. According to domain theory, as

the width increases, the state of being multiple-domains become favorable. We have implemented computation study and looked into the wall dynamics in DWCs. To be consistent with the fabricated structure, the thickness was chosen as 10 nm. We varied the width from 100 nm to 200 nm.

Firstly, we chose a width of 140 nm, which is the same size of DWC (a) in Fig. 7.5. We simulated the same process as done in experiment. After relaxation, the final pattern agreed well with what we observed in Fig. 7.8 (a): the Co/Pt film on top of DWC partially flipped over. Further more, in simulation we applied an in-plane field to reverse the two poles of this DWC. The nucleation started randomly from one end and then the domain wall propagated to the other end. The reversal of the DWC led to another nucleation on the top Co/Pt layer. The snapshots in Fig. 7.9 indicate and verify the strong interaction between the two layers. The reversal of the Co/Pt layer follows the motion of domain wall beneath. However, as the DWC is completely reversed, a small portion of Co/Pt film at the edge remains un-switched and the Co/Pt ends at a split state.

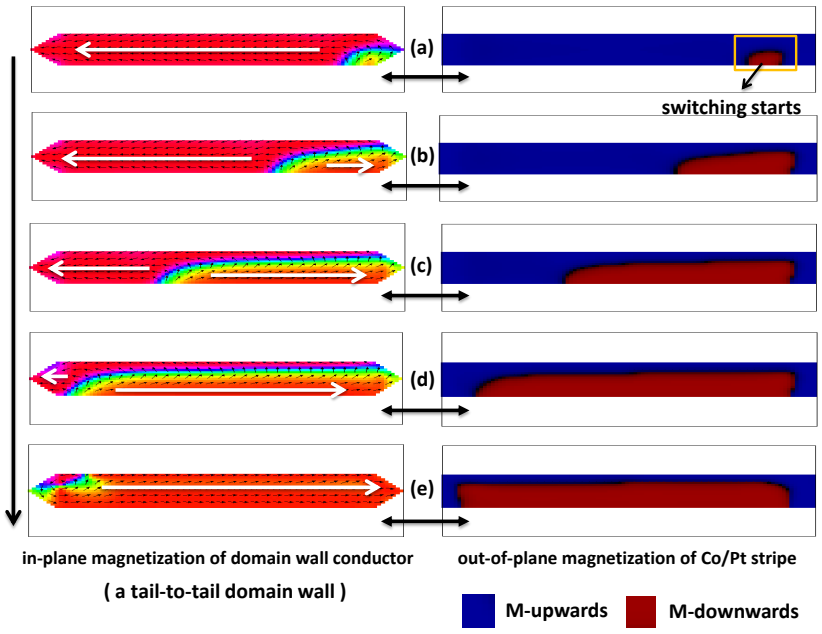

Figure 7.9. Snapshots from OOMMF showing the interaction between the DWC and Co/Pt film: the nucleation of Co/Pt film follows the motion of the domain wall.

During the simulation, we also observed that:

1. Considering random parameter variations (e.g. shape variation, M_s variation, etc.) in simulation, the nucleation starts from either of the two poles randomly, which was consistent with our former theoretical description.

2. In the simulations where the DWCs are thicker, the domain wall appeared a vortex pattern and the wall was transforming all the way during its propagation. This very unstable domain wall generated a time-and-spatial varying inhomogeneous stray field. This complicated behavior increases the difficulty and uncertainties in our study.

To conclude, we have experimentally and computationally verified the strong interlayer interaction. These observations can serve as hints for NML-clocking design. In the next section, we will take advantage of these results.

7.5 Computational verification of clocking field-coupled Co/Pt nanomagnets with domain walls

It has been proved that the stray-field from the two poles of the DWCs and the domain walls in DWCs can reverse the magnetization in Co/Pt films. However, to utilize DWCs to control the ordering of Co/Pt dots is more challenging. In order to realize the ideal clocking with just a propagating domain wall, the following restrictions must be considered:

1. The stray field from the domain wall needs to be sufficiently strong so as to drive the dots switching. Yet it is not enough because the clocking field should lie in a certain range. If and only if the clocking field is in this proper range, the antiferromagnetic ordering can be achieved. Otherwise the clocking field may either disturb the already aligned ordering (too strong) or make no influence at all (too weak).

2. During the wall's propagation, the shape of the wall should be as stable as possible and the stray field should be at least as homogeneous as possible, acting as a steady-going external field.

3. A domain wall with fast speed can increase the operating performance of NML circuits. It is expected to obtain domain walls with a fast speed, which should, in the mean while, have plenty of interaction with each dot as they pass by.

Condition 1 can be fulfilled by adjusting the vertical distance between the two layers or varying the thickness of the DWC. However, the layer thickness together with width plays an decisive role in the wall type [141] [142]. As the thickness decreases, the domain wall transforms from a Bloch wall to an Néel wall and the shape changes from a 'C' shape to a vortex pattern and in the end to a transverse form [141]. In Fig 7.10 (a), it is presented that a vortex-shaped domain wall occurs in a DWC with a relatively large width (200 nm). In view of condition 2, this vortex-shaped domain wall should be avoided by mean of further reducing the width. The narrower DWCs yield to a transverse domain wall. The comparison is made in Fig. 7.10 (b), where the thickness is set to 10 nm. Simulations confirm that with a width of 100 nm, a transverse wall is created and maintains its form during the whole propagation in this DWC.

With this DWC width, we implemented simulations on the whole structure together with Co/Pt dots. This structure is illustrated in Fig. 7.11. 200 nm $\times$ 200 nm 5 ML Co/Pt are placed in a row right on top of the 100 nm wide Permalloy DWC. These dots are partially irradiated on the left side (20 nm wide) so that (1) the switching field is significantly reduces and (2) uni-direction information flow is ensured. The gap from dot to dot is 20 nm.

In the simulation, the same approach as described in Section 7.3 is applied to generate a domain wall. With this geometry, the average stray field distribution from the transverse domain wall during the whole propagation is plot in Fig. 7.12.

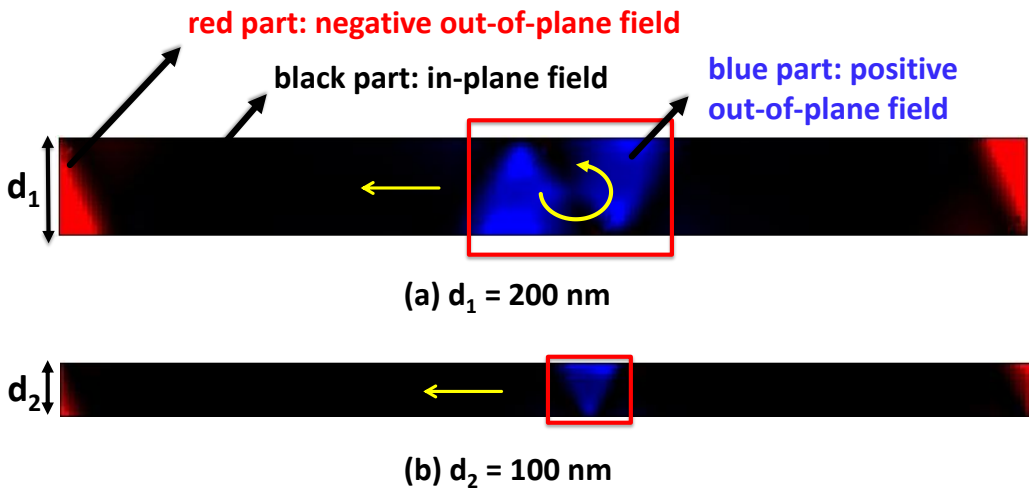

Figure 7.10. Different wall forms occur in DWCs with different layer widths: (a) a vortex-shaped domain wall and (b) a transverse domain wall. The vortex-shaped domain wall also spins during the propagation; however, the transverse domain wall maintains a steady form.

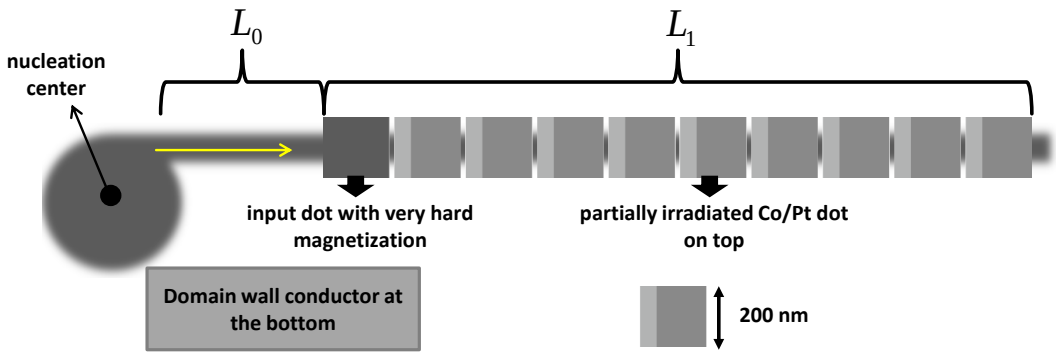

Figure 7.11. The three-dimensional structure shows a chain of Co/Pt dots clocked by a DWC.

This field distribution is captured in a 200 nm $\times$ 100 nm rectangular area, with the wall locating in the middle of the length. As one can see, this distribution is not uniform. The field at one edge ($y = 100$ in Fig. 7.12) is highest (B_{peak} with the coordinate ($x = 0$; $y = 100$) and it goes down from this edge to the opposite one ($y = 0$)) The field-distribution of this moving domain wall along the propagation is actually quite stable and here we simply assume there is no variation of this distribution and we directly take the average value B_{peak} and B_{half} (coordinate: $x = 0$; $y = 50$) for further discussion.

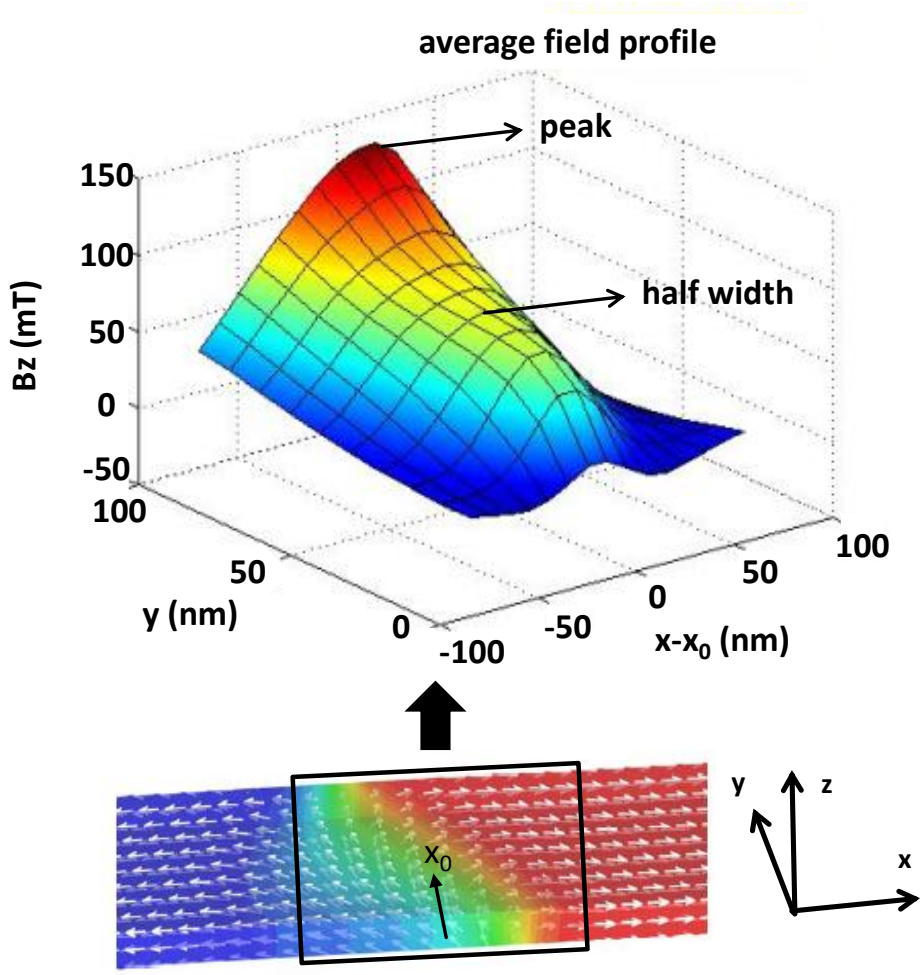

Figure 7.12. The average field distribution over a 200 nm × 100 nm area with a vertical distance of 15 nm, where we assume the domain wall locates at the middle length (x_0).

In this case, B_{peak} is several tens of milltesla larger than B_{half}. However, B_{peak} only acts in the small red area, which is not sufficient to switch the dot even this peak value is larger than the coercivity of the dots. Here we take B_{half} as the reference value, which makes more sense with the simplification that B_{half} acts as the mean value of the clocking field.

Since B_{half} is dependent on the vertical distance from the DWC and the DWC thickness, we could tune these the two parameters in order to get a proper clocking field. Fig. 7.13 shows the dependency of B_{half}.

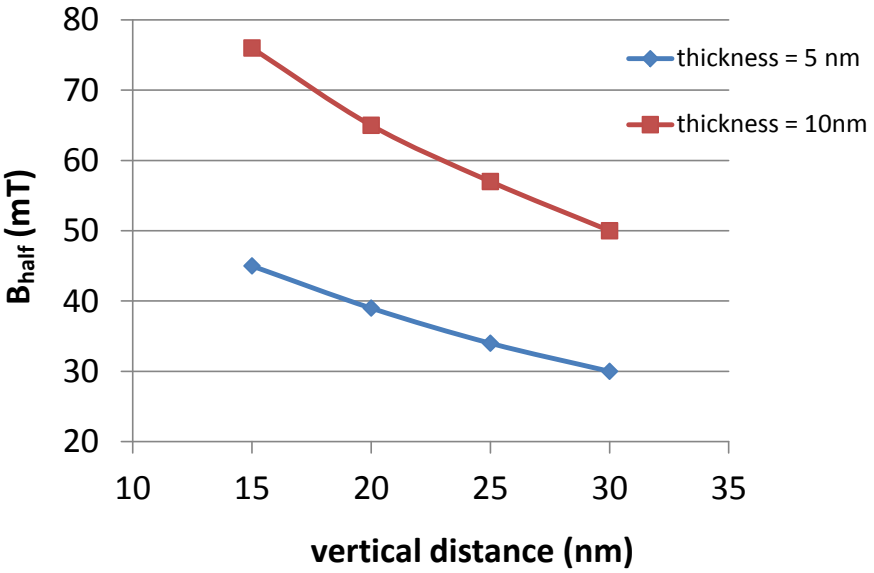

Figure 7.13. B_{half} vs. distance at different thicknesses.

With the DWC layer thickness of 10 nm and a vertical distance of 25 nm, B_{half} equals to 56 mT, which lies in the working margin of these 200 nm $\times$ 200 nm dot chain. Our simulations verified this running domain wall can successfully clock the dots to the antiferromagnetic manner. Some snapshots in our simulations are exhibited in Fig. 7.14. These snapshots show the out-of-plane magnetic field in a 4-dot chain (a) and 10-dot chain (b). Initially the input dot (the leftmost one) is with very high coercivity and magnetized upwards, and all the other dots are magnetized to the opposite direction. The domain wall field is in the positive direction perpendicular to the film plane. With an in-plane field of 20 mT as the driving force in the x-direction, this domain wall propagates from left to right and switches every second dot in the chain. In the end, the 'up-down-up-down $\cdots$' ordering is reached in both cases.

The previous case is a relatively simple one because all the dots except the input are magnetized to the same direction. With just one 'domain wall pulse', the frustration-free ordering can be realized. We also proved that even frustrations can be cleared out of the chain with multiple 'domain wall pulses'. However, the applied in-plane field need to oscillate from 20 mT to -20 mT in order to produce

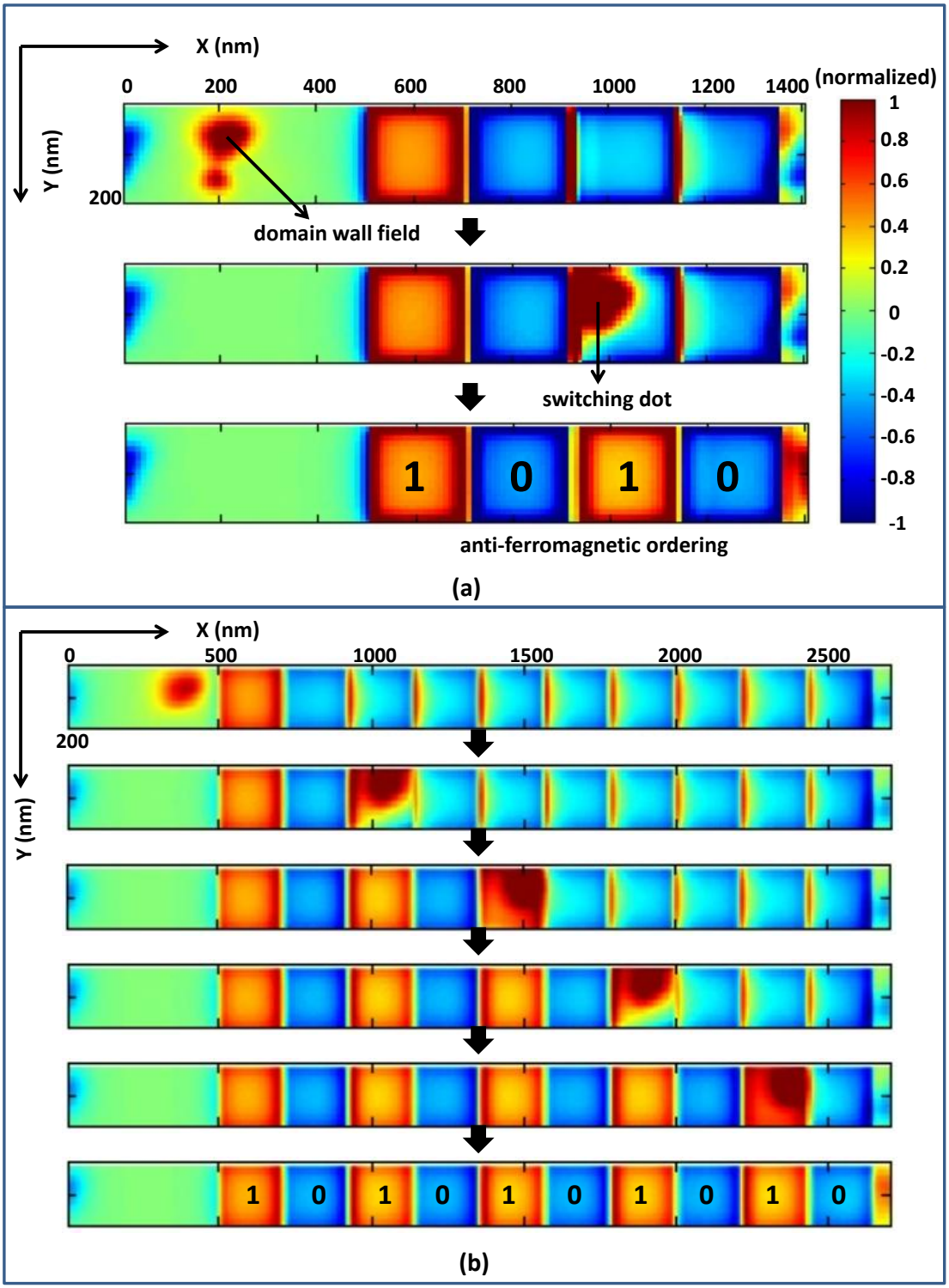

Figure 7.14. Simulation snapshots: (a) A four-dot chain and (b) a ten-dot chain are driven to the computational ground state by the domain wall.

alternant appearance of head-to-head wall and tail-to-tail wall. The details are illustrated in Fig. 7.15.

It is not difficult to find the analogy between these 'domain wall pulses' and the homogeneous out-of-plane field introduced in Chapter 5, when used as the clocking in NML. Both of these two approaches need an oscillating field. Here the oscillating field is in-plane. It doesn't directly influence the states of Co/Pt dots, but controls the domain wall field. In other words, we could consider this oscillating field as an indirect clocking field. While in Chapter 5, the oscillating field directly clock the dots. Another similarity between the two approaches is that the error states are pushed forward two dots after each oscillating cycle.

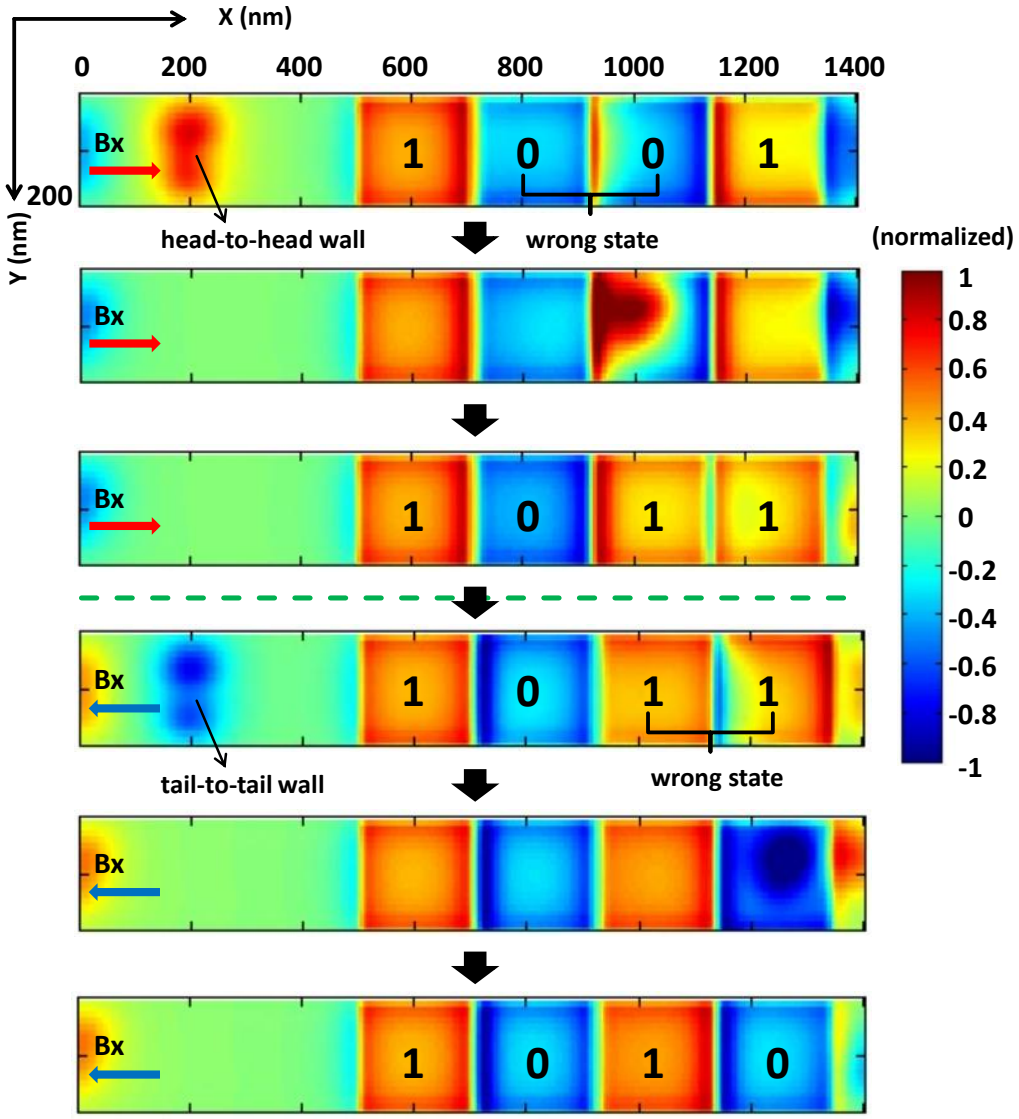

Figure 7.15. The approach to eliminate the parallel state with domain wall fields.

7.6 Summary

In this chapter, we proposed an new clocking scheme, where the domain wall field is employed to clock Co/Pt dots. It could provide us an more power-efficient clocking structure. We have experimentally demonstrated the strong interaction between the domain wall and Co/Pt films and dots, and verified the feasibility through physics-based simulations.

Rely on our simulation results, with a proper geometry, it has been proved that an in-plane oscillating field is sufficient to manipulate the motion of the domain wall in the DWC, and the stray field of the domain wall can switch the Co/Pt dots correctly. The amplitude of this in-plane field was 20 mT, which is already much lower compared to that of the out-of-plane field in Chapter 5 (above 50 mT). Nevertheless, we believe there is still plenty of room to improve the clocking efficiency. The threshold value of in-plane field to drive the domain wall can be further reduced by adjusting the geometry (the width and thickness) of the DWC or using new materials. Consequently, the threshold can be down to few mT, which drastically brings down the overhead power dissipation in NML devices.

On the other hand, a fast moving domain wall can upgrade the operating speed. On the basis of extensive earlier study [117] [144] [145] and also our own simulation study on domain wall dynamics. The speed of a domain wall is at a few hundred-meters per second in thin Permalloy layer, and this value rises up as the in-plane field increases [145]. Clearly, there is a trade-off between the speed performance and the power consumption by raising the in-plane field. However, it is possible to find a DWC with a high intrinsic wall speed driven by a satisfying low field [146]. With a very pessimistic estimate, a DW-clocked NML device can have a working frequency at 100 MHz, which is acceptable for specific applications.

However, there is a drawback that the Permalloy DWC has to be very narrow ($\sim$ 100 nm) in order to obtain a relatively stable domain wall field. As a result, each DWC could only probably clock one-dimensional dot-chains. There is still no

good solution for clocking the gates, where information flows two-dimensionally. Though it is possible to have DWCs laying in both in x and y in-plane direction, the fabrication and information control become prohibitively complicated.

In the future efforts, the following are worth considered:

1. To replace the Permalloy DWC, an idea DWC should posses features such as (a) a larger natural domain size, (b) a stable and fast domain wall motion and (c) an uniform and strong domain wall field.

2. Exchange interaction and spin-transfer torque [147] [148] can be taken into account as new approaches to manipulate the domain wall.

3. The circuit area can be divided into different clocking zones, which can increase the working frequency. However, it's fairly tricky to realize the manipulation of the local in-plane fields.

The blue print is sketched in Fig. 7.16, where much wider DWCs are taken in use to clock several gates and chip area is divided into multiple clocking zones. The domain wall injector on the left end generates one head-to-head wall and one tail-to-tail wall alternately.

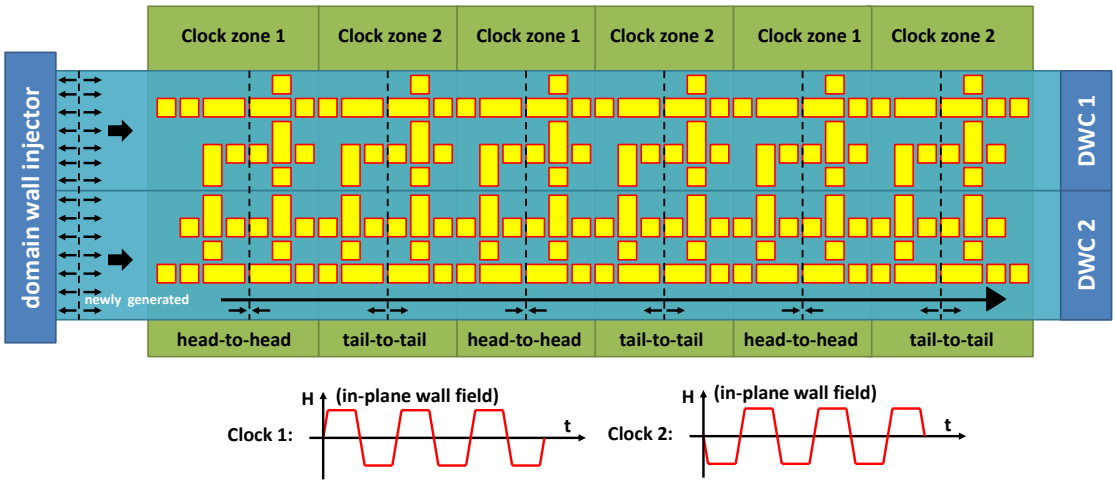

Figure 7.16. A draft of one ideal DW-clocked NML circuits.

CHAPTER 8

CONCLUSIONS

8.1 Summary of the dissertation work

As is known in nowadays electronic industry, the main stream of information computing has been accomplished through electronic phenomena and data storage has been done through magnetic phenomena. In this dissertation, however, our efforts have been made to investigate Nanomagnet Logic, which combines the data process and memory using only magnetic phenomena. In particular, we focused on NML built from Co/Pt nanomagnets with out-of-plane anisotropy.

At this point, I would like to sum up my original contributions to the research.

I first developed a calibrated model for Co/Pt multilayer films by fitting experimental hysteresis curves. We verified this model can fairly precisely describe the characteristics of Co/Pt nanomagnets, which allowed us to have an in-depth understanding of their switching behaviors.

I theoretically analyzed the source of those most frequently observed errors in NML and provided our solutions to eliminate these metastable states.

The most contributive part through my dissertation is that I proposed the model of partially irradiated nanomagnets. The computational study proved that these engineered dots can induce asymmetrical coupling, also called non-reciprocal coupling from the circuit point of view. This induced asymmetry in coupling makes a great contribution because in this case back-propagation is avoided during information processing and in the end uni-direction can be achieved.

I discussed the preconditions of required clocking field in order to drive the partially irradiated magnets to computational ground state. Actually, we verified

via theory and simulations that an global external oscillating field with a proper amplitude is sufficient, which is rather simpler than the clocking structure where current pulses are applied in the underneath metal wires.

I presented our specific design of a large scale circuit (systolic architecture) built from Co/Pt based NML. This is the first attempt in more complex circuit level. Our simulations confirmed the error-free data processing can be realized in a large number of gates.

In addition, we invented a new clocking scheme – clocking NML with domain wall conductors, which may further reduce the power dissipation of the clocking structure and improve the performance. Our simulations verified its feasibility and experimental work is ongoing.

8.2 Outlook of the future work

A fully functional NML system is composed of (1) an electronic/magnetic interface serving as input, (2) strongly field-coupled nanomagnets which store and process binary data, (3) a clocking structure to drive and control the information flow and (4) an electronic readout mechanism. Within the scope of this dissertation, we mainly applied ourselves to part (2) and part (3).

As for (1), besides using current pulses to set the input value [128], recent development of spintronics offers more possibilities to feed the inputs, such as spin transfer torque (STT) induced switching in Magnetic Tunnel Junctions (MTJ) [149] and spin valve interface [150]. On the other hand, the magnetic-electrical (readout) interface can be accomplished with MTJs [151], or GMR sensing. Our colleagues are making progress on the input and readout mechanism in experiments.

Based on my knowledge, I would like to address the following issues, which I believe are the ones most worthy looking into and of the great significance for NML devices in the near future.

1. Process variations: Precisely defined geometry and homogeneous material

properties during fabrication result in a narrow switching field distribution, which plays an important role in ordering the nanomagnets. So far it is still challenging to fabricate sub-100 nm Co/Pt dots with FIB lithography. A large variation of dot sizes and unexpected pinning sites all rise the probabilities of having error metastable states, which disturb the normal order. Meanwhile partially irradiation also requires to be implemented with a accurate dose and at the accurate positions to ensure the information propagation. We have proved, the single-domain state is well perserved in sub-100 nm scale. Fabricating sub-100 nm dots with acceptable process variations can remarkably enhance the robustness of NML devices.

2. Thermal effect: First of all, thermal fluctuations is another factor influencing the SFD. Secondly, the switching behavior of nanomagnets at high temperature is still unknown. In most of the simulations, thermal noise was not really considered. These thermal effects set a few qualifying conditions for NML devices. Further investigations regarding these effects are still needed in both simulations and experiments.

3. Power dissipation: The switching of nanomagnets consumes very little power at room temperature (less then 1 atto-Joules per switching). However, the power consumed in order to generate a clocking field, as the overhead, is dominant in the total power dissipation. In this dissertation, we described our power-efficient clocking schemes. We also proposed that new materials with lower coercivity (e.g. Co/Ni) can be applied to further bring down the energy cost. Our experimental group just initialized their research on Co/Ni system. In low-temperature operating NML, using superconducting materials as clocking wires may be taken into account, since there is no Joule heat loss.

4. Design of NML architecture: there are already literatures about architecture design of NML devices. However, there it was simply assumed all

the dots 'should work' and the model was developed directly by the system level hardware description language (HDL) [152] [153]. In other words, it's not physics-based model. We presented our design of a systolic pattern matcher for NML [154], which is the first design of a large scale circuits with micromagnetic simulation tools. In the later work, more suitable architectures, especially where low power dissipation becomes the main issue, could be thought over as candidates for NML applications. Actually, the anti-ferromagnetic ordering of nanomagnets is even considerable in much broader fields, such as non-Boolean information processing [155].

APPENDIX A

INVESTIGATION ON THE COUPLING AND SWITCHING BEHAVIORS OF PERMALLOY NANOMAGNETS.

The appendix summaries the work cooperated with nanomagnetism group at Notre Dame. Particularly, most of the experimental fabrication and measurements were done by Peng Li. I implemented computational study in order to have a pellucid explanation of experimental observations and provide theoretical assistance for ongoing study in laboratory.

Note within the scope of this appendix, we focus on Supermalloy ($Ni_{79}Fe_{16}Mo_5$) nanomagnet arrays. The units of H- field and B-field are given in cgs system (Oersted and gauss) instead of the ones in SI system (A/m and tesla).

A.1 Switching behavior of lithographically fabricated Permalloy nanomagnets

In NML, ideally each nanomagnet should switch coherently. However, metastable magnetization states, thermal fluctuations, and size and shape variations significantly complicate this simple picture yielding complex, non-uniform magnetization reversals. In order to build reliable NML devices and predictive computational models, the switching behavior must be thoroughly understood. While much work has focused on coupled magnets, including densely packed Permalloy dot chains [156], arrays [157] [158] [159] [160], and Co dots [161], there were only a few studies on sub-200 nm, lithographically fabricated non-interacting dots [162]. Here, we carry out experiments and simulations to study the switching behavior and magnetization states of the nanomagnets. Understanding the sources of non-ideal behaviors will yield better design tools so that error tolerances of NML circuits can be enhanced.

Rectangular Supermalloy nanomagnet arrays are fabricated using electron beam lithography (EBL), followed by evaporation and lift-off. Because NML requires strong coupling between nanomagnets, we choose rectangular shapes for this study as opposed to, say, elliptical that would be easier to fabricate, since rectangular magnets provide optimum coupling. To make the template for the nanomagnets, 100 nm poly(methyl-methacrylate) (PMMA) is spun onto a silicon substrate, and baked at 170 °C for 2 min. Elionix 7700 EBL system is used to define the patterns, and a solution of methyl-isobutyl ketone (MIBK), isopropanol (IPA) and methyl-ethyl ketone (MEK) is used for development. Electron beam evaporation is made at a base pressure of 9 $\times 10^{-7}$ torr with a growth rate of 0.1 nm/s. Then a 10 nm titanium underlayer is predeposited beneath the 20 nm Supermalloy layer to improve the adhesion. Dichloromethane is used for the final lift-off step. The size of the nanomagnets is 100 nm $\times$ 200 nm $\times$ 20 nm in sample A and 60 nm $\times$ 120 nm $\times$ 20 nm in sample B. On the order of 10^7 nominally identical rectangular nanomagnets are produced for each sample. The magnets are placed sufficiently far apart so that coupling field interactions are negligible. The inset of Fig. A.1 shows a scanning electron microscope (SEM) image of the nanomagnet array in sample A.

To characterize the nanomagnet behavior, we use a Microsense EV7 variable-temperature vibrating sample magnetometer (VSM), Micromag 2900 alternating gradient magnetometer (AGM), and Veeco MultiMode V AFM/MFM. Large-scale micromagnetic simulations are implemented to help interpret the experimental findings.

Fig. A.1 (a) shows measured hysteresis loops of sample A. The red and black curves are recorded along the long and short geometrical axes, which correspond to the easy and hard magnetization axes, respectively. Ideally, nanomagnets with such a size should show an abrupt switching along the easy axis, but the measured curve is broadened.

Fig. A.1 (b) demonstrates the hysteresis loops of 100 nm $\times$ 200 nm $\times$ 20 nm

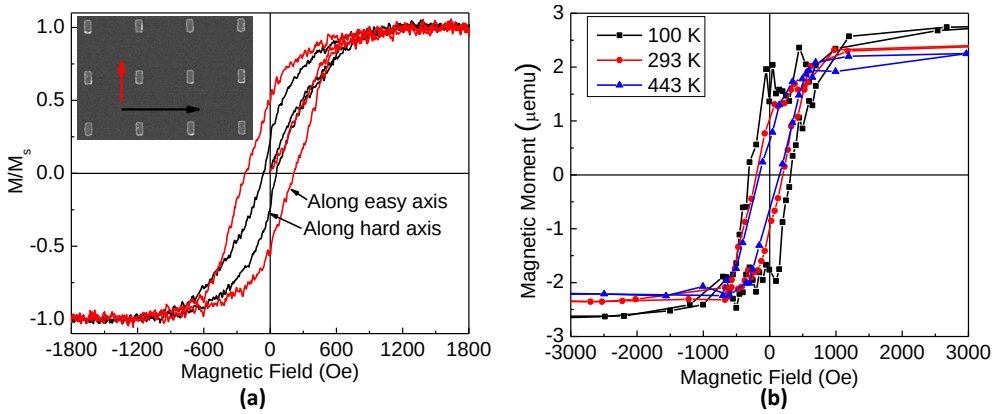

Figure A.1. (a) Measured hysteresis loops along the hard and easy axes of nanomagnets at room temperature. Inset: SEM image of the nanomagnet array (Sample A). (b) Hysteresis loops of nanomagnets (sample A) along the easy axis at different temperatures.

nanomagnets along their easy axes measured at 100 K, 293 K and 443 K. When the temperature was reduced from 443 K to 100 K, the switching field (coercivity) distribution of the loop is also reduced, the squareness ratio increased from 0.28 to 0.61, and the coercivity increased from 149 Oe to 321 Oe.

We perform micromagnetic simulations to investigate the contributions of shape variations and temperature fluctuations on nanomagnet behaviors. Shape variation is considered by randomly moving the positions of the corners of a 100 nm $\times$ 200 nm $\times$ 20 nm nominal sized rectangular magnet within a $\Delta x = \Delta y =$ 10 nm diameter circle (see inset of Fig. A.2). This simple model is intended to account for variations in switching fields, shape anisotropy and nucleation events that occur in variously shaped corners of the magnets. A hundred simulated hysteresis curves were averaged at T = 0 K as shown in Fig. A.2 (a). The width of the shape-induced switching field distribution is in reasonable agreement with low-temperature measurements, though the zero-kelvin simulation still overestimates the switching field.

Fig. A.2 (b) shows the combined effect of shape variations and temperature fluctuations for smaller, 60 nm $\times$ 90 nm $\times$ 10 nm magnets. Thermal effects reduce the switching field and further widen the switching field distribution.

Temperature-dependent simulations of 100 nm × 200 nm × 20 nm nanomagnets (not shown) did not replicate the measured strong temperature dependence in Fig. A.1 (b). We believe this is due to the simulated sweep rate of 100 ns/sweep (limited by computational restrictions) compared to several hours/sweep for the measurements. In literature [163], it has been demonstrated that sweep rate can have a significant effect on the switching field, but such long simulations are not possible.

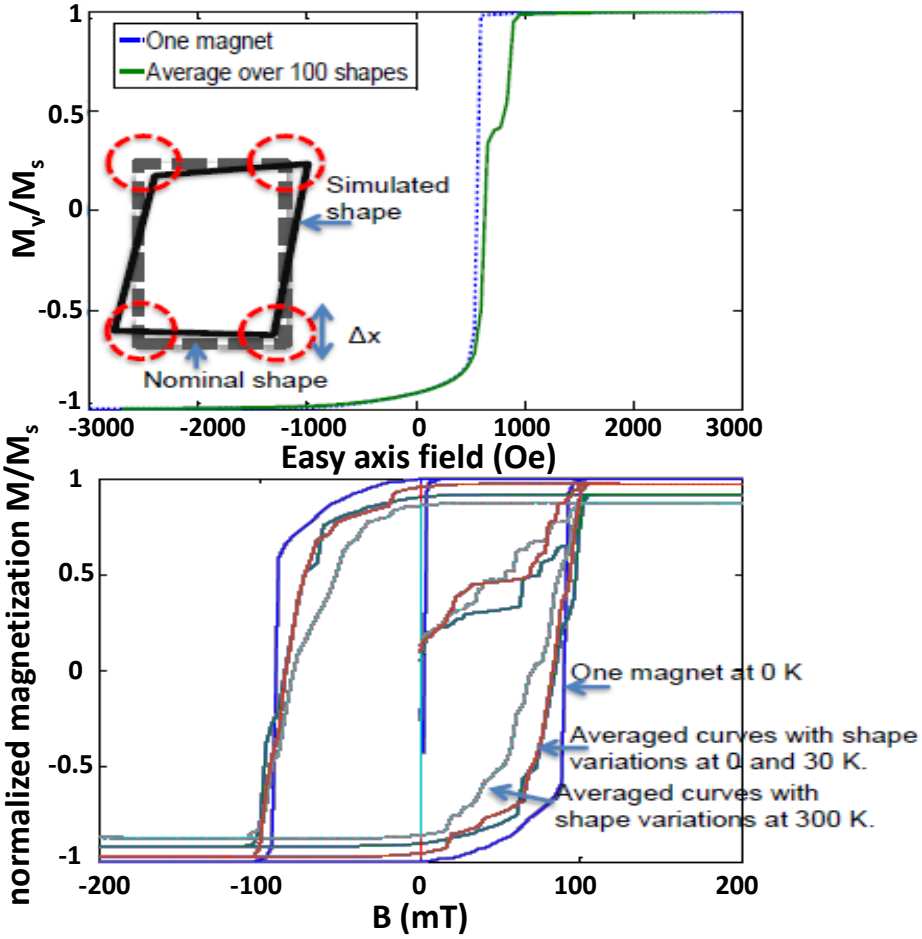

Figure A.2. (a) Simulated half hysteresis curve of 100 nm × 200 nm × 20 nm nanomagnets at 0 K. (b) Shape and size effect for 60 nm × 90 nm × 10 nm magnets at various temperatures.

The hard-axis hysteresis loop (Fig. A.1) shows strong remanent magnetization M_r (M_r refers here to only the hard-axis remanent magnetization) instead of an ideally zero remanence. Micromagnetic simulations showed that two types of

magnetization states can contribute to M_r, namely end-domain [164] and flower-like metastable states, both of which are shown in the insets of Fig. A.3 (a).

Simulation results suggest that metastable states are sensitive to external magnetic fields. By applying a weak easy-axis oscillating field, the metastable states can be easily destabilized.

We magnetized the nanomagnets along the hard axis with a 10 kOe constant field for 10 s (step 1). Upon removal of the field, we measured the hard-axis remanent magnetization (step 2). Subsequently, an oscillating field with amplitude of 30 Oe (Hosc = 30 Oe) and frequency of 1 Hz was applied along the easy axis for 10 s (step 3). After the removal of H_{osc}, the hard-axis remanent magnetization was measured again (step 4). By repeating step 3 and 4 with higher-amplitude oscillating fields, we plotted M_r versus H_{osc} curves as shown in Fig. A.3 for samples A and B.

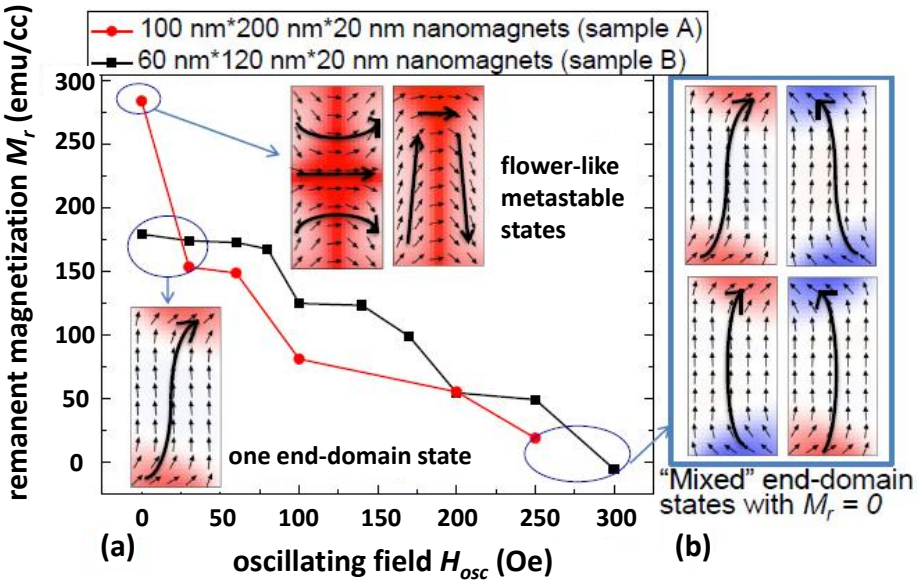

Figure A.3. (a) Hard-axis remanent magnetization M_r vs. easy-axis oscillating field H_{osc}. Insets: simulated metastable and end-domain states. (b) Mixed end-domain states carrying zero hard-axis magnetization ($M_r = 0$).

M_r for sample A was 284 emu/cc after the initial magnetization; after applying 30 Oe oscillating field along the easy axis, M_r dropped to 154 emu/cc. For stronger oscillating fields, M_r decreased gradually. For sample B, M_r remained constant

until H_{osc} = 80 Oe, and then it began to reduce and approached zero at higher H_{osc} (H_{osc}= 300 Oe).

The flower-like metastable and the end-domain states coexisted in the 100 nm × 200 nm × 20 nm nanomagnets (sample A) after the hard-axis magnetization, both contributed to M_r. The weak oscillating field of just 30 Oe (H_{osc} = 30 Oe) destabilized the flower-like metastable states, causing the initial drop of M_r. We believe that the existence of the initial metastable state is due to shape variations.

Higher H_{osc} fields afforded the opportunities for the end-domain state with the original hard-axis magnetization to change to 'mixed' end-domain states, as shown in Fig. A.3 (b). Higher oscillating fields (H_{osc} > 250 Oe) caused the end-domain states to choose randomly the hard-axis remanent magnetization, so the end-domain states became evenly 'mixed' and resulted in a zero M_r. These 'mixed' states are energetically equivalent to the end-domain state with the original hard-axis magnetization, but they require high H_{osc} field to be realized.

For the smaller nanomagnets (sample B), the end-domain state with the original hard-axis magnetization remained unchanged for Hosc < 80 Oe, but they gradually changed to 'mixed' end-domain states with $M_r = 0$ for higher H_{osc}.

To conclude, an oscillating field with amplitude of 30 Oe was sufficient to destabilize these metastable states; however, a high oscillating field (amplitude > 250 Oe) was required to reduce the remanence to zero. We can draw an analogy between this demonstration of using an oscillating field to demagnetize an array of single domain magnets with the same process using an oscillating field to demagnetize a bulk magnetic material, as is commonly done with tool demagnetizers and cathode ray tube 'degaussers'. In our case, the individual domains are physically separated, whereas in bulk materials they are contiguous.

Understanding such non-ideal switching behavior and the magnetization states of the nanomagnets brings us closer to finding the 'sweet spot' for ideally-sized and shaped nanomagnets that can serve as reliable building blocks for NML devices.

A.2 Direct measurement of magnetic coupling between nanomagnets for NML applications

In NML, magnetic coupling substitutes current flow as the primary carrier of information, which potentially yields large savings in power. Coupling between magnets should be strong, and give interaction energies well above those from thermal fluctuations. Single-domain nanomagnets currently used in NML are too large ($50 - 150$ nm) to rotate coherently. Additionally, they are placed close to each other, and exert highly inhomogeneous fields to each other. If coupled nanomagnets are placed in an external magnetic field, they will experience the superposition of external fields, demagnetization fields, and coupling fields, leading to complex magnetic switching behaviors with possible metastable states.

Experimental measurements indicate there is a magnetization component lying along hard-axes even in sub-200 nm magnets. Our computational study verified that metastable states, such as end-domain state, exist in non-coupled dot arrays. However, what kind of role are these metastable states playing in coupled case? In order to gain the picture, here we demonstrate a new method to sense the coupling directly and reveal the switching process among coupled magnets.

The primary tool of this measurement is a VSM with vector coils, which can sense magnetization vertical to external magnetic field during measurements [165].

Since a minimum of 2 μemu magnetic moment is needed to produce accurate curves, on the order of 10^7 Supermalloy nanomagnets with a size of 60 nm $\times$ 120 nm $\times$ 20 nm are fabricated in sample 1 and 2. We use one 100 nm thick PMMA layer as the template, which is intended to provide a deep undercut after development. The patterns are defined by an Elionix 7700 EBL system with a dose of 640 μC/cm^2. Development is done in a solution of MIBK, IPA and MEK, 1:3:1.5% respectively [166]. A 10 nm Ti adhesion layer followed by a 20 nm Supermalloy layer is evaporated for the sample. Lift-off is done in dichloromethane. More details about fabrication processes can be found in [167].

Fig. A.4 (a) shows a unit of two coupled magnets and Fig. A.4 (b) is a SEM

image of units placed far apart. The basic unit of sample 2 has two magnets that are placed in the same manner as in sample 1, but are sufficiently separated so as to be uncoupled, as shown in Fig. A.4 (c). Fig. A.4 (d) is an SEM image of sample 2. For later reference, the insets of Fig A.4 indicate the horizontal (x), vertical (y), and the external field directions. In the following, we name the magnet with its easy axis aligned horizontally (x) as driver magnet, and the one with its easy axis along the vertical (y) direction as driven magnet.

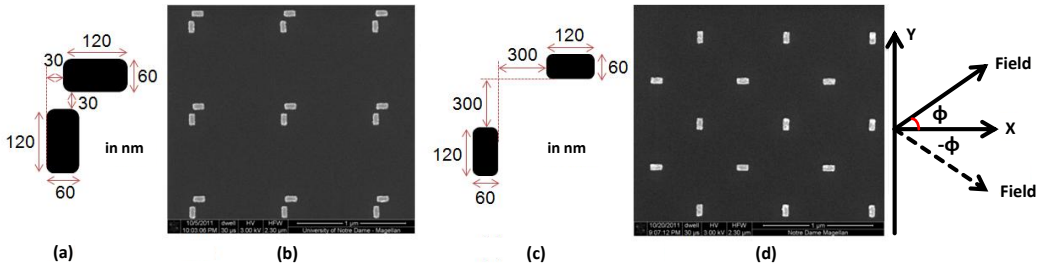

Figure A.4. (a) Layout of basic unit of coupled magnets. (b) SEM image of coupled magnets sample (sample 1). (c) Layout of basic unit of uncoupled magnets (sample 2). (d) SEM of non-coupled magnets sample (sample 2). The x and y axes, and the external field directions are also shown here.

Unless stated otherwise, we sweet the external magnetic field along the horizontal axis from +400 mT (pointing to the right) to −400 mT (pointing to the left) horizontally and sense magnetic moment along the vertical axis (M_y) to create M_y vs. B_{ext} curves. Due to shape anisotropies, M_y primary comes from the driven magnet, and this allows us to perceive the behaviors of the driven magnet under the influence of magnetic coupling.

First we measure the uncoupled magnets sample (sample 2) to see the situation when no coupling exists, and the results are shown in Fig. A.5. For this sample, if the external field is swept exactly along the x axis as in Fig A.5 (a), then we will sense almost zero M_y component, and this can be explained by the fact that the driven magnets turn up or down randomly since there is no coupling bias from the horizontal magnets. The measured curves are noisy, and this may be due to shape and size variations from fabrication and thermal fluctuations. The driver

magnets may contribute very little magnetic moment to M_y only via end-domain configurations [113].

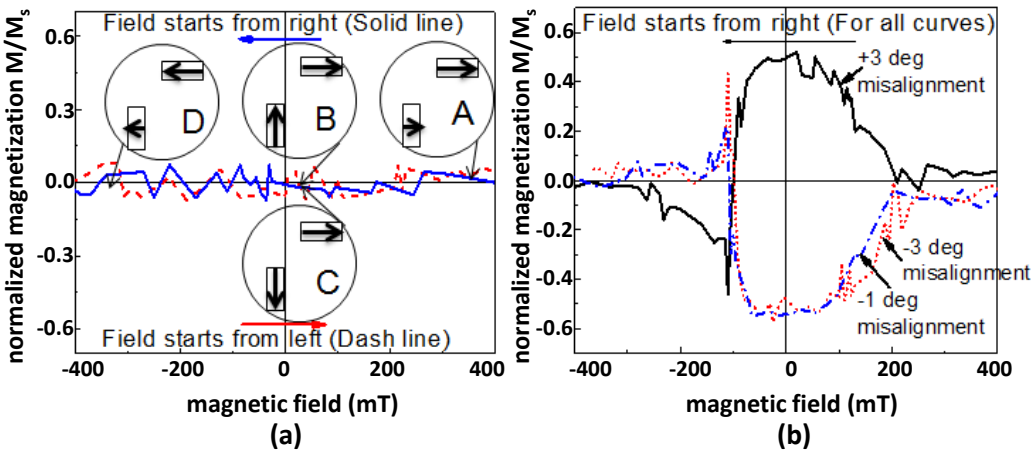

Figure A.5. (a) Curves measured when there is no misalignment between field and uncoupled magnets. (b) Curves measured at $\phi = \pm$ 3° and ϕ = -1° misalignments between the field and uncoupled magnets with respect to their easy/hard axes.

If the magnetic field (B_{ext}) is applied in a ϕ degree misalignment to the x axis then the external field will have a $B_y = B_{ext} \cdot sin(\phi)$ component along the easy axis of the driven magnets. When the field is relaxed ($B_{ext} = 0$), the magnetic moment (normalized to the entire volume of the ferromagnetic material) reaches $\pm 0.5 M_s$. For uncoupled magnets, the sign of M_y is decided by the sign of ϕ when B_{ext} becomes 0. At higher negative fields, M_y goes to zero as the magnet turns again to a hard-axis state.

For the coupled magnets sample, the coupling field ($B_{coupling}$) between the two magnets biases the driven magnet. If the external field is applied at a small misaligned angle with the horizontal axis sweeps from right to left, then its vertical component $B_y = B_{ext} \cdot sin(\phi)$ will have an opposite direction with the coupling field $B_{coupling}$, so $B_{coupling}$ competes with B_y, and the driven magnet will switch to the direction of the stronger one. In Fig. A.6, at $\phi = -1°$, the driven magnet flips upwards when the external field decreases from +400 mT to 0, and this means $B_{coupling} > B_y$; At $\phi = -3°$, the driven magnet flips downwards and this means $B_y > B_{coupling}$.

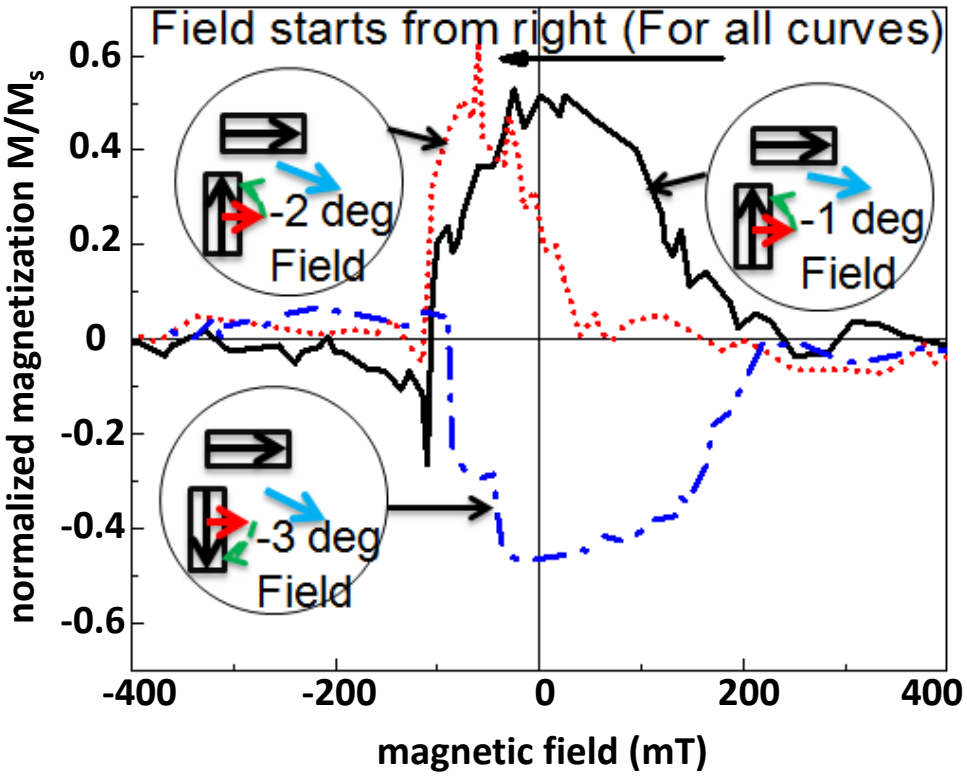

Figure A.6. Experimental M_y vs. B_x VSM curves of the coupled nanomagnet sample at different angles.

For $\phi = -2°$ (red curve in Fig. A.6) the shape of the M_y vs. B_{ext} curve changes, and the curve intersects with the $M_y = 0$ axis when $B_{ext} = 185$ mT. This is an indication that B_y cancels $B_{coupling}$, so according to $B_{coupling} = B_y = B_{ext} \cdot \sin(\phi)$, the coupling field strength from measurements is 6.5 mT.

A microspin model is developed to simulate these coupled dots. For more details of the modeling, see [168]. Here only the simulation result is presented in Fig. A.7

However, as seen there this microspin model is unable to predict the curve at $\phi = -2°$. Thus, we perform OOMMF simulations, where stand parameters of Permalloy (saturation magnetization $M_s = 8.6 \times 10^5$ A/m, exchange stiffness $A_{\text{exch}} = 1.3 \times 10^{-11}$ J/m^3, damping constant α= 0.5). Simulated curve for the $\phi = -2°$ case is given in Fig. A.8, with insets showing non-uniform magnetization states during reversal.

The micromagnetic simulation result has shown most of the features of the

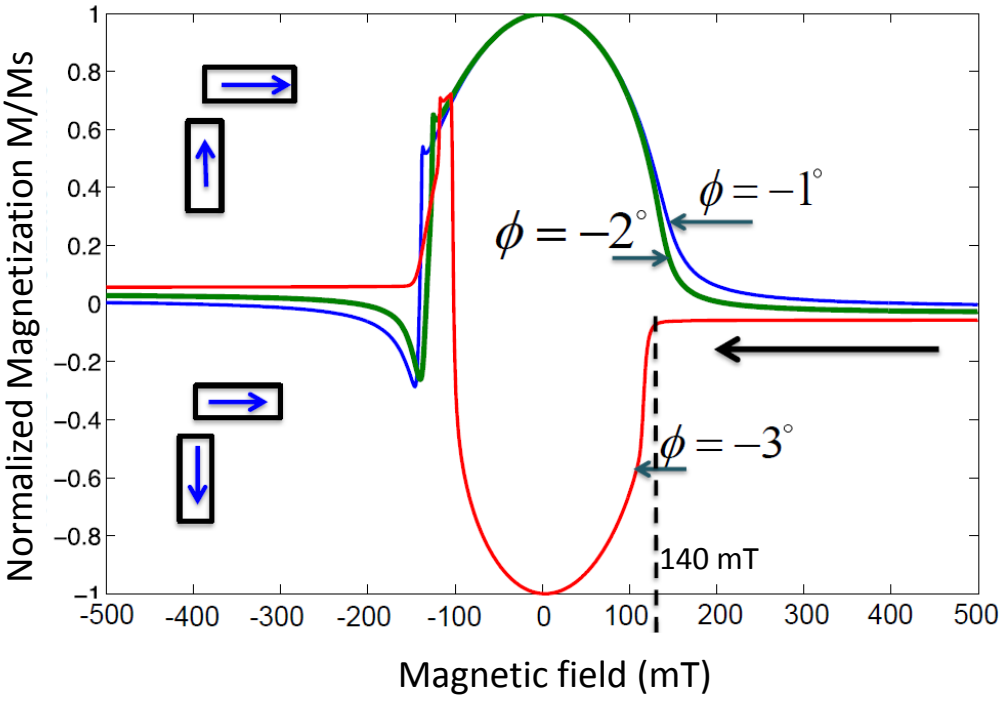

Figure A.7. M_y vs. B_{ext} curves for two coupled magnets calculated by microspin model.

measured curve for the $\phi = -2°$ case, although some peaks of the curve do not appear at the same fields. This might be due to the inaccuracy of setting measuring angles in the VSM.

The non-uniform magnetization states in the switching process are results of the splitting of magnetization by the homogeneous external field and inhomogeneous coupling field. The net field at the lower edges of driven magnet was pointing downwards, so the magnetization tends to turn down. However, at the upper and the central parts of the driven magnet, the net field is pointing upwards, so the magnetization tends to turn upwards. The quasi-uniform switching mode (which is observed at $\phi = -2°$) shows a highly non-uniform switching process with intermediate vortex states.

We found in a recent study [169] that end-domain states and metastable states are shown even in sub-100 nm size, near single-domain nanomagnets. While such nanomagnets appear to display single-domain state in images by MFM, the end

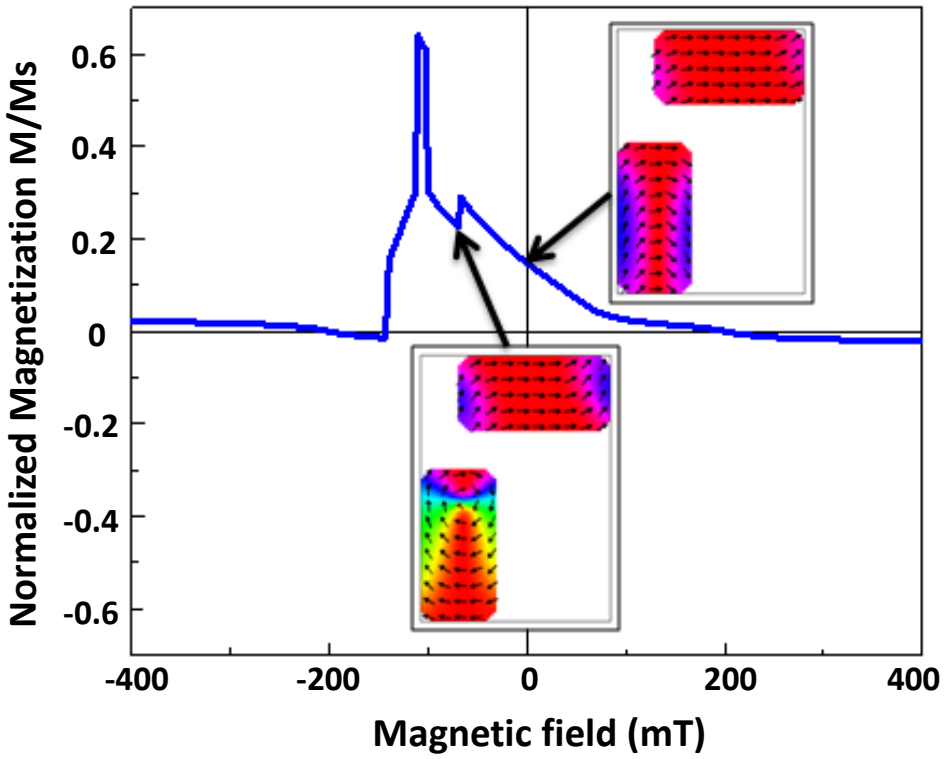

Figure A.8. Micromagnetic simulation of the nanomagnet switching at $\phi = -2°$. Insets show non-uniform magnetization states during reversal.

domain states can still play an important role in the switching process and may exist in the steady state of the magnets. These non-uniformities are difficult to observe with MFM, since the limited resolution of the microscope and the parasitic interaction between the tip and sample drive the multi-domain structure toward a single domain configuration with minimum energy. Non-invasive magnetic imaging methods can confirm the existence of end-domain states.

A spin-SEM image of coupled nanomagnets is shown in Fig. A.9. This sample is different from those shown in Fig. A.4, but it was magnetized using similar hard-axis fields. End domain states are clearly seen in the spin-SEM image. These states strongly influence surface charge distributions and coupling fields. It is interesting that despite their similar shape, the two vertical magnets end up displaying different end-domain configurations. We speculate that end-domain states in this coupled structures are induced by coupling fields.

From our study, it seems metastable states widely exist even in NML with foot-

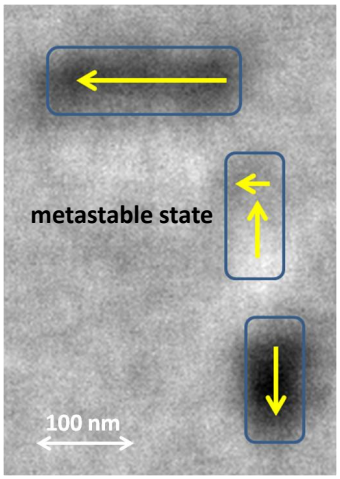

Figure A.9. Spin-polarized SEM image of nanomagnets revealing end-domain states in the coupled nanomagnets.

print of sub-100 nm. A clear understanding of the characters of these metastable states help lower the error-rate and enhance the reliability. Further study is necessary to fully evaluation the performance of NML, in particular, to verify the feasibility of error-free NML and its sustainability at room or high temperature.

APPENDIX B

RELATED PUBLICATIONS OF THE AUTHOR

1. X. Ju, S. Wartenburg, J. Rezgani, M. Becherer, J. Kiermaier, S. Breitkreutz, D. Schmitt-Landsiedel, W. Porod, P. Lugli and G. Csaba, "Nanomagnet Logic from Partially Irradiated Co/Pt Nanomagnets," *IEEE Transactions on Nanotechnology,* vol. 11, no. 1, pp. 97–104, 2012.

2. X. Ju, S. Wartenburg, M. Becherer, J. Kiermaier, S. Breitkreutz, D. Schmitt-Landsiedel, P. Lugli and G. Csaba, "Computational model of partially irradiated nanodots for field-coupled computing devices," *14th International Workshop on Computational Electronics (IWCE),* Pisa, 2010.

3. X. Ju, M. Becherer, J. Kiermaier, S. Breitkreutz, P. Lugli and G. Csaba, "Error analysis of Co/Pt multilayer based Nanomagnetic Logic," *11th IEEE Conference on Nanotechnology,* pp. 1034–1037, August, 2011.

4. X. Ju, M. T. Niemier, M. Becherer, W. Porod, P. Lugli and G. Csaba, "Application of Nanomagnetic Logic: Co/Pt based Systolic Pattern Matcher," submitted to *IEEE Transactions on Nanotechnology.*

5. X. Ju, M. T. Niemier, M. Becherer, W. Porod, P. Lugli and G. Csaba, "Design of a Systolic Pattern Matcher for Nanomagnet Logic," *15th International Workshop on Computational Electronics (IWCE),* 2012.

6. X. Ju, J. Kiermaier, M. Becherer, S. Breitkreutz, W. Porod, D. Schmitt-Landsiedel, P. Lugli and G. Csaba, "Computational Study of Domain-Wall-

Induced Switching of Co/Pt Multilayer," *15th International Workshop on Computational Electronics (IWCE),* 2012.

7. X. Ju, S. Wartenburg, M. Becherer, D. Schmitt-Landsiedel, P. Lugli, W. Porod and G. Csaba, "Simulation of Focused Ion Beam Patterned Cobalt-Platinum Multilayers," *Electronic Materials Conference (EMC),* 2010.

8. X. Ju, J. Kiermaier, M. Becherer, S. Breitkreutz, I. Eichwald, D. Schmitt-Landsiedel, W. Porod, P. Lugli and G. Csaba, "Modeling interaction between Co/Pt nanomagnets and Permalloy domain wall for Nanomagnet Logic," accepted for publication in *12th IEEE Conference on Nanotechnology,* 2012.

9. J. Kiermaier, S. Breitkreutz, X. Ju, G. Csaba, D. Schmitt-Landsiedel and M. Becherer, "Ultra-low volume ferromagnetic nanodots for field-coupled computing devices," *European Solid-State Device Research Conference (ESSDERC),* pp. 214–217, 2010.

10. J. Kiermaier, S. Breitkreutz, X. Ju, G. Csaba, D. Schmitt-Landsiedel and M. Becherer, "Field-coupled computing: Investigating the properties of ferromagnetic nanodots," *Solid-State Electronics,* vol. 65, pp. 240–245, 2011.

11. S. Breitkreutz, J. Kiermaier, X. Ju, G. Csaba, D. Schmitt-Landsiedel and M. Becherer, "Nanomagnetic Logic: Demonstration of directed signal flow for field-coupled computing devices," *European Solid-State Device Research Conference (ESSDERC),* pp. 323–326, 2011.

12. S. Breitkreutz, J. Kiermaier, C. Yilmaz, X. Ju, G. Csaba, D. Schmitt-Landsiedel and M. Becherer, "Nanomagnetic logic: Investigations on field-coupled computing devices by experiment-based compact modeling," *11th IEEE Conference on Nanotechnology,* pp. 1048–1251, August, 2011.

13. M. Becherer, J. Kiermaier, S. Breitkreutz, G. Csaba, X. Ju, J. Rezgani, T. Kießling, C. Yilmaz, P. Osswald, P. Lugli and D. Schmitt-Landsiedel, "On-

chip Extraordinary Hall-effect sensors for characterization of nanomagnetic logic devices," *Solid-State Electronics,* vol. 54, no. 9, pp. 1027–1032, 2010.

14. S. Breitkreutz, J. Kiermaier, C. Yilmaz, X. Ju, G. Csaba, D. Schmitt-Landsiedel and M. Becherer, "Nanomagnetic logic: compact modeling of field-coupled computing devices for system investigations," *Journal of Computational Electronics,* vol. 10, no. 4, pp. 352–359, 2011.

15. S. Breitkreutz, J. Kiermaier, I. Eichwald, X. Ju, G. Csaba, D. Schmitt-Landsiedel and M. Becherer, "Majority Gate for Nanomagnetic Logic with Perpendicular Magnetic Anisotropy," *2012 International Magnetics Conference,* Vancouver, 2012.

16. S. Breitkreutz, J. Kiermaier, I. Eichwald, X. Ju, G. Csaba, D. Schmitt-Landsiedel and M. Becherer, "Majority Gate for Nanomagnetic Logic with Perpendicular Magnetic Anisotropy," accepted for publication in *IEEE Transactions on Magnetics,* 2012.

17. P. Li, G. Csaba, V. K. Sankar, X. Ju, P. Lugli, X. S. Hu, M. Niemier, W. Porod, G. H. Bernstein, "Switching behavior of lithographically fabricated nanomagnets for logic applications," *J. Appl. Phys,* vol. 111, no. 7, 2012.

18. P. Li, G. Csaba, V. K. Sankar, X. Ju, P. Lugli, X. S. Hu, M. Niemier, W. Porod, G. H. Bernstein, "Switching behavior of lithographically fabricated nanomagnets for logic applications," *56th Annual Conference on Magnetism and Magnetic Materials,* 2011.

19. G. Csaba, J. Kiermaier, M. Becherer, S. Breitkreutz, X. Ju, P. Lugli, D. Schmitt-Landsiedel and W. Porod, "Clocking magnetic field-coupled devices by domain walls," *56th Annual Conference on Magnetism and Magnetic Materials,* 2011.

20. G. Csaba, J. Kiermaier, M. Becherer, S. Breitkreutz, X. Ju, P. Lugli, D.

Schmitt-Landsiedel and W. Porod, "Clocking magnetic field-coupled devices by domain walls," *J. Appl. Phys,* vol. 111, no. 7, 2012.

21. P. Li, G. Csaba, V. K. Sankar, X. Ju, E. Varga, P. Lugli, X. S. Hu, M. Niemier, W. Porod and G. H. Bernstein, "Direct Measurement of Magnetic Coupling between Nanomagnets for NML Applications," *IEEE International Magnetics Conference,* Vancouver, 2012.

22. P. Li, G. Csaba, V. K. Sankar, X. Ju, E. Varga, P. Lugli, X. S. Hu, M. Niemier, W. Porod and G. H. Bernstein, "Direct Measurement of Magnetic Coupling between Nanomagnets for NML Applications," accepted for publication in *IEEE Transactions on Magnetics,* 2012.

23. M. Niemier, X. Ju, M. Becherer, G. Csaba, X. S. Hu, D. Schmit-Landsiedel, P. Lugli and W. Porod, "Systolic Architectures and Applications for Nanomagnet Logic," accepted for publication in *Silicon Nanoelectronics Workshop,* 2012.

24. M. Niemier, X. Ju, G. Csaba, M. Becherer, A. Dingler, X. S. Hu, D. Schmit-Landsiedel, P. Lugli and W. Porod, "Boolean and Non-Boolean Nearest Neighbor Architectures for Out-of-Plane Nanomagnet Logic," accepted for publication in *International workshop on Cellular Nanoscale Networks and their Applications,* 2012.

25. G. Csaba, X. Ju, Z. Ma, Q. Chen, W. Porod, J. Schmidhuber, U. Schlichtmann, P. Lugli and U. Ruhrmair, "Application of mismatched Cellular Nonlinear Networks for Physical Cryptography," *12th International Workshop on Cellular Nanoscale Networks and Their Applications (CNNA),* 2010.

26. Q. Chen, G. Csaba, X. Ju, S. B. Natarajan, P. Lugli, M. Stutzmann, U. Schlichtmann and U. Ruhrmair, "Analog circuits for physical cryptography," *12th International Symposium on Integrated Circuits (ISIC),* 2009.

APPENDIX C

ACRONYMS

AND	AND: boolean function
CMOS	complementary metal-oxide semiconductor
DPU	data processing unit
DWC	domain wall conductor
DWL	Domain Wall Logic
EBL	electron beam lithography
EHE	extraordinary Hall effect
EPD	enhanced permeability dielectric
FET	field effect transistor
FIB	focused ion beam
GMR	giant magneto-resistance
HDL	hardware description language
iNML	in-plane Nanomagnet Logic
IPA	isopropanol
ITRS	International Technology Roadmap for Semiconductors
I/O	input/output
LC circuit	resonant circuit
LL	Landau-Lifshitz
LLG	Landau-Lifshitz-Gilbert
MEK	methyl-ethyl ketone
MFM	magnetic force microscope
MIBK	methyl-isobutyl ketone
ML	multilayer
MOKE	magneto-optical Kerr effect

MQCA	Magnetic Quantum-dot Cellular Automata
MRAM	Magneto-resistive Random Access Memory
MTJ	magnetic tunnel junction
NAND	NAND: NOT AND function
NML	Nanomagnet Logic
NOT	NOT: boolean function
oNML	out-of-plane Nanomagnet Logic
OOMMF	object oriented micromagnetic framework
Oxsii	OOMMF eXtensible solver interactive interface
PE	processing elements
PID	partially irradiated dot
PMA	perpendicular magnetic anisotropy
PMMA	poly(methyl-methacrylate)
QCA	Quantum-dot Cellular Automata
SEM	scanning electron microscope
SFD	switching field distribution
SPICE	simulation program with integrated circuit emphasis
SPM	systolic pattern matcher
SQUID	superconducting quantum interference device
SRIM	stopping and range of ions in matter
STT	spin transfer torque
TRIM	transmission and range of ions in matter
VSM	vibrating sample magnetometer
XOR	Exclusive OR: boolean function
XNOR	inverse of XOR: boolean function

BIBLIOGRAPHY

[1] 'Emerging Research Devices' section of the International Technology Roadmap for Semiconductors, available: http://www.itrs.net/.

[2] http://en.wikipedia.org/wiki/Compass

[3] N. Z. Haron and S. Hamdioui, Why is CMOS scaling coming to an END, *3rd International Design and Test Workshop,* pp. 98–103, 2008.

[4] C. S. Lent, P. Tougaw, W. Porod and G. Bernstein, Quantum cellular automata, *Nanotechnology,* vol. 4, pp. 49–57, 1993.

[5] R. J. Spain, Controlled Domain Tip Propagation. Part I, *J. Appl. Phys.,* vol. 37, no. 7, pp. 2572–2583, 1966.

[6] R. J. Spain and H. I. Jauvtis, Controlled Domain Tip Propagation. Part II, *J. Appl. Phys,* vol. 37, no. 7, pp. 2584–2593, 1966.

[7] D. O. Smith, *Magnetic domain wall storage and logic,* US Patent No. 3176276, Issue date: Mar 1965.

[8] R. P. Cowburn and M. E. Welland, Room Temperature Magnetic Quantum Cellular Automata, *Science,* vol. 287, no. 5457, pp. 1466–1468, 2000.

[9] M. Forshaw, R. Stadler, D. Crawley and K Nikolic, A short review of nanoelectronic architectures Nanotechnology, *Nanotechnology,* vol. 15, no. 4, pp. 220–223, 2004.

[10] B. D. Cullity and C. D. Graham, *Introduction to magnetic materials,* Piscataway, NJ, IEEE Press, 2009.

[11] A. Aharoni, *Introduction to the Theory of Ferromagnetism,* Oxford University Press, Oxford, 1996.

[12] R. P. Cowburn, D. K. Koltsov, A. O. Adeyeye and M. E. Welland, Single-Domain Circular Nanomagnets, *Physical Review Letters,* vol. 83, no. 5, pp. 1042–1045, 1999.

[13] N. Vernier, D. A. Allwood, C. D. Atkinson, M. D. Cooke, and R. P. Cowburn, Domain wall propagation in magnetic nanowires by spin-polarized current injection, *Europhysics Letters,* vol. 65, pp. 526–532, 2004.

[14] D. A. Allwood, G. Xiong, M. D. Cooke, C. C. Faulkner, D. Atkinson, N. Vernier and R. P. Cowburn, Submicrometer Ferromagnetic NOT Gate and Shift Register, *Science,* vol. 296, pp. 2003–2006, 2002.

[15] X. Zhu, D. A. Allwood, G. Xiong, R. P. Cowburn and P. Grutter, Spatially resolved observation of domain-wall propagation in a submicron ferromagnetic NOT gate, *Applied Physics Letters,* vol. 87, no. 062503, 2005.

[16] D. A. Allwood, G. Xiong, C. C. Faulkner, D. Atkinson, D. Petit and R. P. Cowburn, Magnetic Domain-Wall Logic, *Science,* vol. 309, no. 5741, pp. 1688–1692, 2005.

[17] D. A. Allwood, G. Xiong and R. P. Cowburn, Magnetic domain wall serial-in parallel-out shift register, *Applied Physics Letters,* vol. 89, no. 102504, 2006.

[18] L. O'Brien, D. Petit, H. T. Zeng, E. R. Lewis, J. Sampaio, D. E. Read and R. P. Cowburn, Near-Field Interaction between Domain Walls in Adjacent Permalloy Nanowires, *Physical Review Letters,* vol. 103, no. 077206, 2009.

[19] D. Petit, A. Jausovec, H. T. Zeng, E. Lewis, L. O'Brien, D. Read and R. P. Cowburn, Mechanism for domain pinning potential landscape modification by artificially patterned traps in ferromagnetic nanowires, *Physical Review B,* vol. 79, no. 214405, 2009.

[20] E. R. Lewis, D. Petit, L. O'Brien, A. Fernandez, J. Sampaio, A. Jausovec, H. T. Zeng, D. E. Read and R. P. Cowburn, Fast domain wall motion in magnetic comb structures, *Nature Materials,* vol. 9, pp. 980–983, 2010.

[21] H. T. Zeng, D. E. Read, L. O'Brien, J. Sampaio, E. R. Lewis, D. Petit and R. P. Cowburn, Asymmetric magnetic NOT gate and shift register for high density data storage, *Applied Physics Letters,* vol. 96, no. 262510, 2010.

[22] D. Petit, A. V. Jausovec, D. E. Read, and R. P. Cowburn, Domain wall pinning and potential landscapes created by constrictions and protrusions in ferromagnetic nanowires, *J. Appl. Phys.,* vol. 103, no. 114307, 2008.

[23] G. Csaba and W. Porod, Simulation of Field-Coupled Computing Architectures Based on Magnetic Dot Arrays, *Journal of Computational Electronics,* vol.1, no. 1–2, pp. 87–91, 2002.

[24] G. Csaba, A. Imre, G. H. Bernstein, W. Porod and V. Metlushko, Nanocompting by Field-Coupled Nanomagnets, *IEEE Transactions on Nanotechnology,* vol. 1, pp. 209–213, 2002.

[25] G. Csaba, W. Porod and A. I. Csurgay, A computing architecture composed of field-coupled single domain nanomagnets clocked by magnetic fields, *International Journal of Circuit Theory and Applications,* vol. 31, no.1, pp. 67–82, 2003.

[26] G. Csaba and W. Porod, Computing Architectures for Magnetic Dot Arrays, *First International Conference and School on Spintronics and Quantum Information Technology,* Hawaii, 2001.

[27] G. Csaba and W. Porod, Simulation of field-coupled computing architectures based on magnetic dot arrays, *8th International Workshop on Computational Electronics,* Beckman Institute, 2001.

[28] W. Porod, G. Csaba and A. I. Csurgay, Field-Coupled Devices for Nanoelectronic Integrated Circuits, *First International Workshop on Quantum Dots for Quantum Computing and Classical Size Effect Circuits,* Kochi, Japan, 2002.

[29] G. Csaba and W. Porod, Design and Realizability of Logic Devices Based on Field-Coupled Nanomagnets, *March Meeting of the American Physical Society,* 2002.

[30] G. Csaba, A. Imre, G. H. Bernstein, W. Porod and V. Metlushko, Signal Processing with Coupled Ferromagnetic Dots, *the Second IEEE Conference on Nanotechnology,* Washington, DC, 2002.

[31] G. Csaba, A. Imre, G. H. Bernstein, V. Metlushko and W. Porod, Application of Magnetic Rings for Field-Coupled Computing, *Fourth International Symposium on Nanostructures and Mesoscopic Systems,* Tempe, 2003.

[32] A. Imre, G. Csaba, G. H. Bernstein, W. Porod and V. Metlushko, Investigation of shape-dependent switching of coupled nanomagnets, *Superlattices and Microstrucures,* vol. 34, no. 3–6, pp. 513–518, 2003.

[33] A. Imre, G. Csaba, V. Metlushko, G. H. Bernstein and W. Porod, Controlled domain wall motion in micron-scale permalloy square rings, *Physics E: Low-dimensional Systems and Nanostructures,* vol. 19, no. 1–2, pp. 240–245, 2003.

[34] A. Imre, G. Csaba, P. Lugli, G. H. Bernstein, V. Metlushko and W. Porod, Magnetic Logic Devices, *Advanced Heterostructure Workshop,* Hawaii, December 2004.

[35] A. Orlov, A. Imre, G. Csaba, L. Ji, W. Porod, and G. H. Bernstein, Magnetic Quantum-Dot Cellular Automata: Recent Developments and Prospects, *Journal of Nanoelectronnics and Optoelectronics,* vol. 3, no. 1, pp. 55–68, 2008.

[36] A. Imre, G. Csaba, L. Ji, A. Orlov, G. H. Bernstein and W. Porod, Majority Logic Gate for Magnetic Quantum-Dot Cellular Automata, *Science,* Vol. 311, no. 5758, pp. 205–208, 2006.

[37] E. Varga, G. Csaba, G. H. Bernstein and W. Porod, Implementation of Nanomagnetic Full Adder Circuit, *11th IEEE International Conference on Nanotechonoloy,* Portland, 2011.

[38] M. A. Imtaar, A. Yadav, A. Epping, G. Scarpa and P. Lugli, Single domain nanomagnet fabrication using electrodeposition, nanoimprinting and focused ion beam cutting, *TUM Nanomagnetik-Workshop,* Munich, Feb. 2012.

[39] G. Csaba, P. Lugli, A. Csurgay and W. Porod, Simulation of power gain and dissipation in field-coupled nanomagnets, *Journal of Computational Electronics,* vol. 4, no. 1–2, pp. 105–110, 2005.

[40] G. Csaba, P. Lugli and W. Porod, Power dissipation in nanomagnetic logic devices, *4th IEEE Conference on Nanotechnology,* Munich, 2004.

[41] M. T. Niemier, X. S. Hu, M. Alam, G. Bernstein, W. Porod, M. Putney and J. DeAngelis, Clocking Structure and Power Analysis for Nanomagnet-Based Logic Devices, *International Symposium on Low Power Electronics and Design,* pp. 26–31, Portland, 2007.

[42] M. T. Alam, M. J. Siddiq, G. H. Bernstein, M. T. Niemier, W. Porod and X. S. Hu, On-chip Clocking for Nanomagnet Logic Devices, *IEEE Transactions on Nanotechnology,* vol. 9, no. 3, 2010.

[43] A. Dingler, M. J. Siddiq, M. T. Niemier, X. S. Hu, M. T. Alam, G. H. Bernstein and W. Porod, Controlling Magnetic Circuits: How Clock Structure Implementation will Impact Logical Correctness and Power, *24th IEEE*

International Symposium on Defect and Fault Tolerance in VLSI Systems, Chicago, 2009.

[44] A. Dingler, M. T. Niemier, X. S. Hu, M. Garrison and M. T. Alam, System-Level Energy and Performance Projections for Nanomagnet-based Logic, *IEEE/ACM International Symposium on Nanoscale Architectures,* 2009.

[45] A. Dingler, M. T. Niemier, X. S. Hu and E. Lent, Performance and Energy Impact of Locally Controlled NML Circuits, *Journal on Emerging Technologies in Computing Systems,* vol. 7, no. 1, 2011.

[46] S. V. Pietambaram, Low-power switching in magnetoresistive random access memory bits using enhanced permeability dielectric films, *Applied Physics Letters,* vol. 90, no. 143510, 2007.

[47] H. Koop, H. Brückl, D. Meyners and G. Reiss, Shape dependence of the magnetization reversal in sub-μm magnetic tunnel junctions, *Journal of Magnetism and Magnetic Materials,* vol. 272–276, pp. E1475–E1476, 2004.

[48] M. T. Niemier, E. Varga, G. H. Bernstein, W. Porod, M. T. Alam, A. Dingler A. Orlov and X. S. Hu, Shape Engineering for Controlled Switching With Nanomagnet Logic, *IEEE Transactions on Nanotechnology,* vol. 11, no.2, pp. 220–230, 2012.

[49] S. Kurtz, E. Varga, M. J. Siddiq, M. T. Niemier, W. Porod, X. S. Hu and G. H. Bernstein, Non-majority magnetic logic gates: a review of experiments and future prospects for 'shape-based' logic, *Journal of Physics: Condens. Matter,* vol. 23, no. 053202, 2011.

[50] E. Varga, M. Siddiq, M. T. Niemier, G. H. Bernstein, W. Porod, X. S. Hu and A. Orlov, Experimental demonstration of non-majority, nanomagnet logic gates, *Device Research Conference,* pp. 87–88, 2010.

[51] R. H. Victoria and Xiao Shen, Composite Media for Perpendicular Magnetic Recording, *IEEE Transactions on Magnetics,* vol. 41, no. 2, pp. 537–542, 2005.

[52] S. Iwasaki, Perpendicular magnetic recording, *IEEE Transactions on Magnetics,* vol. 16, no. 1, pp. 71–76, 1980.

[53] W. B. Zeper, F. Greidanus, P. F. Carcia and C. R. Fincher, Perpendicular magnetic anisotropy and magneto-optical Kerr effect of vapor-deposited Co/Pt-layered structures, *Journal of Applied Physics,* vol. 65, no. 12, pp. 4971–4975, 1989.

[54] S. Iwasaki, Y. Nakamura and K. Ouchi, Perpendicular magnetic recording with a composite anisotropy film, *IEEE Transactions on Magnetics,* vol. 15, no. 6, pp. 1456–1458, 1979.

[55] C. P. Luo, S. H. Liou, L. Gao, Y. Liu and D. J. Sellmyer, Nanostructured FePt: B_2O_3 thin lms with perpendicular magnetic anisotropy, *Appl. Phys. Lett.,* vol. 77, no. 14, 2000.

[56] H. Meng and J. P. Wang, Spin transfer in nanomagnetic devices with perpendicular anisotropy, *Appl. Phys. Lett.,* vol. 88, no. 172506, 2006.

[57] M. Nakayama, T. Kai, N. Schimomura, M. Amano, E. Kitagawa, T. Nagase, M. Yoshikawa, T. Kishi, S. Ikegawa and H. Yoda, Spin transfer switching in TbCoFe/CoFeB/MgO/CoFeB/TbCoFe magnetic tunnel junctions with perpendicular magnetic anisotropy, *Journal of Applied Physics,* vol. 103, no. 07A710, 2008.

[58] S. Gadetsky, J. K. Erwin, M. Mansuripur and S. Suzuki, Magneto-optical recording on patterned substrates, *Journal of Applied Physics,* vol. 79, no. 8, pp. 5687–5692, 1996.

[59] C. Chappert, H. Bernas, J.Ferré, V. Kottler, Y. Chen, E. Cambril, T. Devolder, F. Rousseaux, V. Mathet and H. Launois, Planar patternedmagnetic media obtained by ion irradiation, *Science,* vol. 280, pp. 1919–1922, 1998.

[60] C. T. Rettner, M. E. Best and B. D. Terris, Patterning of granular magnetic media with a focused ion beam to produce single domain islands at > 140 Gbit/in^2, *IEEE Transactions on Magnetics,* vol. 37, no. 4, pp. 1649–1651, 2001.

[61] C. T. Rettner, S. Anders, T. Thomson, M. Albrecht, Y. Ikeda, M. E. Best and B. D. Terris, Magnetic characterization and recording properties of patterned $Co_{70}Cr_{18}Pt_{12}$, *IEEE Transactions on Magnetics,* vol. 38, pp. 1725–1730, 2002.

[62] M. Albrecht, C. T. Rettner, M. E. Best and B. D. Terris, Magnetic coercivity patterns for magnetic recording on patterned media, *Applied Physcis Letters,* vol. 83, no. 21, pp. 4363–4365, 2003.

[63] G. Csaba, *Computing with field-coupled nanomagnets,* Ph. D dissertation, University of Notre Dame, 2003.

[64] J. A. C. Bland and B. Heinrich, *Ultrathin Magnetic Structures Part I,* pp. 21–85, Springe, 1994.

[65] P. F. Carcia, Perpendicular magnetic anisotropy in Pd/Co and Pt/Co thin-film layered structures, *Journal of Applied Physics,* vol. 63, no. 10, pp. 5066–5073, 1988.

[66] W. B. Zeper, F. J. A. M. Greidanus, P. F. Carcia and C. R. Fincher, Perpendicular magnetic-anisotropy and magneto-optical Kerr effect of vapor-deposited Co/Pt-layered structures, *Journal of Applied Physics,* vol. 65, no. 12, pp. 4971–4975, 1989.

[67] P. F. Carcia and W. B. Zeper, Sputtered Pt/Co multilayers for magneto-optical recording, *IEEE Transactions on Magnetics,* vol. 26, no. 5, pp. 1703–1705, 1990.

[68] P. F. Carcia, M. Reilly, Z. G. Li and H. W. van Kesteren, Ar-sputtered Pt/Co multilayers with large anisotropy energy and coercivity, *IEEE Transactions on Magnetics,* vol. 30, no. 6, pp. 4395–4397, 1994.

[69] R. A. Hajjar, M. Mansuripur and H. P. D. Shieh, Measurements of magnetoresistance in magneto-optical recording media, *Journal of Applied Physics,* vol. 69, no. 10, pp. 7067–7080, 1991.

[70] C. T. Rettner, S. Anders, J. E. E. Baglin, T. Thomson, and B. D. Terris, Characterization of the magnetic modification of Co/Pt multilayer films by He^+, Ar^+, and Ga^+ ion irradiation, *Applied Physics Letters,* vol. 80, no. 2, pp. 279–281, 2002.

[71] M. Becherer, G. Csaba, W. Porod, R. Emling, P. Lugli and D. Schmitt-Landsiedel, Magnetic Ordering of Focused-Ion-Beam Structured Cobalt-Platinum Dots for Field-Coupled Computing, *IEEE Transactions on Nanotechnology,* vol 7, no 3, pp. 316–320, 2008.

[72] M. Becherer, G. Csaba, R. Emling, P. Osswald, W. Porod, P. Lugli and D. Schmitt-Landsiedel, Extraordinary Hall-effect sensor in split-current design for readout of magnetic field-coupled logic devices, *2nd IEEE International Nanoelectronics Conference INEC08,* Shanghai, March 2008.

[73] M. Becherer, G. Csaba, R. Emling, L. Ji, W. Porod, P. Lugli and D. Schmitt-Landsiedel, Focused ion beam structured Co/Pt multilayers for field-coupled magnetic computing, *Mater. Res. Soc. Symp. Proc,* vol. 998, no. 998-J06-07, Warrendale, 2007.

[74] M. Becherer, G. Csaba, R. Emling, W. Porod, P. Lugli and D. Schmitt-Landsiedel, Field-coupled nanomagnets for interconnect-free nonvolatile computing, *IEEE International Solid-State Circuits Conference ISSCC,* pp. 474–475, Feb. 2009.

[75] M. Becherer, J. Kiermaier, G. Csaba, J. Rezgani, C. Yilmaz, P. Osswald, P. Lugli and D. Schmitt-Landsiedel, Characterizing magnetic field-coupled computing devices by the Extraordinary Hall-Effect, *39th European Solid-State Device Research Conference ESSDERC,* pp. 474–475, Athens, Sep. 2009.

[76] M. Becherer, J. Kiermaier, S. Breitkreutz, G. Csaba, X. Ju, J. Rezgani, T. Kießling, C. Yilmaz, P. Osswald, P. Lugli and D. Schmitt-Landsiedel On-chip Extraordinary Hall-effect sensors for characterization of nanomagnetic logic devices, *Solid-State Electronics,* vol. 54, pp. 1027–1032, 2010.

[77] M. Becherer, *Nanomagnetic Logic in Focused Ion Beam Engineered Co/Pt Multilayer Films, Selected Topics of Electronics and Micromechatronics*, vol. 38, Shaker Verlag, 2011.

[78] J. Kiermaier, S. Breitkreutz, X. Ju, G. Csaba, D. Schmitt-Landsiedel and M. Becherer, Field-coupled computing: Investigating the properties of ferromagnetic nanodots, *Solid-State Electronics,* vol. 65, pp. 240–245, 2011.

[79] J. Kiermaier, S. Breitkreutz, X. Ju, G. Csaba, D. Schmitt-Landsiedel and M. Becherer, Ultra-low volume ferromagnetic nanodots for field-coupled computing devices, *40th European Solid-State Device Research Conference (ESSDERC),* pp. 214–217, Sevilla, 2010.

[80] X. Ju, S. Wartenburg, M. Becherer, J. Kiermaier, S. Breitkreutz, D. Schmitt-Landsiedel, P. Lugli and G. Csaba, Computational model of partially irradiated nanodots for field-coupled computing devices, *14th International Workshop on Computational Electronics (IWCE),* Pisa, 2010.

[81] X. Ju, M. Becherer, J. Kiermaier, S. Breitkreutz, P. Lugli and G. Csaba, Error analysis of Co/Pt multilayer based Nanomagnetic Logic, *11th IEEE Conference on Nanotechnology,* pp. 1034–1037, Portland, August 2011.

[82] X. Ju, S. Wartenburg, J. Rezgani, M. Becherer, J. Kiermaier, S. Breitkreutz, D. Schmitt-Landsiedel, W. Porod, P. Lugli and G. Csaba, Nanomagnet Logic from Partially Irradiated Co/Pt Nanomagnets, *IEEE Transactions on Nanotechnology,* vol. 11, no. 1, pp. 97–104, 2012.

[83] S. Breitkreutz, J. Kiermaier, X. Ju, G. Csaba, D. Schmitt-Landsiedel and M. Becherer, Nanomagnetic Logic: Demonstration of directed signal flow for field-coupled computing devices, *41th European Solid-State Device Research Conference (ESSDERC),* pp. 323–326, Helsinki, Sep. 2011.

[84] I. Eichwald, A. Bartel, J. Kiermaier, S. Breitkreutz, G. Csaba, D. Schmitt-Landsiedel and M. Becherer, Nanomagnetic Logic: error-free, directed signal transmission by an inverter chain , accepted for publication in *IEEE Transactions on Magnetics,* 2012.

[85] S. Breitkreutz, J. Kiermaier, I. Eichwald, X. Ju, G. Csaba, D. Schmitt-Landsiedel and M. Becherer, Majority Gate for Nanomagnetic Logic with Perpendicular Magnetic Anisotropy, accepted for publication in *IEEE Transactions on Magnetics,* 2012.

[86] S. Breitkreutz, J. Kiermaier, S. V. Karthik, G. Csaba, D. Schmitt-Landsiedel and M. Becherer, Controlled reversal of Co/Pt dots for nanomagnetic logic applications, *Journal of Applied Physics,* vol. 111, no. 07A715, 2012.

[87] P. Weiss, Controlled reversal of Co/Pt dots for nanomagnetic logic applications, *Compt. Rend.,* vol. 143, pp. 1136–1139, 1906.

[88] Charles Kittel, *Introduction to Solid State Physics,* New York: Wiley, 1996.

[89] B. Kiefer and D. C. Lagoudas, Magnetic field-induced martensitic variant reorientation in magnetic shape memory alloys, *Philosophical Magazine,* vol. 85, no. 33–35, pp. 4289–4329, 2005.

[90] I. Karaman, B. Basaran, H. E. Karaca, A. I. Karsilayan and Y. I. Chumlyakov, Energy harvesting using martensite variant reorientation mechanism in NiMnGa magnetic shape memory alloy, *Applied physics letters,* vol. 90, no. 17, pp. 172505, 2007.

[91] E. C. Stoner and E. P. Wohlfarth, A mechanism of magnetic hysteresis in heterogeneous alloys, *Philosophical Transactions of the Royal Society A: Physical, Mathematical and Engineering Sciences,* vol. 240, no. 826, pp.599642,1948.

[92] A. DeSimone, H. Knüpfer and F. Otto, 2-d stability of the Néel wall, *Calculus of Variations and Partial Differential Equations,* vol. 27, no. 2, pp. 233–253, 2006.

[93] S. A. Dyachenko, V. F. Kovalenko, B. N. Tanygin and A. V. Tychko, Influence of the demagnetizing field on the structure of a Bloch wall in a (001) plate of a magnetically ordered cubic crystal, *Physics of the Solid State,* vol. 50, no. 1, pp. 32–42, 2008.

[94] http://math.nist.gov/oommf/, OOMMF 1.2 a3

[95] http://llgmicro.home.mindspring.com/index.htm

[96] H. Fangohr, T. Fischbacher, M. Franchin, G. Bordignon, J. Generowicz, A. Knittel, M. Walter and M. Albert, NMAG User Manual Documentation, available at: http://nmag.soton.ac.uk/nmag/index.html.

[97] http://math.nist.gov/oommf/software-12a4pre.html

[98] http://www.nanoscience.de/group_r/stm-spstm/projects/temperature/download.shtml, Oxs extension module.

[99] O. Hellwig, A. Berger, J. B. Kortright and E. E. Fullerton, Domains structure and magnetization reversal of antiferromagnetically coupled perpendicular anisotropy films, *Journal of Magnetism and Magnetic Materials,* vol. 319, pp. 13–55, 2007.

[100] J. Crangle, *The magnetic properties of solids,* Edward Arnold, London, 1977.

[101] V. W. Guo, B. Lu, X. Wu, G. Ju, B. Valcu and D. Weller, A survey of anisotropy measurement techniques and study of thickness effect on interfacial and volume anisotropies in Co/Pt multilayer media, *Journal of Applied Physics,* vol. 99, no. 08E918, 2006.

[102] W. Gong, H. Li, Z. Zhao and J. Chen, Ultrafine particles of Fe, Co, and Ni ferromagnetic metals, *Journal of Applied Physics,* vol. 69, no. 8, pp. 5119–5121, 1991.

[103] N. Rizos, *Simulation of nanomagnetic logic devices from Co/Pt multilayers,* Master thesis, Technische Univeristät München, 2008.

[104] A. Murayama, M. Miyamura, K. Nishiyama, K. Miyata and Y. Oka, Brillouin spectroscopy of spin waves in sputtered CoPt alloy films and Co/Pt/Co multilayered films, *J. Appl. Phys,* vol. 69, no. 5661, 1991.

[105] S. Hashimoto and Y. Ochiai, Co/Pt and Co/Pd multilayers as magneto-optical recording materials, *Journal of Magnetism and Magnetic Materials,* vol. 88, no. 1–2, pp. 211–226, 1990.

[106] C. Vieu, J. Gierak, H. Launois, T. Aign, P. Meyer, J. P. Jamet, J. Ferré, C. Chappert, T. Devolder, V. Mathet and H. Bernas, Modifications of magnetic properties of Pt/Co/Pt thin layers by focused gallium ion beam irradiation, *Journal of Applied Physics,* vol. 91, no. 5, pp. 3103–3110, 2002.

[107] G. J. Kusinski and G. Thomas, Physical and Magnetic Modification of Co/Pt Multilayers by Ion Irradiation, *Microscopy and Microanalysis,* vol. 8, no. 4, pp. 319–332, August 2002.

[108] P. Warin, R. Hyndman, J. Gierak, J. N. Chapman, J. Ferré, J. P. Jamet, V. Mathet and C. Chappert, Modification of Co/Pt multilayers by gallium irradiation – Part 2: The effect of patterning using a highly focused ion beam, *Journal of Applied Physics,* vol. 90, no. 8, pp. 3850–3855, 2001.

[109] T. Aign, P. Meyer, S. Lemerle, J. P. Jamet, J. Ferré, V. Mathet and C. Chappert, J. Gierak, C. Vieu, F. Rousseaux, H. Launois and H. Bernas, Magnetization reversal in arrays of perpendicularly magnetized ultrathin dots coupled by dipolar interaction, *Physical Review Letters,* vol. 81, pp. 5656–5659, 1998.

[110] J. F. Ziegler and J. P. Biersack, The stopping and range of ions in solids, *The stopping and ranges of ions in matter,* vol. 1, New York: Pergamon Press, 1984.

[111] J. F. Ziegler, SRIM: The stopping and ranges of ions in matter Available online: http://www.srim.org/

[112] J. M. Shaw, S. E. Russek, T. Thomson, Mi. J. Donahue, B. D. Terris, O. Hellwig, E. Dobisz and M. L. Schneider, Reversal mechanisms in perpendicularly magnetized nanostructures, *Phys. Rev. B,* vol 78, no. 024414, 2008.

[113] P. Li, G. Csaba, V. K. Sankar, X. Ju, P. Lugli, X. S. Hu, M. Niemier, W. Porod, G. H. Bernstein, Switching behavior of lithographically fabricated nanomagnets for logic applications, *J. Appl. Phys,* vol. 111, no. 7, 2012.

[114] G. Gallavotti, *Statistical mechianics,* Berlin: Springer-Verlag, 1999.

[115] G. Csaba, P. Lugli, M. Becherer, D. Schmitt-Landsiedel and W. Porod, Field-coupled computing in magnetic multilayers, *Journal of Computational Electronics,* vol. 7, no. 3, 2008.

[116] D. B. Carlton, N. C. Emley, E. Tuchfeld and J. Bokor, Simulation Studies of Nanomagnet-Based Logic Architecture, *Nano Lett.,* vol. 8, no. 12, pp. 4173–4178, 2008.

[117] S. S. P. Parkin, M. Hayashi and L. Thomas, Magnetic Domain-Wall Racetrack Memory, *Science,* vol. 320, 2008.

[118] R. Hyndman, P. Warin, J. Gierak, J. N. Chapman, J. Ferré, J. P. Jamet, V. Mathet and C. Chappert, Modification of Co/Pt multilayers by gallium irradiation – Part 2: The effect of strcutral and magnetic properties, *Journal of Applied Physics,* vol. 90, no. 8, pp. 3850–3855, 2001.

[119] T. Devolder, J.Ferré, C. Chappert, H. Bernas, J. P. Jamet and V. Mathet, Magnetic properties of He^+-irradiated Pt/Co/Pt ultrathin films, *Physical Review B,* vol. 64, no. 6, 2001.

[120] L. S. Alvarez, G. Burnell, C. H. Marrows, K. Y. Wang, A. M. Blackburn and D. A. Williams, Nucleation and propagation of domain walls in a Co/Pt multilayer wire, *Journal of Applied Physics,* vol. 101, no. 09F508, 2007.

[121] G. Csaba and W. Porod, Behavior of Nanomagnet Logic in the presence of thermal noise, *14th International Workshop on Computational Electronics (IWCE),* Pisa, Italy, 2010.

[122] S. Mangin, D. Ravelosona, J. A. Katine, M. J. Carey, B. D. Terris and E. E. Fullerton, Current-induced magnetization reversal in nanopillars with perpendicular anisotropy, *Nature Materials,* vol. 5, pp. 210–215, 2006.

[123] H. T. Kung and C. E. Leiserson, Algorithms for VLSI processor arrays, *Introduction to VLSI Systems,* Addison-Wesley, 1979.

[124] H. T. Kung, Why systolic architectures?, *Computer,* vol. 15, pp. 37–46, 1982.

[125] S. Breitkreutz, J. Kiermaier, C. Yilmaz, X. Ju, G. Csaba, D. Schmitt-Landsiedel and M. Becherer, Nanomagnetic logic: compact modeling of field-coupled computing devices for system investigations, *Journal of Computational Electronics,* vol. 10, no. 4, pp. 352–359, 2011.

[126] M. T. Niemier, G. H. Bernstein, G. Csaba, A. Dingler, X. S. Hu, S. Kurtz, S. Liu, J. Nahas, W. Porod, M. Siddiq and E. Varga, Nanomagnet logic: progress toward system-level integration, *Journal of Physics: Condensed Matter,* vol. 23, no. 49, 2011.

[127] D. S. Gardner, G. Schrom, P. Hazucha, F. Paillet, T. Karnik, S. Borkar, R. Hallstein, T. Dambrauskas, C. Hill, C. Linde, W. Worwag, R. Baresel, and S. Muthukumar, Integrated on-chip inductors using magnetic material, *Journal of Applied Physics,* vol. 103, no. 07E927, 2008.

[128] N. Rizos, M. Omar, M. Becherer, D. Schmitt-Landsiedel, P. Lugli and G. Csaba, Clocking Schemes for Field Coupled Devices from Magnetic Multilayers, *13th International Workshop of Computational Electronics (IWCE),* Beijing, 2009.

[129] G. Csaba, J. Kiermaier, M. Becherer, S. Breitkreutz, X. Ju, P. Lugli, D. Schmitt-Landsiedel and W. Porod, Clocking magnetic field-coupled devices by domain walls, *J. Appl. Phys,* vol. 111, no. 7, 2012.

[130] L. Ji, A. Orlov, G. H. Bernstein, W. Porod and G. Csaba, Domain-wall trapping and control on submicron magnetic wire by localized field, *9th IEEE Conference on Nanotechnology,* pp. 758–762, Genoa, Italy, 2009.

[131] G. Csaba, P. Lugli, L. Ji and W. Porod, Micromagnetic simulation of current-driven domain wall propagation, *Journal of Computational Electronics,* vol. 6, no. 1–3, pp. 121–124, 2007.

[132] C. Faulkner, M. D. Cooke, D. A. Allwood, D. Petit, D. Atkinson and R. P. Cowburn, Artificial domain wall nanotraps in Ni_81Fe_19 wires, *J. Appl. Phys,* vol. 95, no. 6717, 2004.

[133] A. Thiaville, Y. Nakatani, J. Miltat and Y. Suzuki, Micromagnetic understanding of current-driven domain wall motion in patterned nanowires, *Europhysics Letters,* vol. 69, no. 6, 2005.

[134] M. Hayashi, L. Thomas, Y. B. Bazaliy, C. Rettner, R. Moriya, X. Jiang and S. S. P. Parkin, Influence of Current on Field-Driven Domain Wall Motion in Permalloy Nanowires from Time Resolved Measurements of Anisotropic Magnetoresistance, *Phys. Rev. Lett.,* vol. 96, no. 19, 2006.

[135] R. P. Cowburn, D. A. Allwood, G. Xiong and M. D. Cooke, Domain wall injection and propagation in planar Permalloy nanowires, *J. Appl. Phys,* vol. 91, no. 10, pp. 6949–6951, 2002.

[136] X. Ju, J. Kiermaier, M. Becherer, S. Breitkreutz, I. Eichwald, D. Schmitt-Landsiedel, W. Porod, P. Lugli and G. Csaba, Modeling interaction between Co/Pt nanomagnets and Permalloy domain wall for Nanomagnet Logic, accepted for publication in *12th IEEE Conference on Nanotechnology,* 2012.

[137] X. Ju, J. Kiermaier, A. Savo, M. Becherer, S. Breitkreutz, D. Schmitt-Landsiedel, W. Porod, P. Lugli and G. Csaba, Computational study of domain-wall-induced switching of Co/Pt multilayer, *15th International Workshop on Computational Electronics (IWCE),* Madison, 2012.

[138] J. Kiermaier, S. Breitkreutz, I. Eichwald, X. Ju, G. Csaba, D. Schmitt-Landsiedel and M. Becherer, Programmable Input for Nanomagnetic Logic Devices, accepted for publication in *European Physical Journal Web of Conferences,* 2012.

[139] E. E. Huber, D. O. Smith and J. B. Goodenough, Domain Wall Structure in Permalloy Films, *J. Appl. Phys.,* vol. 29, no. 3, pp. 294–295, 1958.

[140] R. D. Gomez, T. V. Luu, A. O. Pak, K. J. Kirk, and J. N. Chapman, Domain configurations of nanostructured Permalloy elements, *J. Appl. Phys.,* vol. 85, no. 8, pp. 6163–6165, 1999.

[141] T. Trunk, M. Redjdal, A. Kákay, M. F. Ruane, and F. B. Humphrey, Domain wall structure in Permalloy films with decreasing thickness at the Bloch to Néel transition, *J. Appl. Phys.,* vol. 89, no. 11, pp. 7606–7608, 2001.

[142] R. D. McMichael and M. J. Donahue, Head to head domain wall structures in thin magnetic strips, *IEEE Transaction on Magnetics,* vol. 33, no. 5, pp. 4167–4169, 1997.

[143] A.Hubert and R. Schäfer, *Magnetic Domains: the analysis of magnetic microstructures,* Springer, 1998.

[144] Andrew Kunz, Simulating the Maximum Domain Wall Speed in a Magnetic Nanowire, *IEEE Transaction on Magnetics,* vol. 42, no. 10, pp. 3219–3221, 2006.

[145] D. Atkinson, D. A. Allwood, G. Xiong, M .D. Cooke, C. C. Faulkner and R. P. Cowburn, Magnetic domain-wall dynamics in a submicrometre ferromagnetic structure, *Nature Materials,* vol. 2, pp. 85–87, 2003.

[146] G. Beach, C. Nistor, C. Knutson, M. Tsoi and J. L. Erskine, Dynamics of field-driven domain-wall propagation in ferromagnetic nanowires, *Nature Materials,* vol. 4, pp. 741–747, 2005.

[147] Z. Li and S. Zhang, Domain-wall dynamics driven by adiabatic spin-transfer torques, *Phys. Rev. B,* vol. 70, no. 2, 2004.

[148] G. Tatara and H. Kohno, Theory of Current-Driven Domain Wall Motion: Spin Transfer versus Momentum Transfer, *Phys. Rev. Lett.,* vol. 92, no. 8, 2004.

[149] Z. Diao, Z. Li, S. Wang, Y. Ding, A. Panchula, E. Chen, L. Wang and Y. Huai, Spin-transfer torque switching in magnetic tunnel junctions and spin-transfer torque random access memory, *J. Phys.: Condens. Matter,* vol. 19, pp. 165209, 2007.

[150] C. Augustine, B. Behin-Aein, X. Fong and K. Roy, A Design Methodology and Device/Circuit/Architecture Compatible Simulation Framework for Low-Power Magnetic Quantum Cellular Automata Systems, *2009 Asia and South Pacific Design Automation Conference,* pp. 847–852, Yokohama, 2009.

[151] S. Liu, X. S. Hu, J. J. Nahas, M. T. Niemier, W. Porod and G. H. Bernstein, MagneticElectrical Interface for Nanomagnet Logic, *IEEE Transactions on Nanotechnology,* vol. 10, no. 4, pp. 757–763, 2012.

[152] M. Graziano, A. Chiolerio and M. Zamboni, A technology aware magnetic QCA NCL-HDL architecture, *9th IEEE Conference on Nanotechnology,* pp. 763–766, Genoa, 2009.

[153] M. Graziano, M. Vacca, A. Chiolerio and M. Zamboni, An NCL-HDL Snake-Clock-Based Magnetic QCA Architecture, *IEEE Transactions on Nanotechnology,* vol. 10, no.5, pp. 1141–1149, 2011.

[154] X. Ju, M. T. Niemier, M. Becherer, W. Porod, P. Lugli and G. Csaba, Application of Nanomagnetic Logic: Co/Pt based Systolic Pattern Matcher, submitted to *IEEE Transactions on Nanotechnology,* 2012.

[155] M. Niemier, X. Ju, G. Csaba, M. Becherer, A. Dingler, X. S. Hu, D. Schmit-Landsiedel, P. Lugli and W. Porod, Boolean and Non-Boolean Nearest Neighbor Architectures for Out-of-Plane Nanomagnet Logic, accepted for publication in *International workshop on Cellular Nanoscale Networks and their Applications,* 2012.

[156] R. P. Cowburn, Probing antiferromagnetic coupling between nanomagnets, *Phys. Rev. B,* vol. 65, no. 092409, 2002.

[157] V. Novosad, M. Grimsditch, K. Yu Guslienko, P. Vavassori, Y. Otani and S. D. Bader, Spin excitations of magnetic vortices in ferromagnetic nanodots, *Phys. Rev. B,* vol. 66, no. 052407, 2002.

[158] T. A. Savas, M. Farhoud, H. I. Smith, M. Hwang and C. A. Rossa, Properties of large-area nanomagnet arrays with 100 nm period made by interferometric lithography, *Journal of Applied Physics,* vol. 85, no. 8, pp. 6160–6162, 1999.

[159] Y. Hao, C. A. Ross and H. I. Smith, Thermal stability of the magnetization of 150nm × 230nm $Ni_{19}Fe_{81}$ elements, *J. Appl. Phys.,* vol. 93, no. 10, pp. 7909–7911, 2003.

[160] S. Jain, A. O. Adeyeye and N. Singh, Spin re-orientation in magnetostatically coupled $Ni_{80}Fe_{20}$ ellipsoidal nanomagnets, *Nanotechnology,* vol. 21, no. 285702, 2010.

[161] M. Natali, I. L. Prejbeanu, A. Lebib, L. D. Buda, K. Ounadjela and Y. Chen, Correlated Magnetic Vortex Chains in Mesoscopic Cobalt Dot Arrays, *Phys. Rev. Lett.,* vol. 88, no. 157203, 2002.

[162] S. Moralejo, F.J. Castano, C. Redondoa, R. Jic, K. Nielschc, C.A. Ross and F. Castan, Fabrication and magnetic properties of hexagonal arrays of NiFe elongated nanomagnets, *Journal of Magnetism and Magnetic Materials,* vol. 316, no. 2, pp. e44–e47, 2007.

[163] M. P. Sharrock, Time dependence of switching fields in magnetic recording media, *Journal of Applied Physics,* vol. 76, no. 10, pp. 6413–6418, 1994.

[164] J. Shi, T. Zhu, M. Durlam, E. Chen, S. Tehrani, Y. F. Zheng, and J. G. Zhu, End domain states and magnetization reversal in submicron magnetic structures, *IEEE Transactions on Magnetics,* vol. 34, no. 4, pp. 997–999, 1998.

[165] http://www.microsense.net/products-vsm-accessories.htm.

[166] G. H. Bernstein, D. A. Hill, and W. P. Liu, New highcontrast developers for poly(methyl methacrylate) resist, *J. Appl. Phys.,* vol. 71, no. 8, pp. 4066–4075, 1992.

[167] E. Varga, A. Orlov, M. T. Niemier, X. S. Hu, G. H. Bernstein, and W. Porod, Experimental Demonstration of Fanout for Nanomagnetic Logic, *IEEE Transactions on Nanotechnology,* vol. 9, no. 6, pp. 668–670, 2010.

[168] P. Li, G. Csaba, V. K. Sankar, X. Ju, E. Varga, P. Lugli, X. S. Hu, M. Niemier, W. Porod and G. H. Bernstein, Direct Measurement of Magnetic Coupling between Nanomagnets for NML Applications, accepted for publication in *IEEE Transactions on Magnetics*, 2012.

[169] G. Csaba, M. Becherer and W. Porod, Development of CAD tools for Nanomagnetic Logic Devices, *International Journal of Circuit Theory and Applications,* April 2012.